ResearchOnline@JCU

JAMES COOK UNIVERSITY AUSTRALIA

This file is part of the following work:

Muccignat, Dale (2024) ***The determination of scattering cross-sections for non-equilibrium electrons in gaseous and liquid environments using deep learning.*** **PhD Thesis, James Cook University.**

Access to this file is available from:

https://doi.org/10.25903/9tz9%2Dxz30

Copyright © 2024 Dale Muccignat

The author has certified to JCU that they have made a reasonable effort to gain permission and acknowledge the owners of any third party copyright material included in this document. If you believe that this is not the case, please email researchonline@jcu.edu.au

The determination of scattering cross-sections for non-equilibrium electrons in gaseous and liquid environments using deep learning

Dale Muccignat

Bachelor of Science (Maths & Physics) (Honours)

0000-0002-6693-6851

A thesis submitted for the degree of Doctor of Philosophy at James Cook University in 2024

College of Science & Engineering

Abstract

Accurate modelling of electron scattering from liquids and complex biological targets is critical for the development and implementation of plasma devices in fields such as medicine, nanoscale device manufacturing and agriculture. A necessary ingredient for electron transport models is the microscopic description of electron scattering through matter, which is usually described through complete sets of cross-sections. Current theoretical, experimental and numerical methods have thus far provided a wealth of electron scattering cross-section sets for various gas-phase molecular targets and non-polar liquids. However, the same can not be said for scattering in polar liquids and from complex molecules due to a combination of limitations in theory, direct experimental measurements and numerical techniques.

The focus of this work is thus directed toward the determination of electron scattering cross sections, particularly in regimes where existing techniques are limited. We propose a new experimental technique and improve upon existing numerical techniques that aim to expand the horizon of cutting-edge electron transport research.

In partnership with Flinder's University, we present the first measurements of electron scattering from a liquid water surface in vacuum conditions through the use of a newly developed liquid micro-jet apparatus. Through a feasibility study that utilises simulations of the experimental apparatus, we demonstrate that, while complete electron-liquid cross section sets would require additional methods and measurements, select cross sections could be determined using deep learning. Using this knowledge, we then conduct initial tests of the experiment and compare the results with existing theory. First, the equipment was calibrated by varying the jet position perpendicular to the electron beam and comparing the scattered intensity to expected simulated results. A reference angle for the detectors was then determined through a Gaussian fit of the angular dependent scattered intensity. Finally, the first measurements of direct electron-liquid energy loss spectra under vacuum conditions are presented and compared with simulation data and their discrepancies are discussed. These results represent the first steps towards utilising direct electron-liquid energy loss spectra for the determination and validation of electron-liquid cross sections.

The determination of gas phase electron-scattering cross section sets for complex molecules represents a key limitation of current techniques. An iterative technique is often utilised to refine an initial prediction using existing knowledge about the molecule, the guidance of an expert and swarm transport coefficients. Recently, leveraging existing cross section sets available, a deep learning technique was developed for the determination of electron cross-sections from macroscopic measurements of electron swarm transport through gaseous environments [1]. Thus far, the method has been applied to the improvement of electron scattering cross-sections from biological molecules. In this work we extend and improve upon the method to reduce the need for prior information about electron scattering and apply the technique to a novel problem.

We demonstrate improvements to the deep learning technique that allow for the determination of full scattering cross-section sets in highly ill-posed regimes with minimal prior knowledge of its solution, and evaluate the performance of this technique using methane as an example due to its vibration and attachment processes. We find that the predicted cross section set is able to replicate methane's drift velocity, reduced longitudinal diffusion coefficient and effective ionisation rate within 0.48, 1.69, and 5.84 % mean absolute relative percentage error, respectively. Finally, we use the technique to determine an electron scattering cross section set for HFO1234ze(E) that demonstrates positive synergy in mixtures with SF_6 with a mean absolute relative percentage difference under 3 % for drift velocity, 13.5 % for reduced longitudinal diffusion and 64 % for effective ionisation rate across the three HFO1234ze(E) mixtures considered. Overall, this method allows a general and automated framework to determine a complete and self-consistent cross section set for arbitrary targets from swarm transport coefficients.

In total, this work advances our understanding of what deep learning techniques can achieve through new techniques that interpret newly developed liquid micro-jet experiments and solutions to ill-posed problems in particle transport.

Sources declaration

I declare that this thesis is my own work and has not been previously submitted in any form for any other degree or diploma at any university or other institute of tertiary education. Information derived from the published and unpublished work of others has been acknowledged in the text and a list of references is given.

Publications included in this thesis

1. [2] **D L Muccignat**, P W Stokes, D G Cocks, J R Gascooke, D B Jones, M J Brunger and R D White, Simulating the Feasibility of Using Liquid Micro-Jets for Determining Electron–Liquid Scattering Cross-Sections, *International Journal of Molecular Sciences*, 6, 23, 2022

2. [3] **D L Muccignat**, G J Boyle, N A Garland, P W Stokes and R D White, An iterative deep learning procedure for determining electron scattering cross-sections from transport coefficients, *Machine Learning: Science and Technology*, 5, 015047, 2024

3. [4] **N A Garland**, D L Muccignat, G J Boyle, and R D White, Robust approximation rules for critical electric field of dielectric gas mixtures, *Journal of Physics D: Applied Physics*, 2024

Submitted manuscripts included in this thesis

1. **D L Muccignat**, G J Boyle, N A Garland and R D White, Towards a self-consistent HFO1234ze-E electron scattering cross section set using deep learning

Other publications during candidature

1. [5] **L Campbell**, D L Muccignat, and M J Brunger, Inclusion of Electron Interactions by Rate Equations in Chemical Models, *Atoms*, 2022

Contributions by others to the thesis

I gratefully acknowledge the contributions detailed below.

Editorial assistance for the overall thesis was provided by Prof. Ronald White, Dr. Gregory Boyle, Dr. Nathan Garland and Dr. Darryl Jones. Chapter 2 and 4 are based on published papers where editorial assistance was provided by all of the listed co-authors.

Initial concept and design for the liquid micro-jet experiment was conducted by Prof. Ronald White, Prof. Michael Brunger, Dr. Jason Gascooke and Dr. Darryl Jones. The deep learning technique used for Chapter 2 was primarily conducted by Dr. Peter Stokes. The experimental design presented in Chapter 3 was conducted under the supervision and with the assistance of Dr. Darryl Jones and Dr. Jason Gascooke. The Boltzmann equation solver used in Chapters 4 and 5 was designed and written by Dr. Peter Stokes. The initial concept and design of the deep learning technique that forms the basis for Chapters 4 and 5 was conducted by Prof. Ronald White and Dr. Peter Stokes. The concept and design of the iterative deep learning method presented in Chapter 4 was conducted under the supervision and with the assistance of Prof. Ronald White, Dr. Peter Stokes, Dr. Gregory Boyle and Dr. Nathan Garland. The experimental data used in Chapter 5 was provided by Prof. Franck Christian and Dr. Eda Eguż.

A more detailed discussion of the contributions from co-authors is given at the beginning of each chapter.

Statement of parts of the thesis submitted to qualify for the award of another degree

No works submitted towards another degree have been included in this thesis

Research involving human or animal subjects

No animal or human subjects were involved in this research

Acknowledgments

I am, and forever will be, grateful for the support of numerous people throughout this work. I would like to give particular acknowledgement to the people listed below.

I am deeply grateful to my supervisor, Prof. Ronald White, for his endless support, guidance and understanding through the entirety of my studies. His infectious enthusiasm for discovery and belief in my potential led me to embark on a small research project between undergraduate semesters, which would later grow into the work presented here. I wish to thank him for the opportunities he has afforded me through my studies and for showing me the wonders of research.

I would like to thank Dr. Daniel Cocks, Dr. Peter Stokes, Dr. Gregory Boyle and Dr. Nathan Garland for their support, advice and expertise. Their willingness to understand and assist was invaluable and integral to this work. I am grateful for the countless fruitful and enthralling discussions that always resulted in more exciting paths to explore.

I am grateful to Prof. Michael Brunger, Dr. Darryl Jones and Dr. Jason Gascooke for welcoming me at Flinder's University and for the opportunity to work on the liquid micro-jet experiment. I wish to thank them for their assistance and willingness to answer my endless questions, especially when it came to equipment malfunctions.

I am immensely grateful to my partner, Hadassah Harland, for their patience, kindness and understanding. Their determination and drive for adventure is an inspiration that has kept me going, even when my own would falter. Their tireless and immense efforts to ensure that I was cared for and well fed, particularly through many late nights, is a debt that I can only hope to repay.

I would like to give special thanks to my brothers, my parents and my grandparents, for always being there when I needed and for believing in me. I will always be grateful for their support and unconditional love, *no matter what*.

Finally, I would like to thank my friends and fellow students for always being supportive and understanding. In particular, I would like to thank Kel Hinchley for his endless enthusiasm, curiosity and unconditional willingness to help.

Financial support

This research was supported by an Australian Government Research Training Program Scholarship and Australian Research Council (ARC) through its Discovery program (DP180101655, DP190100696 and DP220101480).

Chapter 1

Introduction

1.1 Motivation, aims and applications

Electron transport through gaseous, liquid and plasma environments represents the foundation for a vast array of cutting-edge research and applications. From microelectronics [6] to linear accelerators for cancer treatment [7], technologies that leverage electron transport are omnipresent in everyday life. The advancement of current technology, and the development of new applications, relies on a detailed understanding of microscopic interactions between electrons and molecules in each state of matter. In what follows, we highlight two prominent knowledge gaps surrounding the scattering of electrons through liquid environments and gaseous complex molecules. The work presented in this thesis is thus conducted in two phases that aim to further our understanding in each of these areas.

The first phase of this work is motivated by the application of plasma to heat sensitive and liquid targets. Plasma is a unique state of matter composed of both neutral and excited molecules, radicals, electrons and ions. When applied to a surface these highly reactive species can be used to drive numerous important reactions. For example, the microelectronics industry utilise plasmas to deposit and remove materials when fabricating micro-processes [6]. Of interest to this work is the application of low temperature plasmas (LTPs) to liquids, which is fundamental to a variety of important domains including environmental remediation, synthesis of nanomaterials and medicine [8–11]. LTPs are generally distinguished through typical electron temperatures that are much higher than its equilibrium ion and background neutral temperatures [12]. The generated heat flux is then significantly reduced while still maintaining sufficient electron energies to drive reactions within the plasma and the applied surface. Excited or ionised molecules from within the plasma or target material then react with other molecules to generate biologically relevant species. Critically, this property enables their application to heat sensitive biological matter in atmospheric conditions.

Shown in Figure 1.1 is the interaction region of the plasma-liquid interface, which exhibits

highly complex and non-equilibrium scattering mechanics. Identified in the Plasma Roadmaps [10, 11], and the Plasma-Liquid Roadmap [13], the predictive control of each processes is crucial for applications associated with the interaction of LTPs and liquids. In particular, low energy ($< 10\,\text{eV}$) electrons play a key role in driving reactions at the plasma-liquid interface and modelling their transport is critical for the high-level optimisation of efficacy and selectivity of current and future generation plasma-liquid applications [14]. Recent experiments have shown that electrons may penetrate up to $10 - 20\,\text{nm}$ into the liquid before solvation occurs [15–19].

Predictive modelling of electron scattering processes enables a broader and more systematic sampling of the parameter space than what can be achieved physically. The majority of plasma-liquid models however, assume immediate solvation into the liquid [17, 20, 21] or utilise microscopic scattering information (cross-sections) derived from gas phase or amorphous ice scattering measurements [22]. These models may neglect any free non-equilibrium electron penetration, and associated pre-solvated electron-induced chemistry near the surface, including excitation, ionisation, radical formation and other important processes such as dissociative electron attachment processes well known to occur in the modelling of secondary electron radiation damage [23].

Theoretical approaches to describe electron scattering through non-polar liquids has recently reached some maturity [24,25] but the same can not be said for polar liquids. Polar liquids exhibit trapped electron states and free electron scattering from spatially, temporally and orientationally correlated dipoles. Critical for the validation of theoretical approaches are experimental measurements of electron scattering in liquid environments. The high vapour pressure and the volatile nature of liquids makes their study in experimental conditions, particularly in vacuums, difficult to achieve [26]. Experiments generally measure either macroscopic properties of electron swarms

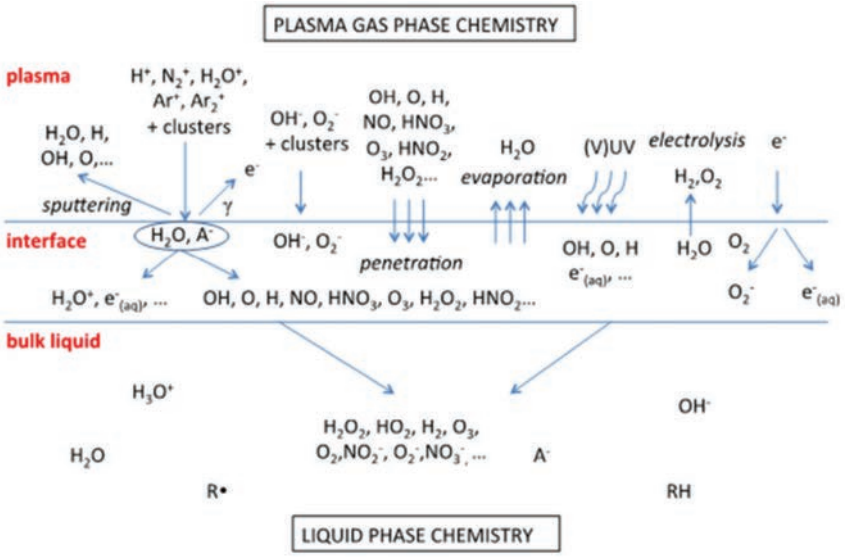

Figure 1.1: An overview of the induced reactions and their reactive species across the plasma-liquid interface. Sourced from Bruggeman *et al.* [13].

in liquids [27–30] or indirectly through photoelectron scattering from liquid beams [31–39]. Therefore, in the first phase of this work, we propose and investigate the feasibility of a new electron-liquid scattering experiment for this purpose.

The motivations for the second phase of this thesis is informed by the need to reduce the use of sulfur hexafluoride (SF_6) as a dielectric insulator in high voltage applications. Dielectric insulators are extensively used in high voltage circuit breakers and in gas insulated switchgear due to their strong electron attaching properties, heat transfer capacity and arc-quenching ability [40, 41]. For high voltage applications, SF_6 has existed as the favoured insulation medium for the electrical industry since 1960 [40]. However, the use of SF_6 is being phased out due to its considerably high global warming potential (GWP) and a search is underway for low GWP alternatives [40]. This search requires the union of experimental measurements and theoretical descriptions of electron scattering from numerous complex molecules that are not currently well described.

1,3,3,3-Tetrafluoropropene ($C_3H_2F_4$), commonly referred to as HFO1234ze-E, has recently been proposed for use in dielectric insulators due to its positive synergy effects in mixtures with SF_6 that results in a higher critical field than either HFO1234ze-E or SF_6 [42]. The extensive use of SF_6 could then be substantially reduced by replacing large fractions of SF_6 with HFO1234ze-E without a reduction in critical field strength. However, in order to model such mixtures, an accurate electron scattering cross section set is required. The polyatomic nature of this molecule, along with the three-body processes observed [43], hinders theoretical approaches to deriving the associated electron scattering cross section set. In addition, the extensive search for replacement candidates makes it difficult to justify the time and monetary cost of crossed-beam scattering experiments, which enable the direct measurement of microscopic scattering events [44].

In the exploratory phase for potential SF_6 replacements, numerical techniques such as the inverse swarm technique [45] and, more recently, a deep learning approach [46, 47] exist as a relatively fast an inexpensive alternative. However, the highly ill-posed nature of the problem renders their application limited when little prior knowledge exists for a particular molecule [47]. Motivated by this limitation, in the second phase of this work we propose modifications to the deep learning approach outlined by Stokes *et al.* [1] and then apply the technique to the determination of a complete and self-consistent description of electron scattering from HFO1234ze-E.

In what follows we provide an overview of electron scattering processes and the tools used to describe their motion through various mediums. We then describe and summarise the main experimental and numerical approaches currently used to determine electron scattering mechanics. Finally, we present an outline of the thesis structure before detailing the work conducted in each phase.

1.2 Electron transport in liquids and biological matter

Initially proposed by Ludwig Boltzmann in 1872 [48], and subsequently modified by Wang Chang *et al.* to include inelastic collisions [45, 49], the Boltzmann equation remains a prominent means for the description of non-equilibrium gases. The equation can be expressed as,

$$\frac{\partial f}{\partial t} + \vec{v} \cdot \vec{\nabla} f + \vec{a} \cdot \frac{\partial f}{\partial \vec{v}} = \left(\frac{\partial f}{\partial t} \right)_{\text{coll}}, \tag{1.1}$$

where $f(\vec{r}, \vec{v}, t)$ is the phase-space distribution function, $\vec{a}$ is the acceleration resulting from external forces such as electric fields, $\vec{r}$ and $\vec{v}$ are the position and velocity vectors respectively, and $\left(\frac{\partial f}{\partial t}\right)_{coll}$ accounts for all particle-neutral interactions. The phase-space distribution function offers a complete description of the system of particles and enables the description of critical macroscopic properties of electron swarms. The solution of Equation (1.1) relies on a complete microscopic description of electron scattering processes, which is provided by a complete set of differential cross sections. In what follows we provide a brief overview of differential cross sections and the associated collisional kinematics for electron scattering from atomic and molecular targets. For an in-depth description, see the work of Robson *et al.* [50]. We then give an overview of numerical techniques for the solution of Boltzmann's equation and the determination of cross section sets.

1.2.1 Electron scattering cross sections

Fundamental to modelling electron transport is the development of electron scattering differential cross sections, which represent a complete probabilistic description of a particle's interaction with a target particle and molecule for a given scattering process. Fundamentally, a differential cross-section is defined by the ratio of the number of particles scattering with a particular final velocity and initial incident beam of particles [50],

$$\sigma(g, \chi) = \frac{\text{Number of particles scattered into small element } d\chi}{\text{Incident particle flux}}, \tag{1.2}$$

where g is the relative speed of the collision, χ is the polar scattering angle. For reference, Figure 1.2 shows a schematic overview of the cross section definition. In this definition, we have assumed rotational symmetry around the scattering axis. The result of this is a probabilistic description of a scattering event that is a function of relative velocity and polar scattering angle.

When anisotropic scattering is weak, the solution of Boltzmann's equation commonly utilises the momentum transfer cross section, which, assuming the target molecule is at rest, can be defined as [51],

$$\sigma_{mj}(\varepsilon) = 2\pi \int_0^{\pi} \left[1 - \left(1 - \frac{\varepsilon_j}{\varepsilon} \right)^{1/2} \cos\chi \right] \sigma(g, \chi) \sin\chi d\chi, \tag{1.3}$$

where ε is the incident energy and ε_j is the threshold energy for the j-th inelastic scattering channel.

As a cross section's magnitude is dependent on the relative velocity of the scattering particles, it is often intuitively thought of as the cross sectional area of the target [50]. A larger cross-section, or surface area, results in a higher likelihood that the associated scattering event will occur. Leveraging their probabilistic nature, numeric solutions techniques can then predict the macroscopic effects of an ensemble of interacting particles and molecules. Each cross section may vary as a function of energy, the phase of matter for molecular targets and in the case of three-body effects, density.

Complete electron scattering cross section sets provide descriptions of each collision process available to the electron. Elastic collisions represent a standard binary collision that results in no change in the internal energy of either the incident or target particle. Excitation cross sections on the other hand contain a threshold energy, below which the probability of the collision is zero, and describes the discrete transfer of energy from the electron to transition the target molecule to a more energetic rotational, vibrational or electronic internal state of the target molecule. Conversely, super-elastic collisions represent the transition to a lower energetic state of the target molecule and an equivalent increase in the electron's energy. Ionisation and attachment collisions are non-conservative in nature and result in the ejection of an additional electron from the target or the attachment of the incident electron respectively.

Electron scattering events in the gas-phase exhibit an average inter-molecular distance that is much larger than the de-Broglie wavelength of the particle, which results in scattering events that

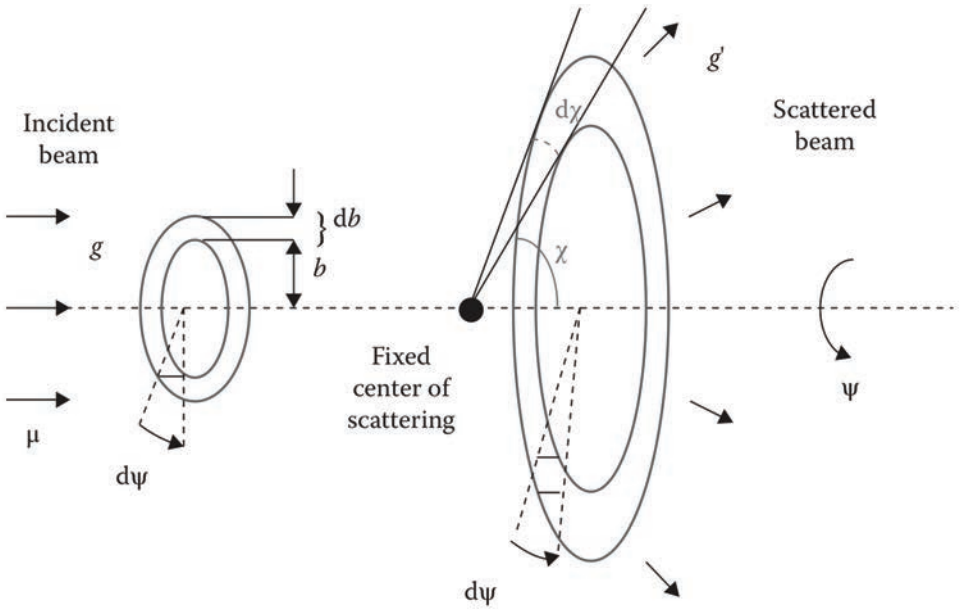

Figure 1.2: Graphical representation of a differential cross section for a beam of particles with a velocity g relative to the target velocity, an impact parameter between b and $b+db$, and reduced mass μ. The beam then scatters between χ and $\chi+d\chi$ with velocity g'. Figure is reproduced from [50].

are two-body in nature. Gas-phase cross sections can then be readily implemented in numerical electron transport modelling software, while their derivation ranges in difficulty depending on the complexity of the subject and the process it describes [44]. The field benefits from online databases such as LXCat [52], which is a collaborative and free reference for electron and ion cross sections in addition to experimental measurements of electron swarms.

Scattering events in the liquid-phase present a particularly challenging problem in low energy ($< 10\,\mathrm{eV}$) regimes due to the influence of neighbouring molecules. The density of liquid targets results in an inter-molecular spacing that is often less than the de-Broglie wavelength of electrons at these energies. In this regime scattering events may occur across multiple targets in addition to multiple scattering events per interaction. Recently, advances were made to account for these interactions for electron scattering through non-polar liquids [24]. Two modifications were made to the gas-phase scattering potential, which forms the basis for scattering cross sections. The first modification accounts for the induced dipole of each surrounding molecule, which results in a screening of the focus molecule's induced dipole in a scattering event. The second includes an additional effective potential to account for the interaction between the electron and other molecules in the bulk liquid.

An electron's transport through a polar liquid is generally described as existing in either a quasifree or a trapped state [53]. Trapped states arise from configurations of molecules that result in a source of low potential energy where quasifree electrons can be localized and then either fully solvated or activated once again into a quasifree state. In addition, at liquid surfaces the orientation of molecules can be correlated, which will require a depth-dependent modification to the scattering cross-section. Another important multi-body processes is three-body attachment, which can be found in molecules such as O_2 and HFO1234ze-E [54, 55]. Three-body attachment processes introduce a pressure dependence to the associated scattering cross section that must be characterised.

Self-consistency is a critical component of cross section sets and is defined by its ability to replicate experimental measurements. Commonly, cross section sets include only transitions from the ground state of the target molecule and total cross sections may be used in place of numerous similar collisional processes. The use of cross sections from a variety of determination techniques, which each may rely on reasonable approximations, can result in cross section compilations that are not self-consistent [56]. Any approximations that are made in electron transport modelling software, such as the prevalent two-term approximation in the solution of Boltzmann's equation, can also affect the self-consistency of a cross section set [57]. Therefore, in lieu of an exact description of each scattering process, cross-sections must be derived or adjusted in the context of each other cross section within the set and the electron transport modelling technique used to ensure an accurate replication of experimental measurements.

1.2.2 Electron transport modelling techniques

The solution of Boltzmann's equation for electron motion through various media requires numerical techniques to solve the system of partial-differential equations [50, 58–61]. The solution of this equation often requires restrictive boundary conditions [57] that limit its applications. The most prominent and simplest application of Boltzmann equation solvers is for simulation of swarm experiments, which are discussed further in Section 1.2.3.

Since the 1950's, the modelling of equilibrium and non-equilibrium statistical mechanics has seen significant advances due to the ever increasing capability of computing technology and numerical techniques. The most prominent of which is the development of Monte Carlo methods by Metropolis *et al.* [62] and the molecular dynamics of Alder and Wainwright [63]. Monte Carlo methods in particular have found widespread use in research and industry due to their ability to utilise arbitrary boundary conditions and complex geometries [64–67]. Generally, Monte Carlo methods reconstruct the phase-space distribution function of Equation (1.1) through a direct simulation of an ensemble of probabilistic particles [68]. Using statistical techniques, macroscopic properties of a large number of simulated particles can then be determined from microscopic cross sections in highly complex systems that are often inaccessible by deterministic methods. In addition, Monte Carlo simulations often utilise what is known as the swarm approximation, which assumes a low electron-density limit such that electron-electron interactions are negligible. In this regime, each particle can be simulated independently, which reduces computational burden and enables parallel computing [66].

Particle-in-cell (PIC) simulations are commonly used in regimes where the swarm approximation is invalid, such as those found in plasmas [69]. Pioneered in the 1950s by Buneman and Dawson [70, 71], PIC techniques provide a full kinetic description of high-dimensional plasma along with the ability to model complex atomic and plasma-surface interactions. A key to these models is the simulation of 'superparticles', which each represent many physical particles, through a phase-space grid on which the solutions of Maxwell's equations are found. While advances in computation power and techniques continue to be made, intensive computations are still required for the simulation of sufficiently large systems.

Each of these modelling techniques, and others, play an important role in both the prediction of real world transport phenomena and the unravelling microscopic descriptions of particle transport. In Chapters 2 and 3, we develop and utilise a Monte Carlo simulation to aid in the design of, and conduct a feasibility study for, a new electron-liquid micro-jet scattering experiment. Following this, we use a multi-term Boltzmann equation solver developed by Stokes *et. al.* [1] to generate training samples of experimentally measured electron transport properties.

1.2.3 Current methods for determining electron scattering cross sections

Throughout the history of modelling electron transport, several theoretical, experimental and numerical techniques have been developed for the determination of electron scattering cross section sets. Together, these methods have created a wealth of cross sections that are systematically benchmarked and validated by experimental measurements and informed by theoretical approaches. The culmination of this body of work is evident from the substantial collaborative efforts made to maintain and expand the online database LXCat [52, 72, 73], which hosts both cross section and measured experimental values for use by the modelling community.

Several theoretical models for electron scattering cross section determination exist depending on the energy regime of interest. For energies much larger than the impact ionisation energy, methods such as the distorted-wave Born approximation and the independent-atom model screening-corrected additivity rule are commonly used [74]. Below these energies, solutions of the Schrödinger equation through grid-based techniques or close-coupling expansion is required [74]. Particularly for low energies between 0 eV and ionisation threshold however, these solutions methods prove difficult and computationally expensive. In addition, the calculation for complex molecular targets is currently limited due to computational limitations arising from the number of atoms and the asymmetric nature of most molecules [75].

Experimental techniques ensure the validity of scattering theory in addition to providing a tool for the derivation of that theory. Generally, there exist two main categories of experiments relevant to low-energy electron scattering; swarm and beam experiments.

Beam experiments generally consist of an intersecting beam of electrons and gaseous targets that are propelling through a vacuum chamber [44]. Figure 1.3 shows a simplified schematic representation of a beam scattering experiment. Each electron then typically undergoes a single scattering event before reaching a detector. The differential cross section is then proportional to the scattered intensity for a particular scattering angle and energy. While in idealised conditions the proportionality function is constant with respect to angle and energy [44], limitations in experimental design and equipment results in a non-trivial functional dependence [76]. To avoid this, a relative flow technique [76, 77] is utilised by determining the ratio of scattered intensities between the target and a standard gas, along with prior knowledge of the differential cross section for the standard gas. The relative flow technique thus requires that either the experimental conditions for each gas are identical, or that any differences are accounted for [78].

Deriving the integral cross section requires the full angular domain of the differential cross section to be defined. Measurements of the angular dependence of electron scattering in beam experiments are often limited by both the physical dimensions of detectors and the electron beam energy. To account for this, extrapolation of the scattering data is then required [44] which often utilise theoretical scattering data [79], a complex phase-shift analysis technique [80–82] or a non-linear least squares fit constrained by known properties of the gas. In addition to differential

and integral cross sections, total cross sections for a particular target can also be determined through single collision beam experiments [83].

The characterisation of cross sections for each scattering process can prove troublesome when similar energy loss thresholds exist for excitation collisions [44, 84]. In the ideal case, once the elastic differential cross section has been determined using the relative flow technique, the excitation differential cross section can then be determined through the ratio between elastic and excitation scattering intensities, which are found by measuring the energy dependence of the scattering intensity. Energy thresholds that are similar, particularly in the case of vibrational and rotational states, result in overlapping signals in the energy loss spectra. It then becomes necessary to conduct a deconvolution procedure to determine the true scattering intensity for a given process [44, 85].

As outlined previously, this work aims to investigate electron scattering from liquid targets. However, liquid-phase targets are not stable under vacuum conditions due to their high vapor pressures [26]. Over the last few decades, a new generation of photon scattering experiments from liquid beams have been developed for this purpose. In their pioneering work in the 1970s, Siegbahn and Siegbahn [86, 87] developed a liquid jet, which provided a stable scattering surface under vacuum, to measure binding energies in formamide ($NOCNH_2$). Using a fast flowing jet in combination with diameters in the order of millimeters, the authors found that laminar

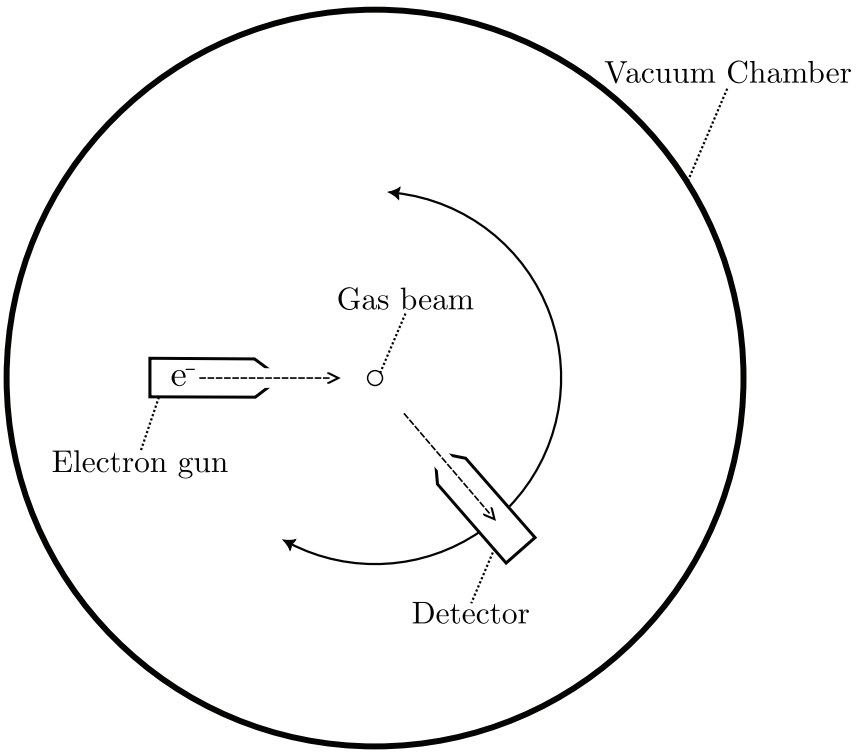

Figure 1.3: A schematic representation of a simplified beam experiment. An electron gun is used to scatter electrons from a column of gas molecules within a vacuum chamber. A detector is then typically rotated around the gas beam to scan the scattered electron signal.

flow can be achieved for a short distance before evaporating. Extending their work to high vapour pressure liquids such as water, Faubel *et al.* [26] reduced the jet to micrometer diameters to study the evaporation of water molecules. Since then, the so-called liquid micro-jet (LμJ) has be used to study a variety of targets through photoemission [33], photoelectron [88] and photoabsorption [89] techniques. Despite the use of LμJs in a broad range of studies of photon scattering, the direct measurement of electron scattering from a LμJ surface has yet to be studied.

The other main category of electron scattering experiments are swarm experiments, which operate in the 'swarm regime'. In this regime, the density of electrons are sufficiently small so as to have a negligible influence on the external electric field and other electrons within the swarm [90]. Generally, while a variety of configurations exist [91–97], an electric field is used to transition a swarm of electrons from thermal equilibrium and into a quasi-steady state in which energy losses from scattering events balance out the energy input from the electric field. A simplified schematic diagram is shown in Figure 1.4. From this state, measurements of different transport coefficients such as drift velocity and diffusion coefficients are made that describe the motion of the electron swarm. Each of these quantities can be derived through the phase-space distribution function from solutions of Boltzmann's equation using cross section data as an input. One can then evaluate the validity of a cross section set through a comparison of calculated and experimental transport coefficients. In addition, by varying the electric field, swarm measurements indirectly probe the energy dependence of electron scattering cross sections, which can be utilised to 'unfold' or extract complete cross section sets, or to validate sets derived by other methods [44].

The derivation of cross sections from transport coefficients measured across a range of electric fields is commonly known as the inverse swarm problem [1]. The presence of multiple

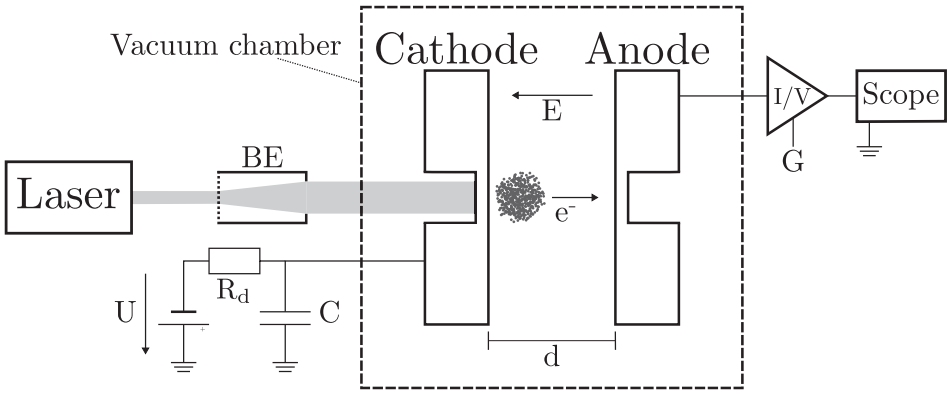

Figure 1.4: A schematic representation of a pulsed Townsend experiment. Two electrodes are mounted a distance, d, apart within a vacuum chamber. A high voltage source is connected to the cathode side with R_d and C serving to decouple the high voltage source from the signal circuit. An ultra-violet laser beam is broadened through a beam expander (BE) before impacting the photocathode and releasing electrons. Attached to the anode is a transimpedance amplifier or variable gain G and a scope to measure the displacement current [97].

scattering processes that exhibit similar properties, such as low threshold excitation collisions, can result in multiple complete cross-section sets that produce similar transport coefficients, rendering the problem ill-posed in nature [47, 98]. Considering this, there exists two prominent methods to derive or improve cross section sets; the iterative swarm technique and deep learning approaches.

The iterative swarm technique utilises an initial approximation of the cross section set and iteratively modifies the set to match experimental transport coefficients [45, 99–104]. This process can be computationally expensive and relies upon the intuition and experience of an expert, which can results in a tedious method and that is difficult to reproduce.

In the early 1990s, Morgan *et al.* [46] demonstrated a solution to the inverse swarm problem through an Artificial Neural Network trained on example cross sections and their associated transport coefficients. Recently, Stokes *et al.* [47] revisited the problem to leverage existing cross sections available on the online database LXCat [52, 72, 73] and advances in computational power and techniques to reduce the ill-posed nature of the inverse swarm problem. Jetly *et al.* [105] also used similar techniques to evaluate the possible improvements offered by select network architectures. To date, ANNs have been shown to aid in the development of cross section sets either through the perturbation of existing cross-section sets, or the derivation of a select few within the set [1, 106, 107]. However, the derivation of full cross-section sets remains elusive as the network is unable to reliably represent the ill-posed nature of the relation between transport coefficients and cross section sets.

In summary, the union of direct measurements from beam experiments, indirect measurements from swarm experiments, the iterative swarm technique and ANNs, forms a broad and powerful foundation for the derivation of accurate and complete cross section sets. In this work, we identify two main limitations of these techniques and present two phases of work that aim to address each limitation.

1.3 Structure of the thesis

The first phase of this work is motivated by the need to further our understanding of electron-liquid scattering dynamics. In partnership with Flinder's University, we present a new electron scattering vacuum chamber that utilises a LμJ designed by Advanced Microfluidic Systems GmbH [108]. The extension to direct electron scattering will provide further insights into the complex nature of electron scattering from molecular liquids. To achieve this, we develop a Monte Carlo simulation package to investigate the feasibility of using the experiment to inform the derivation of electron-liquid cross sections. In addition, we utilise the simulation to aid in the experimental design before conducting initial measurements of electron scattering through liquid H_2O at Flinder's University. Finally, we compare the measurements to simulated data using an

existing cross section set for H_2O.

The second branch of this work aims to improve and extend the existing ANN technique for solving the inverse swarm problem in order to broaden its application to increasingly complex molecular targets. We first demonstrate the limitations of the existing method and present extensions to the method to aid in reducing the ill-posed nature of the problem. Finally, we use the improved method to attempt to derive a complete cross-section set for HFO1234ze-E.

The scope of this thesis can be summarised by the following:

1. The development of a Monte Carlo simulation of non-equilibrium electron transport through gaseous and liquid environments with arbitrary boundary conditions.

2. Conducting a feasibility study of using deep learning to aid in the determination of electron-liquid scattering cross sections from a simulation electron-liquid micro-jet experiment.

3. Utilising the Monte Carlo simulation to inform the construction and design of the liquid micro-jet experiment.

4. Assembling the electron-liquid micro-jet experiment at Flinders University and presenting initial measurements of the electron signal as a function of energy loss and angle.

5. Improving upon the deep learning technique for determining scattering cross sections from transport coefficients in complex and ill-posed scenarios.

6. Applying the developed deep learning technique to the determination of electron scattering cross sections for HFO1234ze(E).

In Chapter 2, a Monte Carlo simulation of electron transport through a liquid micro-jet is detailed. The simulation is then used to generate training data for a neural network to investigate the feasibility of determining electron-liquid scattering cross sections from electron energy loss spectra measured from the liquid micro-jet. Chapter 3 details the construction of a new liquid micro-jet scattering experiment at Flinders University. Along with presenting some initial measurements from the experiment, the Monte Carlo simulation is also used to develop an understanding of its underlying mechanics and interpretation of the resulting energy loss functions.

In Chapter 4, a new deep learning technique is proposed that uses an iterative procedure along with a modified network architecture to determine cross sections from transport coefficients in highly ill-posed scenarios. To demonstrate the technique, we present a case study in which the cross-section set for electron scattering from methane is determined while only assuming knowledge of the energy loss thresholds. Following this in Chapter 5, we attempt the derivation of HFO1234ze(E)'s electron scattering cross section set using the proposed iterative technique.

In Chapter 6 we summarise the thesis and propose future work to extend and improve upon the work conducted here.

Chapter 2

Simulating the feasibility of using liquid micro-jets for determining electron–liquid scattering cross sections

This chapter includes the following publication:

[2] **D L Muccignat**, P W Stokes, and R D White, Simulating the Feasibility of Using Liquid Micro-Jets for Determining Electron–Liquid Scattering Cross sections, *International Journal of Molecular Sciences*, 6, 23, 2022

Electron motion through molecular liquid environments poses a unique problem for both electron scattering theory and experimental design. The work included in this chapter, and the following chapter, was conducted to aid in the design of, and conduct initial measurements for, a new electron-liquid scattering experiment that has been constructed in partnership with Flinders University.

In this chapter, we utilise and extend a Monte Carlo simulation package developed in previous work [109] to conduct a feasability study for the proposed experiment. The primary goal of this work was to determine the potential of measurements from such an experiment to inform electron-liquid scattering theory. The limitations of the experiment's design was also investigated by varying the simulated design and measurement uncertainties.

This chapter includes deep learning that was primarily conducted by P. W. Stokes. All other work described in this chapter is my own.

2.1 Introduction

The interaction of a low-temperature plasma with liquids is fundamental for numerous new and emerging technologies, finding applications in important domains, including environmental

remediation, and the synthesis of nanomaterials and medicine [110–118]. The goal of high-level optimisation, of the efficacy and selectivity, of these and future generation plasma–liquid applications depends on, among other things, a detailed understanding of the underlying fundamental nanoscale physics and associated predictive modelling, underpinned by accurate and complete transport theory and cross sections. The key driver to these applications is the role of electrons (and other radical species) at the plasma–liquid interface, but despite their central role, electron-induced transport and processes at the interface are not well understood [11].

Developing our understanding of electron transport into and within liquids is critical for enhancing the predictive power of plasma–liquid models. Fundamental to transport theory, which governs the motion of electrons into and within such environments, are complete and accurate sets of electron impact cross sections. While there is a wealth of knowledge of electron impact cross sections in the gas phase (e.g., databases such as LXCat [52,72]), the same is not true for the liquid environments. The scattering and transport theory of pre-solvated electrons in non-polar liquids is reaching some level of maturity (see the *ab initio* treatment by the authors [24, 25]), however this is not the case for polar liquids. An existing Monte Carlo simulation of low-energy electrons in liquid water [119] ignored many physical processes, that are relevant to developing appropriate scattering theory. Furthermore, current models use cross sections calculated in the gas phase, or through electron reflection measurements from amorphous ice [22]. The absence of liquid phase data represents a large knowledge gap in the literature, and experiments proposed in this manuscript aim to address, at least in part, this knowledge gap.

Here, we propose a new experimental technique that extends gas phase beam experiment methodologies [44] to include electron scattering from liquid surfaces, through the use of liquid micro-jets (LμJs). A constant replenishment of liquid, a small surface area, and a laminar flow enable the scattering of particles from a smooth and stable liquid surface, whilst operating in a vacuum environment. Until now, LμJ investigations have focused primarily on photon and photoelectron scattering [31, 35, 39, 120–129]. In this work, we introduce electron scattering from LμJs and investigate the feasibility of developing effective electron–liquid cross sections from the measured electron energy loss spectra (EELS). Unlike gas phase experiments, which are designed to ensure single scattering processes only, the proposed experiment is necessarily multi-scattering, with electrons being scattered from the surface and bulk atoms/molecules. The connection of this with traditional (multiple collision) swarm experiments [92, 130–132] is thus clear.

Swarm experiments have proven to be critical in the development of accurate cross section sets [44]. In electron swarm experiments, electrons are driven through a gaseous (or liquid) medium by an applied electric field, and macroscopic descriptors such as current, drift velocity, and diffusion coefficients are determined. Simulation techniques then evaluate the accuracy and self-consistency of the cross section sets through comparisons of the transport coefficients. The

same techniques can be used, in principle, to iteratively improve or develop cross section sets [133–138], although the question of degeneracy in the cross section set remains open, and other means are usually required to minimise this. Recent studies have shown promising applications of neural networks (NN), toward improving cross section sets through swarm transport data [1, 47, 105–107, 139]. Utilising a similar NN methodology, along with energy loss spectra from a LμJ experiment, we propose the generation of cross section sets for electrons within a liquid environment. To facilitate this, a benchmarked Monte Carlo simulation technique, for simulating electron transport in liquid environments [140], has been developed and implemented for this study, with extensions to calculate EELS arising from the scattering of electrons from an LμJ.

The paper is organised as follows. In Section 2.2, we provide a summary of LμJs and their implementation in the proposed experiment. In Section 2.3, we outline the Monte Carlo (MC) simulation method utilised here and discuss the characterisation of bulk liquid and interfacial effects. The characteristic signatures of the various multiple scattering elements on the EELS are also discussed. In Section 2.5, we use the developed Monte Carlo software to train a neural network to predict neon's elastic and ionisation cross sections as a proof-of-concept. Finally, in Section 2.6, we provide some concluding premarks.

2.2 The proposed electron–liquid micro-jet scattering experiment

2.2.1 Liquid micro-jets

Liquid micro-jets were first developed to overcome the limitations of probing liquids under vacuum conditions, which are often required by scattering experiments [86]. Due to the high vapour pressures found in liquids, additional treatment is required to ensure a stable surface within vacuum conditions, and hence the developments of the liquid jets. In our proposed experiment, a replenishing and sufficiently thin liquid source, exhibiting laminar flow, facilitates a smooth and stable scattering surface within a vacuum environment [26].

Siegbahn and Siegbahn [86] first utilised a replenishing 0.2 mm diameter liquid jet, and scattered electrons from that source to measure binding energies in formamide ($HOCNH_2$). *In vacuo* experiments were initially limited to low vapour pressure liquids, to avoid immediate freezing and/or evaporation. For high vapour pressure liquids such as water, a further reduction of exposed surface area is required to maintain a free vacuum surface [121]. To this end, significantly smaller ($\sim$10 μm) liquid micro-jets were first developed to measure the velocity distributions of vapour molecules, while ensuring inter-molecular collisions were minimised [26]. Extending this, a focusing gas surrounding the nozzle was implemented to increase the length and decrease the diameter of the jet substantially [141–143]. Flat LμJs were also developed

from the collision of two micro-jets, which results in a sheet-like scattering surface [144]. Additionally, cryogenic jet systems enable the use of super-cooled liquids with jet diameters reaching 1 µm [145, 146]. It is clear that a wide array of configurations are achievable, and can be tailored towards the desired experiment.

Until now, applications of the aforementioned LµJ designs include an array of photoelectron spectroscopy experiments, to measure properties such as binding energies and hydrogen bonding [31, 35, 39, 120–129]. Other LµJ experiments include mass spectrometry [147], enhanced X-ray production [148–151], X-ray emission/absorption, to probe electronic structure and molecule orientation [152–154], to study the molecular dynamics of evaporation [155], electrokinetic power generation [156, 157], and drug delivery alternatives [158]. For further general reading, one is directed to the summary papers cited here [33, 38, 124].

Scattering simulations, such as the MC code developed at James Cook University, rely on the characterisation of the LµJ features. Liquid dynamics studies of LµJs found jet length stability on the order of millimetres. In one study [159], source widths of 10, 20 and 50 µm, along with velocities ranging between 25 and 150 ms^{-1}, were trialled for each diameter. A limited laminar flow was achieved with jet lengths between 1 and 15 mm. After emergence from a circular nozzle, the jet undergoes contraction to a final cross sectional size due to surface tension forces [160]. Typical contraction values were found to range between 90% and 60% [159] of the original source width, after which capillary forces break the jet into droplets through a tendency to try and reduce surface energy [160].

Within the liquid, charge build-up, and the existence of a streaming potential, due to electrokinetic charging, can hinder the accurate simulation of charged particle transport. A streaming potential is produced when a pressurised liquid is forced through the nozzle, which disrupts the electric double layer created between the liquid and the inner wall of the nozzle [161, 162]. For liquid water, the magnitude of this streaming potential exceeds 60 V depending on the jet velocity and diameter [31, 162]. The addition of an electrolyte has since been shown to minimise this effect [162]. Additionally, the production of electrons within an insulating medium such as water will produce a current and subsequent surface potential [33]. The magnitude of this effect will depend on the application and relevant time scales.

2.2.2 Crossed-beam electron scattering from liquid micro-jets

In our proposed experimental work, we will extend existing crossed-beam methodologies from gas to liquid environments, utilising liquid micro-jets to measure differential electron energy loss spectra (EELS), as shown schematically in Figure 2.1. The liquid would be propelled into a vacuum environment through a 15 µm circular nozzle to produce a continuous, stable, and smooth scattering surface. In this work, we assume that the jet diameter is the same as the nozzle diameter. As noted previously, this jet remains stable for several millimetres before decaying

into droplets. Evaporation at the surface and the tapering of the jet's diameter are neglected in the current work, as the characterisation of such parameters was not available, and their effects on the model are expected to be minimal. Electrons, sourced through thermionic emission from a tungsten filament, and collimated and transported by a series of DC-potential elements, are then propelled through the vacuum normal to the jet's direction, to undergo multiple surface and bulk scattering events before escaping (and being collected by one or more detectors) or solvating within the liquid. For the foreshadowed work, an electron source with an energy full width at half maximum (FWHM) of 0.5 eV will be used [163].

Once an electron escapes the jet, a scattered electron detector will resolve both its energy, ε, and scattering angle, χ, with a resolution of 0.8 eV (FWHM) and 1°, respectively [163].

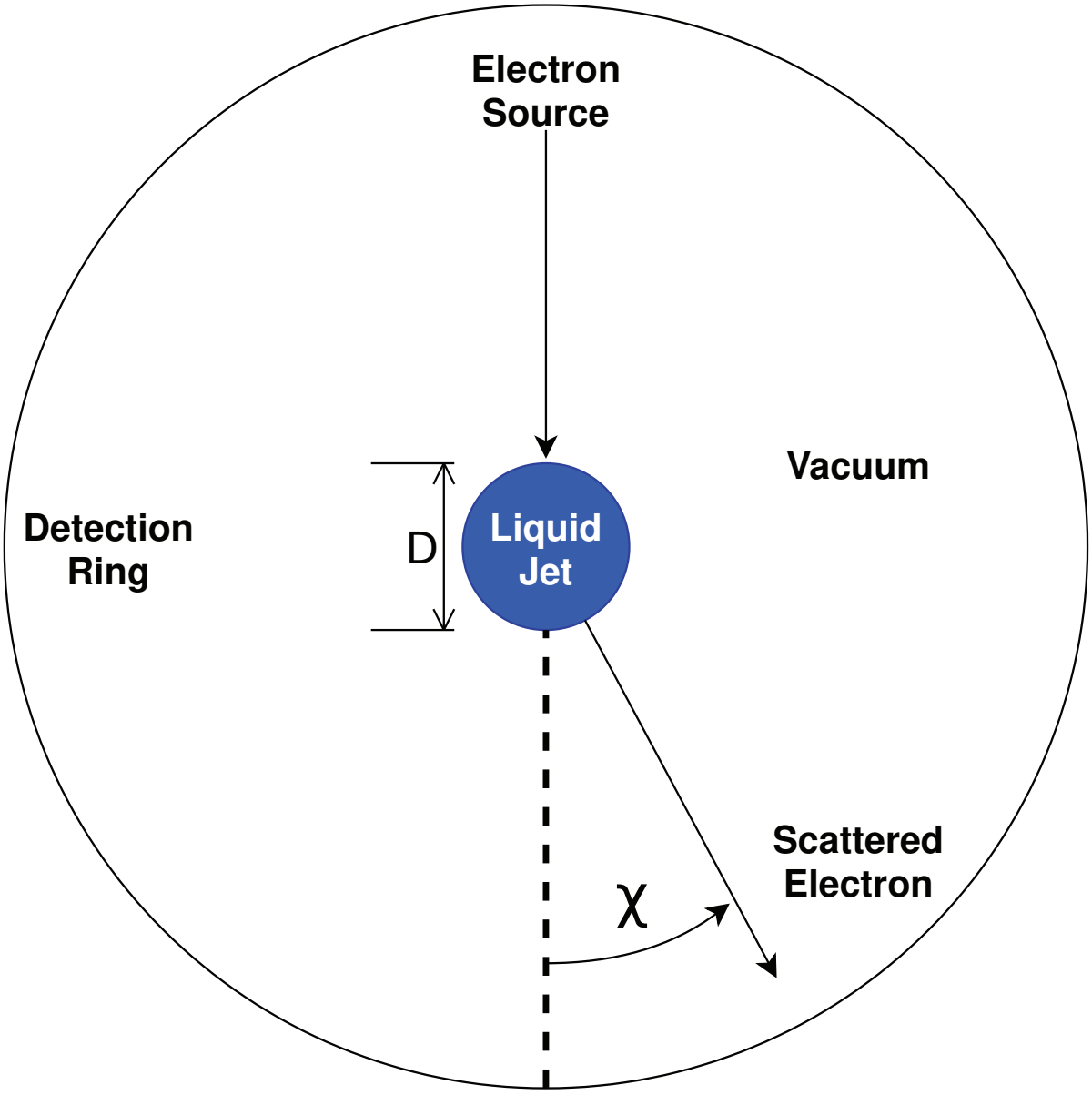

Figure 2.1: Diagram of crossed-beam electron scattering from a liquid micro-jet. The liquid is propelled into the page, while detectors are positioned normal to the liquid surface.

Through the detection of both the energy and angular dependencies, EELS provides a high degree of insight into the underlying electron scattering cross sections and their associated dynamics. This combination of the electron gun and scattered electron detector provides a combined energy resolution of 0.9 eV. We note that, with crossed-beam experiments, some restrictions will inevitably be placed on the available detection angles. This is simply due to the physical size of the electron source, the electron detector(s), and LμJ. Additionally, while an angle-resolved EELS provides sufficient information for the derivation of differential cross sections within the gas phase, multiple scattering effects in liquids present significant challenges when deconstructing EELS into complete (differential) cross section sets due to the high degrees of convolution arising. The extent of this convolution is investigated, in part, in Appendix 2.4.

2.2.3 Extraction of cross section sets from EELS

The derivation of cross sections from a reflected EELS measurement is akin to the 'Inverse Milne Problem', which consists of deriving the reflected EELS from a 'half-plane' medium, of finite or infinite depth from $z = 0$ to $z = L$ (where L is the half-plane depth), and extends to infinity in all other directions [164]. Outside the half-plane, a vacuum exists from which particles are propelled into the half-plane. The presence of high multiple-scattering at large L, relative to the scattering length, results in a complex combinatorial problem with a restricted set of observables, thanks to a reliance on external measurements [164].

The vast majority of treatments involve energy-independent radiative transfer [164, 165] and neutron scattering [166, 167]. The inclusion of energy dependencies was conceptually treated [168], with strict delta function requirements placed on both the source and detector, in order to derive total and differential cross sections. In other studies, sufficiently thin (10–100 nm) solid films were used to derive surface and bulk inelastic mean free paths [169–171], assuming a knowledge of the elastic cross section. Likewise, cross sections for amorphous ice films were derived under a two-stream assumption, along with a variation of film thickness between 0 and 5.456 nm [22, 172, 173]. While the extension of these techniques towards LμJs may be feasible, other indirect approaches, such as Monte Carlo simulations, together with machine learning, could simplify the methodology significantly.

In multiple studies [1, 47, 105, 106, 139], machine learning was applied to the inversion of transport coefficients found through swarm experiments. While swarm transport coefficient measurements differ in nature to EELS, they each represent an ill-posed inversion problem associated with high degrees of multiple scattering. An extension of the current methodology towards liquid phase EELS requires a sufficiently large training dataset, which is facilitated through a highly configurable non-equilibrium Monte Carlo simulation of electron transport developed for this project. In this study, we thus seek an implicit cross section extraction technique utilising a neural network trained through Monte Carlo simulations of an LμJ. In what

follows, we outline the Monte Carlo simulation employed, and its application to the proposed LμJ measurements, before applying machine learning to this ill-posed inverse problem of determining cross sections from LμJ-measured EELS.

2.3 Simulation of electron transport through liquid micro-jets

Machine learning requires a substantial volume of training data to ensure a robust fitting process. To generate these data efficiently, a Monte Carlo simulation method was developed. Monte Carlo (MC) simulations provide flexible environments in which the manipulation of spatial and temporal parameters is both efficient and straightforward. LμJs inherently require specific and precise spatial variation in terms of the neutral density, and hence, an MC simulation is well suited for the task. The simulation technique is discussed in detail in [140], hence, here, we detail its application to LμJs, while a section of benchmark results is presented in Appendix A.1.

2.3.1 Liquid dynamics

Relatively low-density gaseous environments involve an inherent assumption that each scattering event involves instantaneous localised interactions. In liquid environments, however, the de Broglie wavelength of the electron can be smaller than, or of the same order as, the inter-particle spacing and the mean free path, which necessitates modified coherent collision dynamics. To account for coherent scattering, a new method was recently developed which incorporated a structure factor modified cross section [140]. Through this, the macroscopic effects of coherent scattering are realised, while retaining the efficiency of effective single particle scattering events. Therefore, the relative simplicity of modelling single particle-particle collisions is maintained, while replicating the macroscopic effects of multiple scattering. Through an integral structure factor [140, 174], elastic collisions are split into three collisional processes, which are weighted by an angle-integrated structure factor, $\Gamma(\varepsilon)$, produced through either theoretical or independent experimental techniques.

As a result of these microscopic processes, electron scattering through liquids is accurately simulated, given an appropriate structure factor. For real systems, experimentally measured structure factors are available through X-ray or neutron scattering [175–177]. While its functional form will vary, the methodology remains the same. Previously [140], it was shown that these processes match the required momentum and energy transfers derived using Boltzmann's equation [140]. While isotropic scattering was assumed, the proof of principle was extended by the present authors to show its validity for the use of differential cross sections. In the current work, we investigate structure effects upon measured spectra, while its implementation in our machine learning model is left for future study.

2.3.2 Interfacial dynamics

In addition to liquid dynamics, interfacial effects must be considered in the simulation of LμJs. A recent study investigated density-dependent inter-facial effects on electron transport [178]. Due to a change in de-localised electron energy across the interface, a density-dependent (n_0), and hence spatially-dependent potential $V_0(n_0(\vec{r}))$, exists, which produces an effective electric field $E_0(\tilde{r}) = -\nabla V_0(\vec{r})$. A spatial density dependency was thus implemented within the MC simulation, along with the resulting potential, and hence electric field. In that study [178], it was found that a discrete change in density, and hence potential, did not significantly change the path and associated transport dynamics of such particles when compared to a realistic functional form, which in addition to computational considerations, motivated the use of a step function form for the change in density in the current work. Additionally, any variation in the potential resulting from the density change is left for future extensions of this work.

2.3.3 Experimental parameters

Under realistic experimental conditions, detector resolutions and uncertainties will impact the prominence of correlations between EELS and their corresponding cross sections. A critical factor for extracting important information is the experimental energy resolution of both the electron source and detector. In the models discussed above, an approximation to the energy spread of the electron source was incorporated by sampling a Gaussian distribution of FWHM of 0.5 eV. In Figure 2.2, an experimentally feasible combined EELS energy resolution of 0.9 eV [163], which is incorporated into the simulations in what follows in Section 2.5, alongside a hypothetical resolution of 0.1 eV, are shown for comparison. Distinct information loss occurs in the 0.9 eV energy-resolved spectra, for inelastic peaks with similar threshold energies, when compared to the 0.1 eV spectra. This clearly indicates that the foreshadowed experimental measurements should be conducted with as narrow an energy resolution as possible.

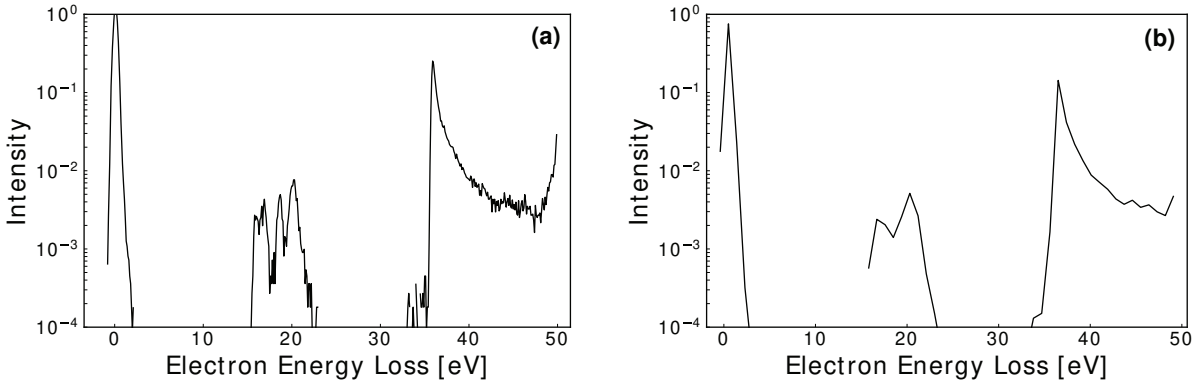

Figure 2.2: An example EELS comparison between a 0.1 eV energy resolution (**a**) and a 0.9 eV energy resolution (**b**), for an initial electron energy of 50 eV scattering from neon [179]. Significant information is lost at 0.9 eV, especially when the peaks are in close proximity.

2.3.4 Liquid micro-jet parameters

To develop training data, simulated electrons were scattered through a cylindrical liquid micro-jet using the benchmarked MC simulation. Each electron, with initial energy ε_0, was fired along the z-axis towards a 15 µm jet, which was directed along the x-axis. It was assumed that the motion of the jet ($\sim$100 ms^{-1}) has a negligible effect on the measured EELS, as deflection angles were measured within the z-y plane and integrated over the x-axis.

Scattered electrons are detected once they reach a radial distance sufficiently far from the jet, such that the angle measured was relative to the jet's centre in the z-y plane. The EELS was then integrated over the x-axis, such that there existed a (χ, ε) dependence, where ε is the electron's final energy, before integrating over χ. Each electron was simulated until it was detected, or until it lost sufficient energy, such that the probability of escape was negligible.

As a proof-of-concept for this work, we assume that the jet is gaseous neon at a liquid density of 2.13×10^{28} m^{-3}, and at a temperature of 0 K. Based on the proposed experiment [163], the energy variance of the initial electrons was sampled from a Gaussian with an FWHM of 0.5 eV, centred around the initial energy ε_0, while its spatial extent was assumed to be a delta function directed along the surface normal. This serves as a first approximation to the experimental work, where there will be an electron beam, with a finite diameter of 1 mm, incident on the LµJ.

2.4 Electron energy loss spectra: sensitivity to the scattering dynamics and experimental parameters

In this study we seek an implicit relationship between the EELS and its underlying cross section set through the use of demonstrative cross section sets. In what follows we now systematically investigate the ramifications of individual changes to the cross section sets upon the EELS. For the conditions under investigation, no electron transmission through the beam of 15 µm was observed.

2.4.1 Magnitude and energy dependence of elastic and excitation cross sections on the EELS

Effect of the elastic cross section dependence on the EELS

In order to de-convolute features present within the EELS and their relationship with the underlying cross section set, each parameter within the model was isolated and tested for its effect upon the EELS. The first model considered was a constant elastic cross section:

$$\sigma_{elastic} = \sigma_0 \text{Å}^2,$$

where σ_0 was varied to determine the impact of the cross section magnitude on the simulated EELS. As expected, an invariance with respect to magnitude was observed as no transmission occurred and thus cross section magnitude changes will scale the problem without affecting the reflected intensities. The second elastic model considers the effect of the energy dependence of the cross section. Specifically, in Figure 2.3 we compare the effect of various power laws, through the elastic only model:

$$\sigma_{elastic} = \varepsilon^l \, \text{Å}^2, \tag{2.1}$$

where ε is energy in eV and l is varied in accordance with the legend of Figure 2.3. Each spectrum showed an invariance with respect to the power law at low energy losses, and exhibited intensity decay rates at higher energy loss that were dependent upon the power law used. The magnitude of this effect depends on the energy dependence of the cross section's derivative, and gradual changes were found to have a minimal impact upon the spectra.

To explain this physically, one can imagine the swarm of electrons as an expanding sphere in Cartesian space. Figure 2.4 shows the electron swarm within the jet at time 2.83×10^{-11} s after impact with a LμJ for $l \in [-1, 0, 1]$. A constant mean free path with energy loss ($l = 0$) results in considerable back scattering after jet surface impact, and the remaining electron cloud travels further inward with a constant expansion rate. Nothing inherently changes during their flight and the back-scattering flux is proportional to the number of remaining electrons within the jet. A decreasing mean free path with energy loss ($l = -1$) results in a diminishing rate of expansion, that results in a relatively smaller back-scattered intensity. In contrast to this, an increasing mean free path with energy loss ($l = 1$) accelerates the rate of expansion, resulting in an increased likelihood of back scattering out of the jet.

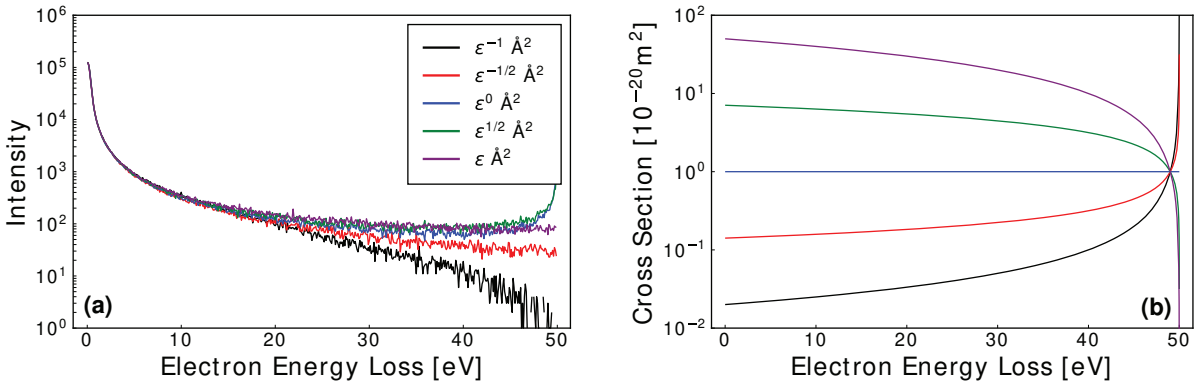

Figure 2.3: Electron Energy Loss Spectra (**a**), and their corresponding elastic cross sections (**b**), for various power laws (see legend of (**a**)). An initial energy of 50 eV was used. Each spectrum initially remains the same between each power law, before a divergence is observed at higher energy loss. Each spectrum for a single cross section remains independent of the cross section magnitude; however evident here is a dependence upon each cross section derivative.

Effect of the excitation cross section dependence on the EELS

Excitation cross sections are introduced through the model:

$$\sigma_{elastic} = 10\,\text{Å}^2,$$
$$\sigma_{excitaiton} = \begin{cases} 0, & \varepsilon < 5\,\text{eV} \\ \sigma_0\,\text{Å}^2, & \varepsilon > 5\,\text{eV} \end{cases},$$

where σ_0 is varied to investigate the relative elastic/excitation cross section magnitudes and their effects on the EELS. As shown in Figure 2.5, it is clear that the intensity peak at 0 eV energy loss is proportional to the elastic cross section. Inelastic peaks are then observed at intervals equal to the 5 eV threshold energy. Once the energy of the electrons falls below that threshold, energy loss is minimal due to the restriction to elastic collisions. This results in a high energy loss peak that is proportional to the elastic mean free path. Additionally, as the inelastic cross section magnitude increases, the below threshold peak at 45 eV energy loss also increases due to an increased energy loss rate. Note that while the initial energy in all cases is sampled from a Gaussian, energy loss is defined as the difference between the average initial energy and final energy, which can result in an apparent negative energy loss in some cases.

As expected, the relative elastic/excitation cross section magnitude is correlated with each peak found in the EELS. As shown previously, in a single collision regime and within an ideal environment, direct relationships exist between the two quantities. However, the introduction of multiple scattering convolutes their dependence. While a clear trend also exists here, excitation

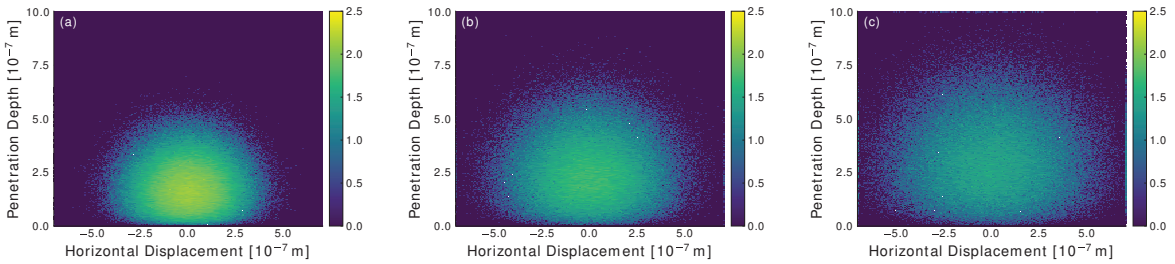

Figure 2.4: Heatmap of the electron cloud at 2.83×10^{-11} s after impact, with the LμJ surface for $l = -1$ (**a**), $l = 0$ (**b**) and $l = 1$ (**c**) according to Equation (2.1). For this model, 10^7 1 eV electrons were simulated through a 15 μm LμJ with the jet directed into the page. The electron counts for each corresponding depth and horizontal displacement were then recorded. A $\log_{10}$ transform of non-zero values was then performed for visualisation purposes. Initially, in each scenario, the elastic cross section is equal due to the initial energy of 1 eV. In (**a**), the electron swarm loses energy through collisions with the background gas and experiences an increasing cross section (decreasing mean free path) with energy loss, which results in a decreased expansion of the electron swarm. In (**b**), the electron swarm experiences a constant cross section (constant mean free path) with energy loss, which results in a steady expansion of the electron swarm. Finally, in (**c**), the electron swarm experiences a decreasing cross section (increasing mean free path) with energy loss, which results in an increased expansion of the electron swarm.

processes within a multiple scattering environment introduce peak dependencies upon relative cross section magnitudes at multiple energies and results in a large combinatorial problem.

Shown in Figure 2.6, we expand the previous model to include energy dependencies with multiple cross sections through the following model:

$$\sigma_{elastic} = \varepsilon^x \text{Å}^2,$$
$$\sigma_{inelastic} = \begin{cases} 0, & \varepsilon < 5\,\text{eV} \\ \varepsilon^x \text{Å}^2, & \varepsilon > 5\,\text{eV} \end{cases},$$

where x is varied according to the legend of Figure 2.6. No change in the elastic peak at 0 eV is observed, however each subsequent peak decays at a rate dependent upon the power law used.

For comparison, integration over the fitted exponential modified Gaussians for each peak are shown in the right hand graph of Figure 2.6 (note that for $x = -1$, the 40 eV peak was not found by the fitting algorithm). In contrast to the single elastic cross section result outlined in Appendix 2.4.1, a distinct correlation was found. The introduction of an inelastic process dramatically

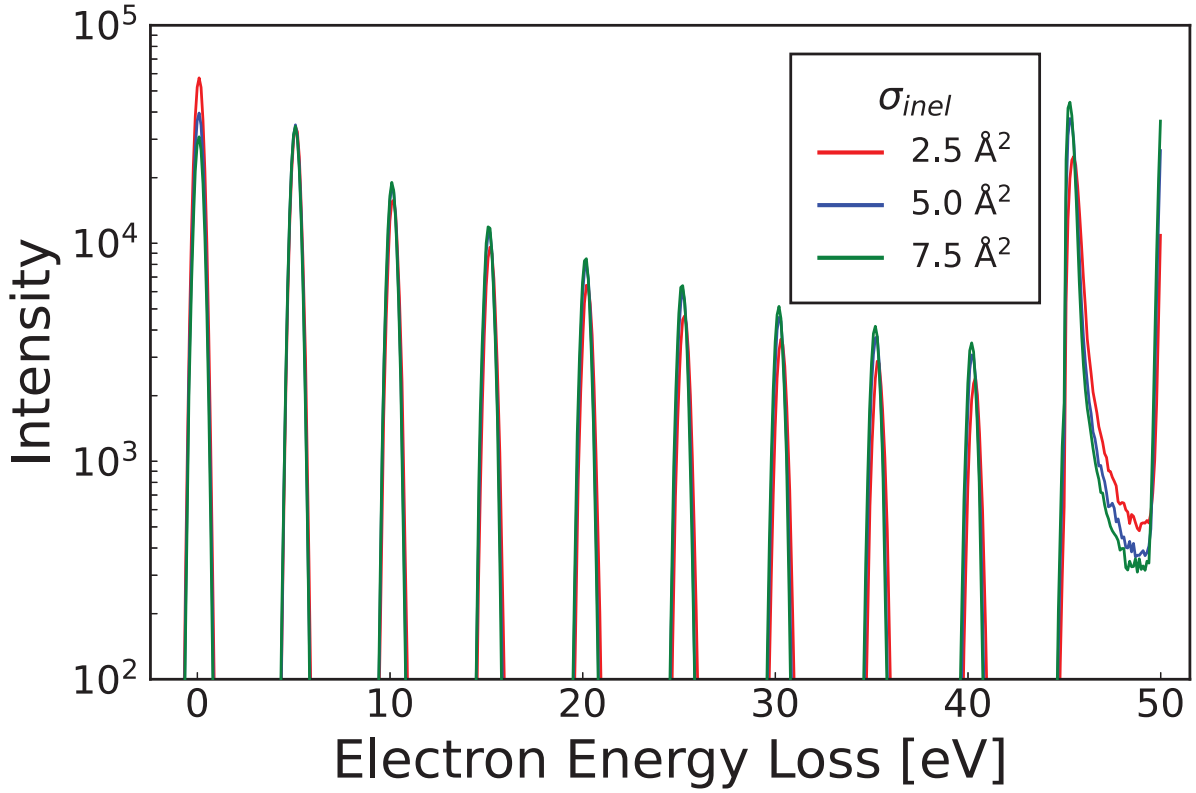

Figure 2.5: EELS for elastic and a single inelastic cross section, with varying relative magnitude. An initial energy of 50 eV was used, with an inelastic threshold of 5 eV. The inelastic cross section magnitude is shown in the legend. At 0 eV energy loss an elastic peak exists, followed by threshold separated sequential inelastic peaks. Additionally, after 45 eV of energy loss, electrons exclusively undergo elastic collisions which results in an increased intensity due to their minimal energy loss. Evident in this figure is a relative elastic to inelastic ratio dependence of the EELS upon the relative magnitude of the respective cross sections.

increases the energy loss rate, which in turn will amplify the effects of an energy-dependent cross section. A direct relationship remains convoluted, however, as the magnitude and energy dependence of the individual cross sections, within a given cross section set, will vary, resulting in significant degeneracy issues.

Of particular interest is the below threshold peak at 45 eV in the EELS. Here it was found that while their areas remain relatively constant, there exists a relationship between their asymmetric nature and the power law used. The exact nature of the relationship depends upon each cross section's, and hence mean free path's, derivative with respect to energy. As discussed in Appendix 2.4.1, when compared to scattering with a constant mean free path, an increasing mean free path with each subsequent collision increases the expansion rate for the electron swarm due to the reduced collisional impediment, resulting in a larger scattered intensity. As the swarm falls below the threshold energies, where energy loss is minimal, fewer electrons remain in the liquid when compared with the result for the constant mean free path model and thus a decreased scattered intensity was observed. A decreasing mean free path with energy loss slows the rate at which the swarm expands, which results in a reduced intensity when compared to a constant mean free path. As the mean free path decreases even further at lower energies, the probability of escape reduces even further, which effectively traps the electron swarm within the liquid.

Effect of the ionisation cross section dependence on the EELS

To investigate ionisation collisions, and their effect upon the EELS, the following model was used:

$$\sigma_{elastic} = 1\,\text{Å}^2,$$
$$\sigma_{ionisation} = \begin{cases} 0, & \varepsilon < 25\,\text{eV} \\ 1\,\text{Å}^2, & \varepsilon > 25\,\text{eV} \end{cases},$$

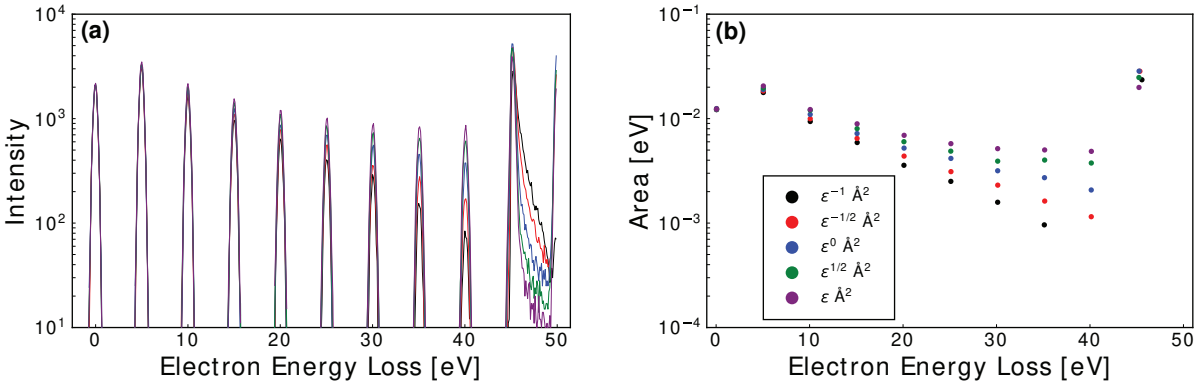

Figure 2.6: Simulated EELS (**a**), and area under each peak (**b**), as a function of the electron energy loss for a single elastic and inelastic cross section, but both now with an equal power law functional form defined by the legend in (**b**). A distinct trend is observed, where the power law is proportional to the each cross section's slope.

with varying ionisation energy-sharing profiles between the primary and secondary electrons as shown in Figure 2.7. At this point, it is important to consider the effects of fractional energy loss on the multiple scattering features of the EELS. Energy loss is largely driven by threshold excitations, energy partitioning losses (i.e., distribution of the excess energy between the scattered and ejected electrons) and kinetic energy exchange between the target and the electron (see Equation (A.12)). Energy exchange losses are proportional to the incident energy of the electron (and the mass ratio with the target atom/molecules), and result in a narrowing of the features (i.e., a reduction in average energy loss) at low energies.

While excitation collisions introduce relatively simple peaks within the spectra, ionisation collisions introduce unique features depending upon the energy-sharing profile between the primary and secondary electrons. Four model scenarios were considered (see Figure 2.7; equal, biased, uniform and skewed sharing). Equal energy sharing (i.e., a 50–50% energy partition) between the primary and secondary electrons resulted in a single peak at an energy loss of the ionisation threshold plus half the ionisation threshold energy. Once below the energy threshold, electrons undergo elastic collisions at minimal energy loss resulting in a relatively large ionisation peak. Biased energy sharing was represented through a 90–10% sharing partition, resulting in separate peaks that exhibit broadening due to energy exchange losses. While the observed amplitudes and full width half maximums vary according to the aforementioned narrowing effect, the total peak area was equal in accordance with the equal cross sectional magnitudes used (see Figure 2.7).

As expected, a uniform probability of all sharing ratios resulted in a shoulder beginning at the ionisation threshold energy loss. A gradual increase was observed in the shoulder intensity once again, due to the energy exchange losses discussed above. Finally, a normalised exponential cumulative distribution function was utilised to emulate a skewed energy sharing distribution for the ionisation process. A semi-symmetric saddle shape was observed, with an asymmetry again driven through energy exchange losses.

2.4.2 Anisotropy in the scattering dynamics

Coherent scattering effects

As discussed previously, modelling coherent scattering in liquid environments was achieved through the addition of liquid structure factors [140, 174]. Figure 2.8 compares how those coherent liquid scattering structure factors affect the present EELS utilising the model:

$$\sigma_{elastic} = 6\,\text{Å}^2,$$
$$\sigma_{inelastic} = \begin{cases} 0, & \varepsilon < 2\,\text{eV} \\ 0.1\,\text{Å}^2, & \varepsilon > 2\,\text{eV} \end{cases},$$

with the Percus-Yevick structure factor [140]. Coherent scattering effects are isolated to the low energy regime ($< 5\,\text{eV}$), and hence its effects were limited outside that range. At low energies, electrons tend to coherently scatter through multiple targets, with little angle change, and hence will travel further in a particular direction when compared to isotropic scattering binary collisions. It was found that initial energies below 5 eV resulted in a decreased surface scattering intensity, due to enhanced forward scattering. Multiple scattering then randomises the preferred direction, such that the swarm will expand in size faster than the isotropic equivalent, which resulted in an increased intensity observed at the higher energy loss.

Differential cross section effects

Anisotropic scattering was included through a differential cross section (DCS) in the following model scenario:

$$\sigma_{elastic} = 6\,\text{Å}^2,$$
$$\sigma_{inelastic} = \begin{cases} 0, & \varepsilon < 2\,\text{eV} \\ 0.1\,\text{Å}^2, & \varepsilon > 2\,\text{eV} \end{cases},$$

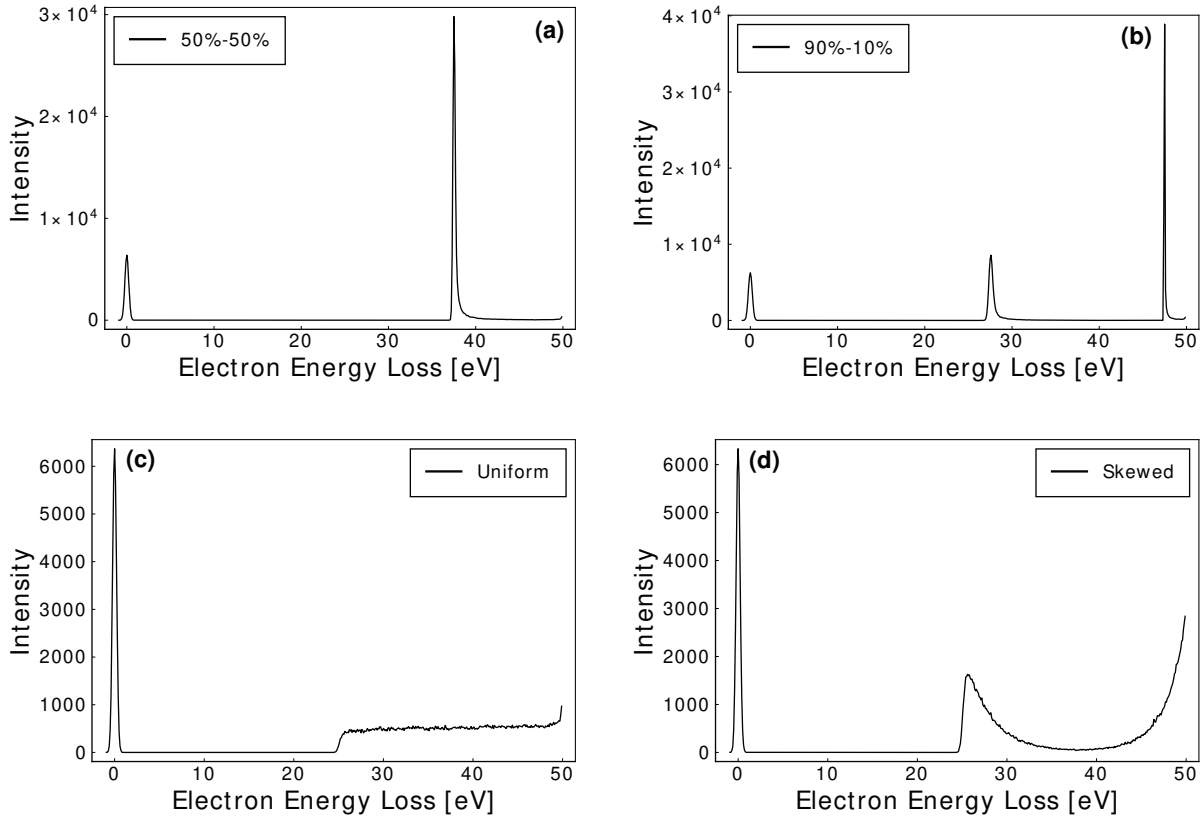

Figure 2.7: EELS for an elastic scattering and ionisation model. Initial energy was set to 50 eV, with an ionisation threshold of 25 eV. The energy sharing ratios, between the primary and secondary electrons, were set to 50–50% (**a**), 90–10% (**b**), uniformly randomised (**c**), and skewed randomisation in accordance to a normalised exponential cumulative distribution function (**d**).

where varying degrees of forward scattering were considered and represented through a normalised powers of the cosχ function, where χ is relative to the incident direction of motion. Each modified DCS was applied to both the elastic and inelastic cross sections.

Similar to coherent scattering effects, an initial decrease in intensity at 0 eV energy loss was observed in Figure 2.9 along with an increased signal at higher energy loss that is proportional to the degree of forward scattering. The explanation of that latter observation is the same as in Appendix 2.4.2, except now it is applicable to all incident energies.

2.5 Determining cross sections from electron energy loss spectra using machine learning

Through a sensitivity analysis, which is presented in Appendix 2.4, we show that there exists a highly complex and degenerate correlation between the energy loss spectra and their underlying cross sections. It was found that, while absolute magnitudes had little effect on the EELS, the effects of both relative magnitudes and energy dependencies of the cross section were relatively significant. Deriving cross section sets directly from EELS, without prior knowledge, is therefore a formidable task.

In this section, we apply machine learning to this ill-posed inverse problem of determining cross sections from LμJ-measured EELS. As a proof-of-concept, we initially consider the task of determining electron–Ne cross sections from EELS that are calculated using our Monte Carlo simulation. In what follows, we assume gas phase isotropic scattering, due to the present limited availability of liquid phase electron scattering and differential cross sections, the inclusion of which remains a critical step towards the determination of liquid phase electron cross sections. We note that, given appropriate liquid phase test data, the methodology that we propose here

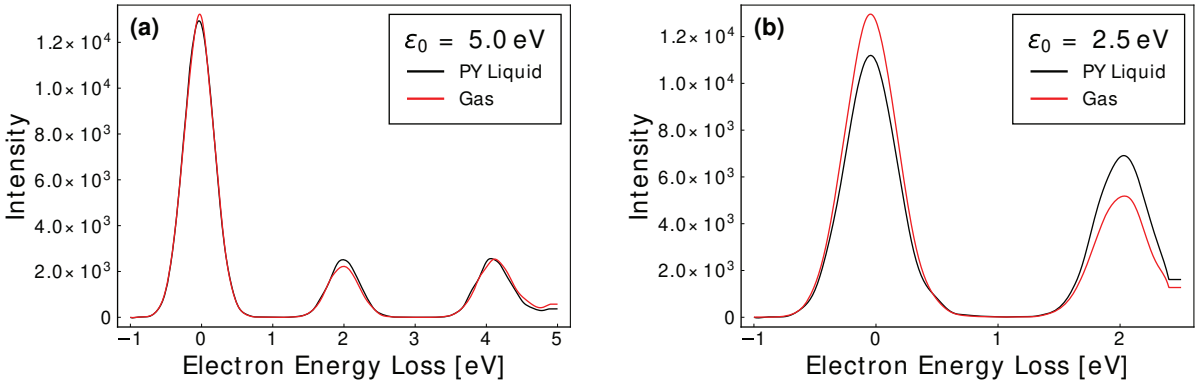

Figure 2.8: An elastic and inelastic EELS, with the Percus-Yevick liquid structure factor result (Black) compared with the equivalent gas phase result (Red). In each model, an inelastic threshold of 2 eV was used with incident energies of 5 eV (**a**), and 2.5 eV (**b**). As coherent scattering is predominantly restricted to low energies ($<$ 5 eV), its effects are minimal when the incident energies exist outside that domain.

could be used to produce effective liquid phase electron cross sections.

2.5.1 Machine learning methodology

To obtain a solution to the "inverse EELS problem", we apply the same general machine learning approach as proposed by Stokes *et al.* [1, 47, 106, 107], for the analysis of electron swarm transport data, and utilise an artificial neural network of the form:

$$\mathbf{y}(\mathbf{x}) = (\mathbf{A}_4 \circ \text{mish} \circ \mathbf{A}_3 \circ \text{mish} \circ \mathbf{A}_2 \circ \text{mish} \circ \mathbf{A}_1)(\mathbf{x}), \tag{2.2}$$

where $\mathbf{A}_n(\mathbf{x}) \equiv \mathbf{W}_n\mathbf{x} + \mathbf{b}_n$ are affine mappings defined by dense *weight* matrices $\mathbf{W}_n$ and *bias* vectors $\mathbf{b}_n$, and $\text{mish}(x) = x\tanh(\ln(1+e^x))$ is a nonlinear *activation function* [180] that is applied element-wise. The output vector, $\mathbf{y}$, contains each cross section of interest:

$$\mathbf{y} = \begin{bmatrix} \sigma_1(\varepsilon) \\ \sigma_2(\varepsilon) \\ \vdots \end{bmatrix}, \tag{2.3}$$

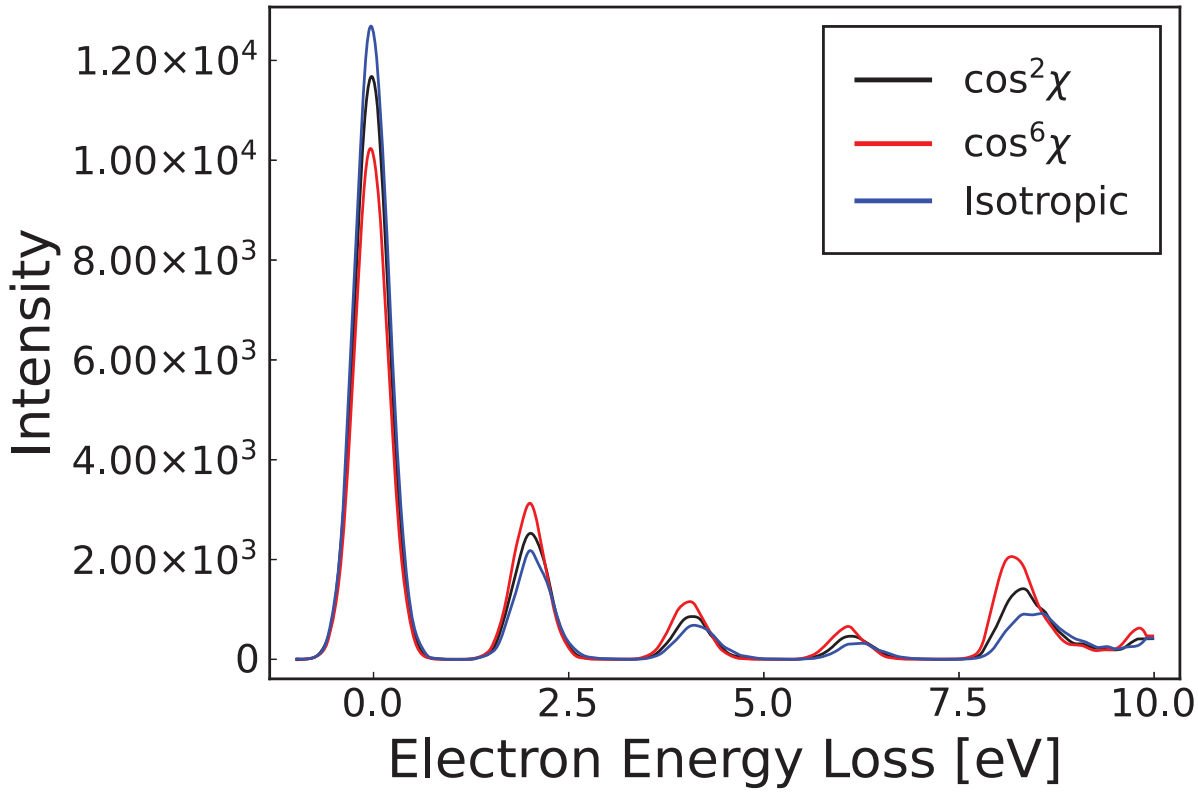

Figure 2.9: Elastic and inelastic EELS, with a varying differential cross section. An initial energy of 10 eV is used with an inelastic threshold of 2 eV. Each DCS is represented using a normalised power of $\cos(\chi)$, as indicated in the legend. For higher degrees of forward scattering, a decrease/increase was observed at lower/higher energy loss.

all of which are a function of energy, ε, which becomes an input to the neural network alongside the available EELS data:

$$\mathbf{x} = \begin{bmatrix} \varepsilon \\ \hline I_1 \\ I_2 \\ \vdots \end{bmatrix}, \tag{2.4}$$

where $I_1, I_2, \ldots$ are the electron intensities accumulated in each of the considered EELS energy bins. Note that we apply suitable logarithmic transformations to ensure that all inputs and outputs of the network are dimensionless and lie within $[-1,1]$. In what immediately follows, we specify that each bias vector contains 64 parameters, with the exception of $\mathbf{b}_4$, of which the size must match the number of cross sections in $\mathbf{y}$. The weight matrices are sized accordingly.

In order to train the neural network, Equation (2.2), we require an appropriate set of example solutions to the inverse EELS problem. To ensure cross sections provided by the network are physically plausible, we train on cross sections from the LXCat project [52, 72]. Specifically, we train with cross sections of the form [1]:

$$\sigma(\varepsilon) = \sigma_1^{1-r}\left(\varepsilon + \varepsilon_1 - \varepsilon_1^{1-r}\varepsilon_2^r\right)\sigma_2^r\left(\varepsilon + \varepsilon_2 - \varepsilon_1^{1-r}\varepsilon_2^r\right), \tag{2.5}$$

where $\sigma_1(\varepsilon)$ and $\sigma_2(\varepsilon)$ are a random pair of LXCat electron scattering cross sections, sampled from the available targets, of a given type (e.g., excitation, ionisation, etc.), r is a pseudo-random number uniformly distributed between 0 and 1, and ε_1 and ε_2 are their respective threshold energies. Once suitable cross sections are found for the training, corresponding LμJ EELS can be determined using our Monte Carlo simulation. In total, we consider 10,000 such training exemplars.

We implement and train the neural network, Equation (2.2), using the *Flux.jl* machine learning framework [181]. The network is initialised such that its biases are zero and its weights are uniform random numbers, as described by Glorot and Bengio [182]. Training is performed using the AdaBelief optimiser [183] with Nesterov momentum [184, 185], step size $\alpha = 10^{-3}$, exponential decay rates $\beta_1 = 0.9$ and $\beta_2 = 0.999$, and the small parameter $\varepsilon = 10^{-8}$. At each iteration, the optimiser is provided with a different batch of 4096 training examples, where each batch consists of 32 training cross sections each evaluated at 128 random energies of the form $\varepsilon = 10^s$, where $s \in [0,2]$ is sampled from a continuous uniform distribution. For each batch, the optimiser adjusts the neural network weights and biases with the aim of further minimising the mean absolute error in solving the inverse EELS problem for that batch. Training is continued for 250,000 iterations, providing an equal number of potential solutions to the inverse problem. We then select every 10 for the last 100,000 cross sections, and the quality of each of these solutions is subsequently assessed by simulating their corresponding EELS and comparing those to Ne's EELS to find the 'best' regression.

2.5.2 Cross section regression given the EELS

We now implement and train neural networks of the form of Equation (2.2), to determine a selection of Ne's cross sections given the corresponding EELS, while assuming full knowledge of Ne's remaining cross sections. In total, we use eleven EELS, corresponding to initial electron energies of 100, 79.43, 63.1, 50.12, 39.81, 31.62, 25.12, 19.95, 15.85, 12.59, and 10.0 eV. In each spectra, a combined energy resolution of 0.9 eV was assumed based on the detector performance that we currently find at Flinders University. Additionally, for computational considerations, each electron was simulated until 90 % of its energy was lost. For the initial energies considered, no electron was simulated below 1 eV, and thus we restrict the prediction domain to $[1\,\text{eV}, 100\,\text{eV}]$.

We first determine only Ne's elastic momentum transfer cross section (MTCS) from the considered EELS. Figure 2.10a shows a reasonable level of agreement between the elastic MTCS for Ne [179] and those found by the neural network, with the best regression seen to be accurate to within 9 %. Figure 2.10b shows that, despite the large range in cross sections for the 100 best regressions depicted in Figure 2.10a, the corresponding range of the EELS is much smaller, and in good agreement with those for Ne. This highlights the nonuniqueness of the inverse EELS problem, and suggests that there is not much room for improvement to the best cross section fit plotted in Figure 2.10a unless; additional EELS were included, the energy resolution of the spectra was improved, or additional information about the unknown cross sections was provided as input to the network.

We follow the above by now simultaneously determining both the elastic MTCS and ion-

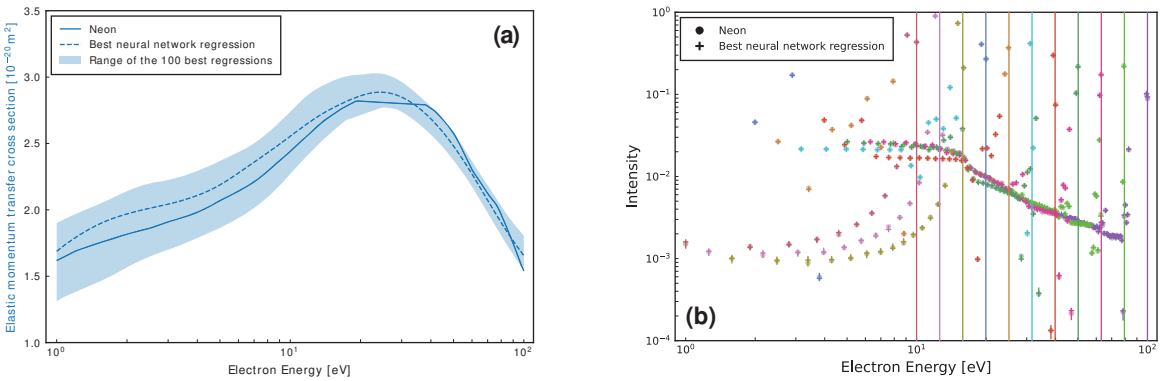

Figure 2.10: *Neural network* regression of Ne's elastic MTCS [179], (**a**), and the corresponding agreement, (**b**), between its simulated EELS and the EELS used to perform the fit. The vertical lines in (**b**) denote the initial energies for each of the eleven EELS considered (from 10 eV to 100 eV incident energy, inclusive). Additionally, a shaded area in (**a**), along with vertical error bars in (**b**), are provided to indicate the range of the 100 best regressions. See also the figure legend for further details, noting that black is used to represent each colour of that marker shape and where colours correspond to each initial electron energies of 100, 79.43, 63.1, 50.12, 39.81, 31.62, 25.12, 19.95, 15.85, 12.59, and 10.0 eV, indicated by vertical lines. In this model, a bias vector size of 64 was used, along with 250,000 iterations.

isation cross sections for Ne, using the same set of EELS. In this model, the bias vector was increased to 128, while 300,000 iterations were performed. As expected, the uncertainty in the elastic MTCS has increased here, with a larger elastic MTCS envelope found in Figure 2.11, with the best regression seen to be accurate to within 18 %. In contrast, the corresponding ionisation cross section envelope is particularly small, with the best regression being accurate here to within 1%. We attribute this high accuracy to the prominent ionisation "shoulder" present in six out of eleven of the EELS. Figure 2.11b shows that the corresponding EELS are now close in line with those for Ne, despite having a range that is slightly larger than their counterparts in Figure 2.10b.

Using the MC simulation, every combination of the best 100 elastic and ionisation cross section pairs was compared through their resulting EELS to find a further improved cross section set. While the maximum error in the elastic MTCS fit increased to 20%, the average error decreased resulting in a closer fit. For ionisation, the maximum error decreased to 0.2%, which further emphasises the remarkable predictive capability of this model for ionisation cross sections.

The extension of this methodology to include the prediction of excitation cross sections, or more specifically, the simultaneous prediction of three or more cross sections, results in a substantial decrease in accuracy within the current methodology. Thus, the simultaneous prediction of elastic, ionisation, and excitation cross sections is left for future iterations of this method, which should include advances in either the experimental resolution, or the fitting process.

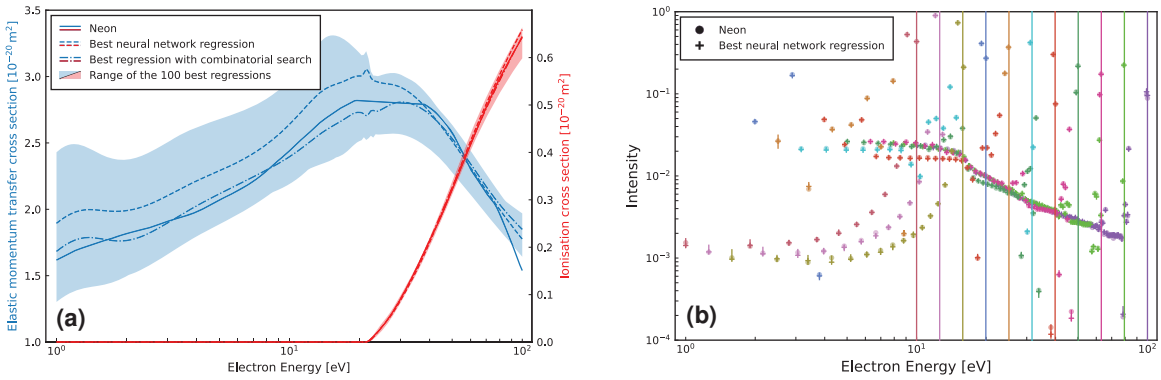

Figure 2.11: *Simultaneous neural* network regression of Ne's elastic MTCS and ionisation cross sections [179], (**a**), and the corresponding agreement, (**b**), between its simulated EELS and the EELS used to perform the fit. The vertical lines in (**b**) denote the initial energies for each of the eleven EELS considered (from 10 eV to 100 eV incident energy, inclusive). Additionally, a shaded area in (**a**), along with vertical error bars in (**b**), are provided to indicate the range of the 100 best regressions. See also the figure legends for further details, noting that black is used to represent each colour of that marker shape, where colours correspond to each initial electron energy of 100, 79.43, 63.1, 50.12, 39.81, 31.62, 25.12, 19.95, 15.85, 12.59, and 10.0 eV, indicated by vertical lines. In this model, a bias vector size of 128 was used along with 300,000 iterations.

2.6 Conclusion

We have developed a joint Monte Carlo and machine learning solution to the inverse Milne problem, that extracts electron cross sections based on electron energy loss spectra from a micro-jet of dense gas. Machine learning was conducted using similar techniques outlined in the literature [1, 47, 106, 107], while a new Monte Carlo simulation of a liquid micro-jet was developed. As a proof-of-concept, we found that the neural network determined neon's gas phase elastic momentum transfer cross sections to within 9%.

The extension towards the simultaneous determination of neon's ionisation cross sections, in addition to elastic scattering, decreased the accuracy to within 18% for elastic scattering, but was accurate within 1% for the ionisation cross section. A combinatorial search was conducted using the 100 best elastic and ionisation cross section pairs, which resulted in an accuracy to within 20% for the elastic MTCS and 0.2% for ionisation. While the maximum error for neon's elastic MTCS increased, overall, the fit was improved, with only the higher energy regime suffering in accuracy. The determination of three or more simultaneous cross sections resulted in a substantial decrease in accuracy, and is thus left for future iterations of this method.

As expected, absolute magnitudes were difficult to determine, although the prediction of the energy dependencies showed promise. Ionisation cross sections were remarkably well determined, while the elastic cross section prediction saw only quite slight discrepancies. Considering a relatively well-formed energy dependence, theoretical values at the higher energies could be used to 'fix' each cross section to improve the current prediction. Alternatively (or in addition), the relative flow technique used for gas phase scattering experiments to achieve absolute cross sections could be adapted to these liquid micro-jet experiments.

The main limitation with our current technique revolves around information density. Spectra are comprised of several 'dead zones', in which little to no scattering information exists. Additionally, a coarse energy resolution was shown to hide important information within the spectra, especially around inelastic peaks with similar threshold energies. To increase information density, a feature extraction algorithm might be utilised for each spectrum along with an improved experimental detector resolution. In other spectral studies, Gaussian de-convolution algorithms are employed to extract peaks from spectra. Utilising a similar approach, along with an increased detector resolution, one could provide further clarity to the network, assuming an appropriate treatment of asymmetry resulting from both multiple scattering and the ionisation energy sharing profiles.

Currently, a fitting algorithm is in development which, when applied to the method outlined in this study, aims to improve the predictive capability of the neural network. Additionally, the inclusion of appropriate liquid structure factors, surface potentials and space charge effects are necessary for real-world derivations of effective electron–liquid cross sections. Overall, through a proof-of-concept model, we have shown that utilising machine learning, along with a

significant wealth of Monte Carlo training data, one can reasonably predict individual and two simultaneous electron scattering cross sections from EELS. The extension towards predicting full, self-consistent cross section sets first begins with improvements on the methodology to ensure an improved accuracy in determining the cross section magnitude.

Chapter 3

The calibration and implementation of an electron-liquid micro-jet experiment

In this chapter, we utilise the results of the work presented in Chapter 2 to construct and conduct initial measurements of electron scattering from the liquid micro-jet set up at Flinders University. The work conducted was primarily undertaken during a 3 months stay at Flinders University supported by James Cook University and Flinders University.

The primary goal of this work was to measure the first energy loss spectra of electron scattering from the liquid micro-jet. To achieve this, it was crucial to develop an operation procedure that would ensure a clean vacuum and stable liquid could be achieved.

This chapter includes experimental design work that was conducted with the aid of by J. R. Gascooke and D. B. Jones. All other work described in this chapter is my own.

3.1 Introduction

In Chapter 2, a Monte Carlo simulation was used to investigate the sensitivity of energy loss spectra, measured from a liquid micro-jet (LμJ) scattering experiment, to changes in the electron-scattering cross section set. Deep learning was then used to determine the feasibility of using this data to determine electron-scattering cross sections. In this chapter, we describe the implementation of such a LμJ experiment in which electron-liquid scattering is directly investigated in a beam-like apparatus.

First, in Section 3.2, we detail each apparatus and procedure used for the LμJ electron scattering chamber. The scattering chamber is modified from the chamber described by Builth-Williams *et al.* [186] to accommodate the LμJ and thus only a summary of the unmodified components are provided here. In addition, the Monte Carlo simulation is again used to aid in evaluating and developing the procedures and measurements made in this experiment. In

Section 3.3, we describe modifications made to the Monte Carlo simulation informed by the equipment used. Finally, in Section 3.4, we conduct initial measurements and compare them to simulated measurements and discuss their ramifications for future investigations.

3.2 Experiment set-up

The scattering chamber described was built originally by Cavanagh and Lohmann [187] for coincidence detection of electron ionisation events from a gas beam. In this section, we describe the scattering chamber and detail the modifications made to suit the new LμJ apparatus.

3.2.1 Chamber

A schematic of the vacuum chamber is shown in Figure 3.1. It consists of a cylindrical lid and baseplate fabricated from 310-stainless steel due to its non-magnetic properties. In addition, an inner layer of 3 mm thick μ-metal exists inside the chamber to significantly reduce any external magnetic fields. Twelve 2.75 inch Conflat flanges are located on the baseplate and act as ports for electrical and rotatable mechanical feed-throughs. Two 3.75 inch viewing ports are positioned on the chamber; one of which directly opposite the electron gun while the other is displaced 90° to view the interaction region at the centre of the chamber.

The chamber measures 600 mm vertically with an outer diameter of 614 mm. A 6 inch Conflat port extends 95 mm from the top of the chamber and the two viewing ports extend 95 mm from the side. The base plate has a diameter of 704 mm and is 35 mm thick.

A 300, mm 310-stainless steel cylindrical cold trap extends down from the 6 inch Conflat located on top of the chamber. The cold trap is filled with liquid nitrogen during operation to aid in maintaining the vacuum by providing a surface for molecules such as H_2O to condense. In addition, the chamber is warmed via heating tape to improve degassing speed and reduce condensation on the inner surface of the chamber.

Nine of the 2.75 inch twelve Conflat flanges are dedicated to electronic and mechanical feedthroughs for the two analyses. One houses a ‘T’ splitter piece that houses both the electronic controller and liquid inlet line for the LμJ. Another is also split into two through a ‘T’ piece with a pirani gauge and an Edwads Penning 8 cold-cathode gauge. The final flange contains a vacuum release valve for pressurizing the chamber.

The evacuation of the chamber is achieved in two stages through a Pfieffer TMH 520 turbomolecular pump along with a Pfieffer Du0 25 M rotary pump connected to the backing line. Typically, the operation of the LμJ within the chamber results in pressures within the low 10^{-5} Torr region. While the base pressure for the chamber is stated as 2×10^{-8} Torr in [186], a minimum pressure of 10^{-7} Torr was found in this work once the LμJ was installed.

Outside the chamber there exists three sets of orthogonal 2.2 m Helmholtz coil pairs to nullify external magnetic fields. We note that the measurements presented here represent initial trials that were conducted without the Helmholtz coils. After their calibration the electron gun and detectors malfunctioned and no further measurements were made.

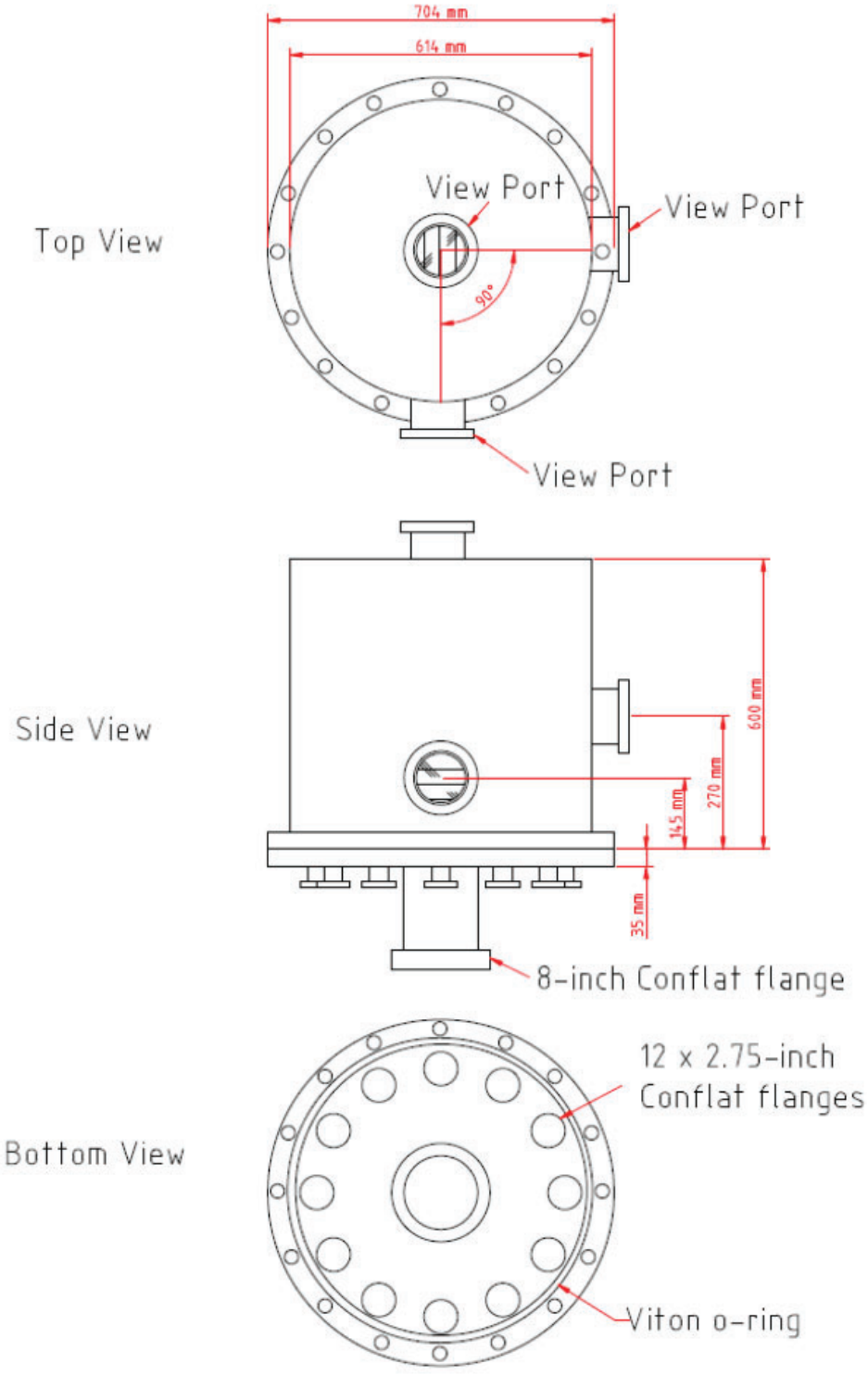

Figure 3.1: The Flinders University $(e,2e)$ spectrometer chamber schematic. Image Source: [186].

3.2.2 Electron gun

The electron gun has been previously described in detail [186] and a brief overview is given in what follows along with a schematic representation in Figure 3.2. The gun consists of a series of electrostatic lense elements $(V_1 - V_5)$, a source cathode (C_1), collimation apertures (A_1, A_2) and a single set of deflectors (D_1) that can steer the electron beam. The source cathode consists of a hairpin filament tungsten filament and during operation a thermionic electron beam is typically produced with a current of $\sim 2.2\,\mathrm{A}$ through the filament.

Following the tungsten filament, a pierce element (P_1) consisting of a 1 mm diameter aperture centred around the source filament exists as an initial focusing element for the electron beam. The application of a negative potential across the pierce element reduces the angular spread of electrons which exit through its aperture. Additionally, there exists two beam defining apertures A_1 and A_2 which each contain a 1 mm diameter in their centre to selectively remove electrons following an aberrant path.

Along the electron gun, voltages are applied across 5 separate 310-stainless steel cylindrical lens elements. These potentials, much like optical lenses, serve to focus the electron beam such that it follows a largely parallel path as it exits the electron gun. A typical path for the electrons using standard values of each potential is shown in Figure 3.2. This path was calculated in [186] using the SIMION charged-particle optics code [188]. Finally, there exists a deflector array D_1, located within V_5, which allows some control over the horizontal and vertical position of the beam in the interaction region.

3.2.3 Electron detectors

Shown in Figure 3.3, the analysers contain a focusing array, two hemispheres and an electron multiplier. The focusing array operates in much the same way as the electron gun with a series of electrostatic lenses, apertures and a set of deflectors that select and transport electrons leaving the interaction region into a hemispherical electron analyser. Each hemisphere of the analyser is made from ultra-high vacuum compatible aluminium, the surface between each hemisphere that interacts with the electrons is coated in a 1 µm layer of gold to minimise surface charging.

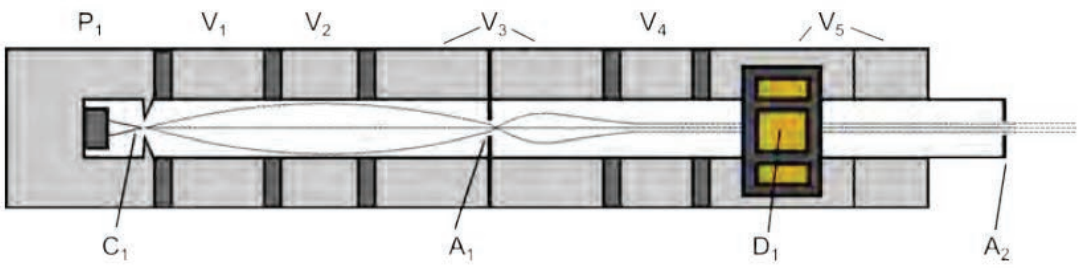

Figure 3.2: Schematic diagram of the electron gun used in the present measurements. Image is reproduced from [186].

As described by Builth-Williams *et al.* [186], the two hemispheres select for electrons electrons that pass through the analyser with an energy of $E_p = eV_p$. The inner (V_i) and outer (V_o) hemisphere potentials are given by,

$$V_i = V_p \left(\frac{r_p}{r_i} - 1 \right), \tag{3.1}$$

and

$$V_o = V_p \left(\frac{r_p}{r_o} - 1 \right), \tag{3.2}$$

respectively, where $r_i = 50\,\text{mm}$ and $r_o = 75\,\text{mm}$ are their corresponding radii and r_p is the mean of the two. r_p also corresponds to the path followed by an electron with energy E_p, which is shown as a red dashed line in Figure 3.3. Electrons leaving the interaction regions with the correct energy pass through the analyser and are detected using a channel electron multiplier.

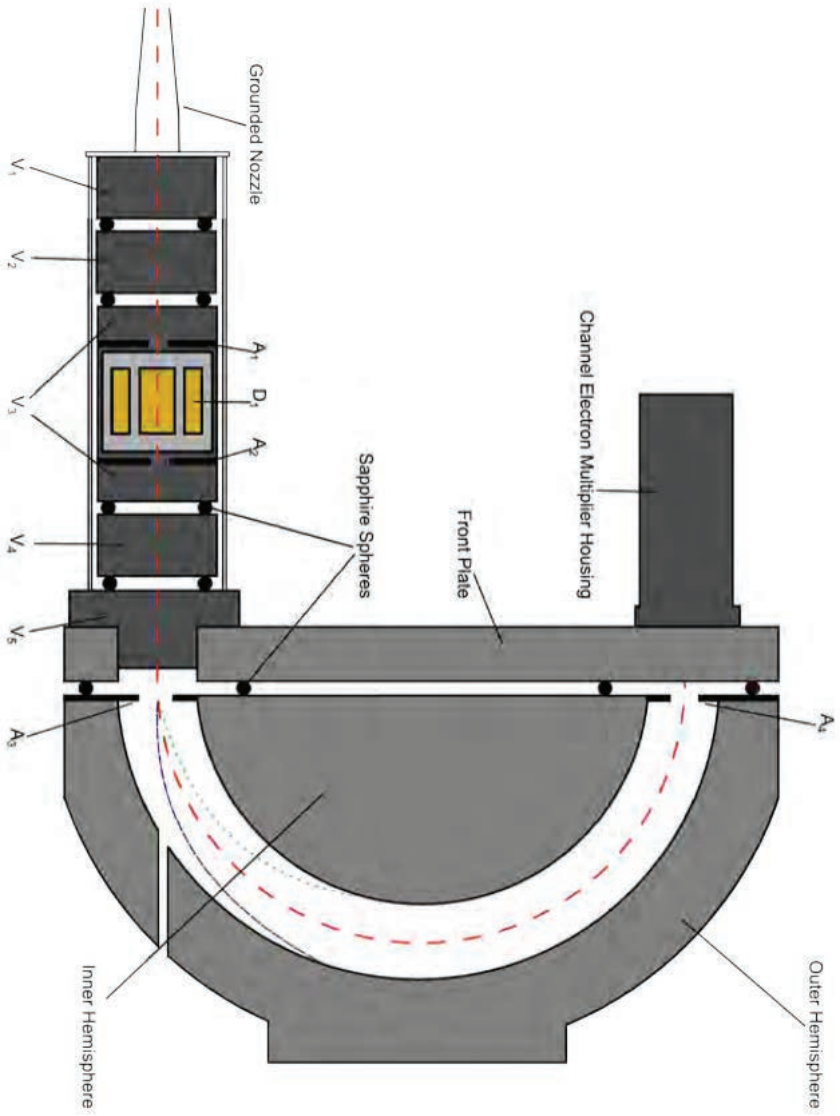

Figure 3.3: Schematic diagram of the electron analyser. The red line traces out the path that electrons of $E_p = eV_p$ take, the green and blue lines trace out paths of electrons with less and more energy respectively. Image is reproduced from [186].

The original experimental setup consisted of two analysers, one for the scattered (primary) electron and one for the ejected (secondary) electron. In this experiment, we seek to measure the energy loss spectra of electron scattering from a LμJ and thus only the scattering analyser is used. Due to the physical size of the LμJ housing and the existence of the ejected analyser, we are restricted to the angular range of -20° to 60°. The removal of the ejected analyser would extend this range to 120° to allow for the measurement of the backscattering signal.

3.2.4 Liquid micro-jet

In this work, a LμJ replaces the original molecular beam source described in [186]. The micro-jet was developed by Advanced Microfluidic Systems GmbH [108]. An $1/16$ inch inlet capillary is passed through a Conflat flange into the chamber where it is attached to a crystal nozzle that produces the LμJ. The inner diameter of the nozzle is tapered to produce a liquid beam of a desired size. Liquid samples are prepared in a glass bottle and are degassed through a sonic bath for 480 s. Before use, a few grains of salt are added to reduce electrokinetic charging of the jet during operation [189]. A high pressure dosing pump (Knauer 40P) is then used to draw liquid from the bottle and through the inlet capillary at $0.5 - 1.5\,\mathrm{ml/min}$.

Figure 3.4 shows the LμJ with the electron gun and the two hemispherical detectors positioned radially around the scattering region. In this experiment, nozzles with diameters of 15, 25 and 40 μm were available and 40 μm was used in this work for its stability. From the nozzle, liquid flows directly downward through the vacuum and into a 1 mm orifice in the centre of the catcher. From there, the liquid drains with gravity and the help of a diaphragm pump (Vacuubrand MD 4C NT) where it pools in a vacuum safe bottle submerged in an ice bath awaiting disposal. Both the nozzle and catcher are heated to reduce the risk of the sample freezing. The position of the jet can be externally controlled through two stepping piezo motors along the x-y axis of the scattering plane. Additionally, the height of the jet can be adjusted manually.

From the catcher, a waste tube removes the expended sample from the chamber through a Conflat flange and into a vacuum safe glass catcher bottle. An additional tube extends from the bottle lid and is attached to a backing pump to prevent backflow into the chamber. Both of these tubes contain valves to allow emptying of the bottle during operation.

3.2.5 LμJ operation

In what follows we outline the procedure followed in this work to prepare the scattering chamber and the various instruments. First, we prepare the LμJ by thoroughly cleaning both the housing and the nozzle before installing and performing a pressure test. With the LμJ running, we then seal and evacuate the chamber until the pressure stabilises. Liquid nitrogen is then added to the

cold trap to further improve the vacuum. Finally, the electron gun and detectors and prepared for measurements.

Preparation

Throughout the experiments the equipment used within the vacuum chamber required regular cleaning before use to prevent clogging of the capillaries and to ensure a good vacuum could be achieved. During preparation before each experiment, we conducted a cleaning process to mitigate these issues. In what follows we outline this process.

To supply the jet, a 1 L sample of de-mineralised water was prepared in a clean glass bottle. The bottle was then partially submerged in a sonic bath for ≈ 480 s to degas the sample. Then, with the cap nut of the LμJ housing removed, the inlet capillary was purged with the dosing pump

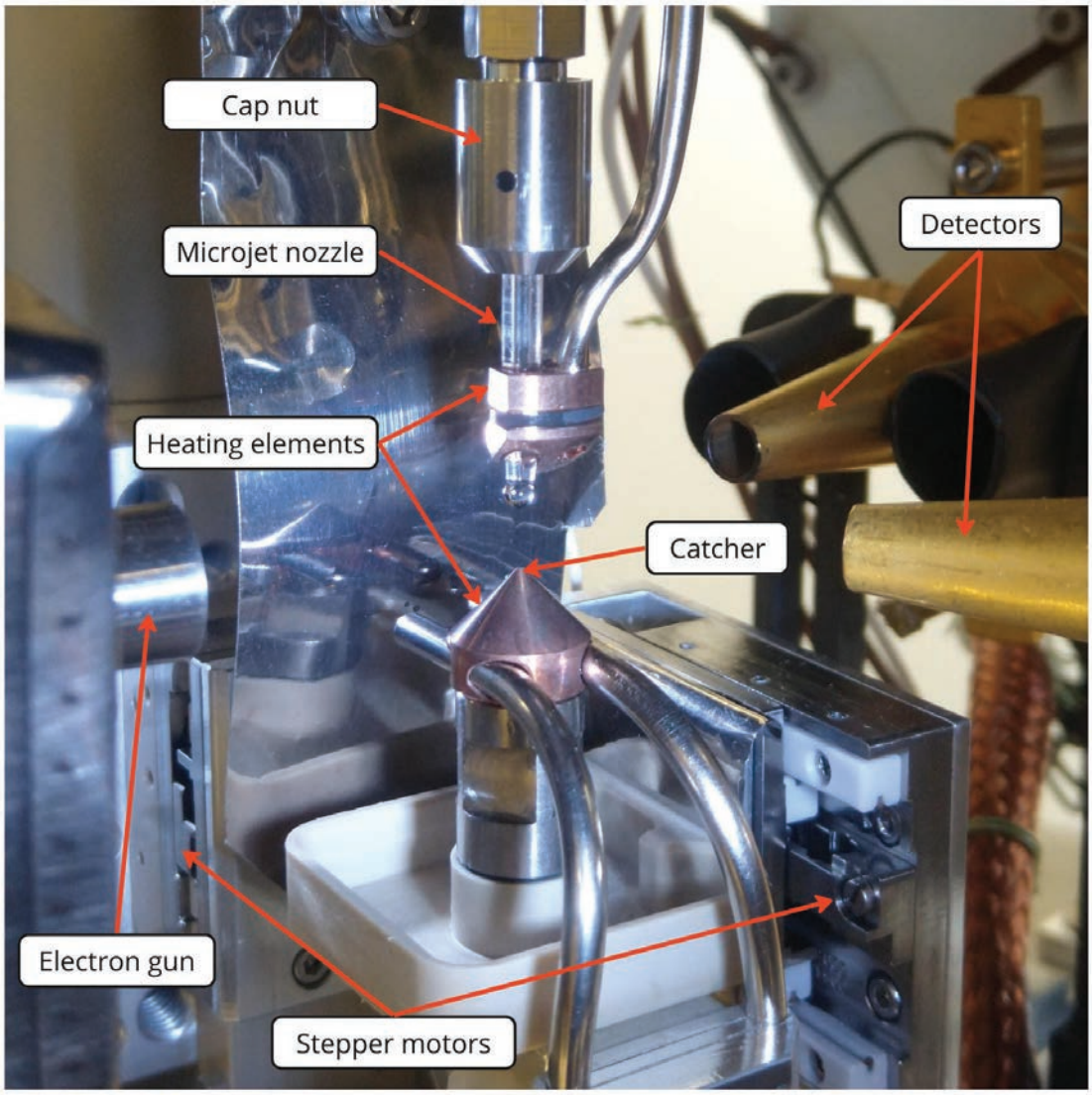

Figure 3.4: Photograph of the present liquid micro-jet apparatus along with various labels indicating each feature.

set to a flow rate of 6 ml per minute for 3 minutes to remove any build up within the capillary. The housing was then wiped with a low-lint cloth to remove any remaining debris and liquid.

To clean the LμJ nozzle, a filtered syringe placed over the tapered end of the nozzle was used to force isopropyl alcohol through and out of the nozzle. The remaining alcohol was then removed from the nozzle with an additional filtered syringe of air before repeating the process 6 times. Ensuring the entrance of the nozzle does not touch any surface once cleaned, the nozzle was then inserted into the housing and the cap nut tightened to finger tight. To ensure a proper fit was obtained once inserted, a pressure test was conducted with with a flow rate of $2\,\mathrm{ml/min}$. A small glass flask was placed under the nozzle to catch the liquid waste and the nozzle if it should fail the pressure test. If the jet moved inside the housing, the flow was stopped and the nozzle repositioned with more force applied when tightening the cap nut.

Once the nozzle was secured, we aligned the nozzle and catcher by eye using the piezo stepper motors. Then, a flow rate between 0.5 and $1.5\,\mathrm{ml/min}$ was used to check the alignment and adjust where needed. A final fine calibration was then conducted where the catcher is moved such that the jet touches each axis boundary before returning to the 'true' center calculated from the number of piezo steps between each boundary. With the jet calibrated, the catcher bottle was the placed within a bucket of ice to ensure waste liquid condenses within the bottle. The catcher backing pump was then engaged to generate negative pressure within the catcher to prevent backflow into the chamber.

With the jet and catcher backing pump running and their heater elements turned on, any remaining liquid was removed from the chamber with a lint free cloth and the chamber seal was cleaned with a isopropyl alcohol wipe. As a precautionary step, a multi-layered sheet of aluminium foil was placed above the LμJ housing to shield the inlet capillary from the cold trap.

Operation

With the lid lowered onto the chamber seal, the chamber was then evacuated with the chamber backing pump until the pressure stabilises around $\approx 1 \times 10^{-2}\,\mathrm{Torr}$. The vacuum pump is then engaged to reduce the pressure until it stabilises around $\approx 5 \times 10^{-5}\,\mathrm{Torr}$. Through the evacuation process, the jet was closely monitored to ensure it remains stable. Finally, liquid nitrogen was added into the cold trap to improve and help maintain the vacuum by freezing evaporated water from the jet and any organic molecules that impact its surface.

Occasionally, solid matter or air bubbles would interrupt or block the flow of liquid through the nozzle. Interruptions in the flow would invariably result in the formation of ice around the nozzle or catcher. If the flow of the jet was impeded while the chamber was under vacuum, ice would often form around either the nozzle or the catcher due to the interrupted or miss-aligned flow of the jet. This formation would result in a large pressure spike as the liquid vapourised. Once the heating elements of the jet and catcher melted the formed ice, the jet was able to restore

operation on occasion. In the majority of cases however, new ice would form in its place resulting in additional pressure spikes. As sharp pressure spikes could be damaging to the vacuum pump and electron detectors, the waste line was constantly monitored for flowing water drops and the jet was monitored directly through the viewing ports. Once flow was interrupted, the shutdown procedure detailed in the next section was followed to protect the equipment and allow for a swift reset of the scattering chamber.

Once the jet and chamber were stable, the electron gun and detectors were turned on gradually to avoid burnout of their respective components. Shown in Figure 3.5 are the control racks for each component. Ensuring first that the voltage and amp dials of the filament supply are set to 0, the electron gun power supplies were turned on. Typical voltage values used were $P_1 = 0.12\,\mathrm{V}$, $V_1 = 398.6\,\mathrm{V}$, $V_2 = 77.0\,\mathrm{V}$, $V_3 = 360.8\,\mathrm{V}$ and $V_4 = 67.5\,\mathrm{V}$. Once the high voltage light turned on, the filiment supply was turned on. Following this, the detector voltage controller and detector CEM were turned on, again, ensuring the voltage dial on the CEM is set to 0. Then, at 10 minute intervals, both the filament supply amp dial and detector CEM voltage dial were increased by $0.2\,\mathrm{A}$ and $0.2\,\mathrm{kV}$ respectively until values of $2.2\,\mathrm{A}$ and $2.2\,\mathrm{kV}$ were reached.

Depending on how long the jet remained in operation, the catcher bottle would need to be emptied and replaced. In the experiments that were conducted here, the $1\,\mathrm{L}$ of sample prepared was more than sufficient for the duration of each experiment. The longest the jet was run continuously was approximately 4 hours in this work. To achieve this, the valves attached to both the backing pump tube and the catcher tube were shut. The bottle was then quickly removed, emptied and re-attached before opening the backing pump valve to return the bottle to an appropriate pressure. Once stable, the catcher valve was opened and the jet checked to ensure flow was maintained.

With the chamber stable and ready to conduct measurements, the software provided in LabVIEW was utilised to control the electron gun and detector and collect measurements as a function of scattering angle, incident energy and scattered energy.

Pressurisation

To shutdown and pressurise the scattering chamber, both the electron gun and detector voltage and amp dials were returned to 0 and their respective supply instruments switched off. It was essential that these instruments were turned off first to prevent damage to their parts during pressurisation. If the LμJ flow was interrupted prior or during the shutdown procedure, the inlet dosing pump was switched off first. Following this, the vacuum pump was switched off and allowed to spin down completely before turning the backing pump off. Finally, the evacuation valve on the chamber was slowly opened, ensuring that the pressure was slowly returned to the chamber.

With the chamber pressurised, any ice that formed on the outside of the cold trap would

begin to melt. The chamber lid was lifted and an aluminium 'bucket' was placed under the cold trap to shield the equipment from the dripping water as the ice melts. If the jet remained flowing, the inlet pump and catcher pump were turned off.

3.3 Simulation set-up

To inform our understanding of the experiment, we utilise a Monte Carlo simulation to replicate the experimental conditions observed. In what follows, we detail how each component of the experiment is reproduced in the simulation.

A 15 µm diameter cylindrical jet of dense gas with a constant radius is positioned such that the radius is in the *x*-*y* plane. The simulations conducted here were conducted with the

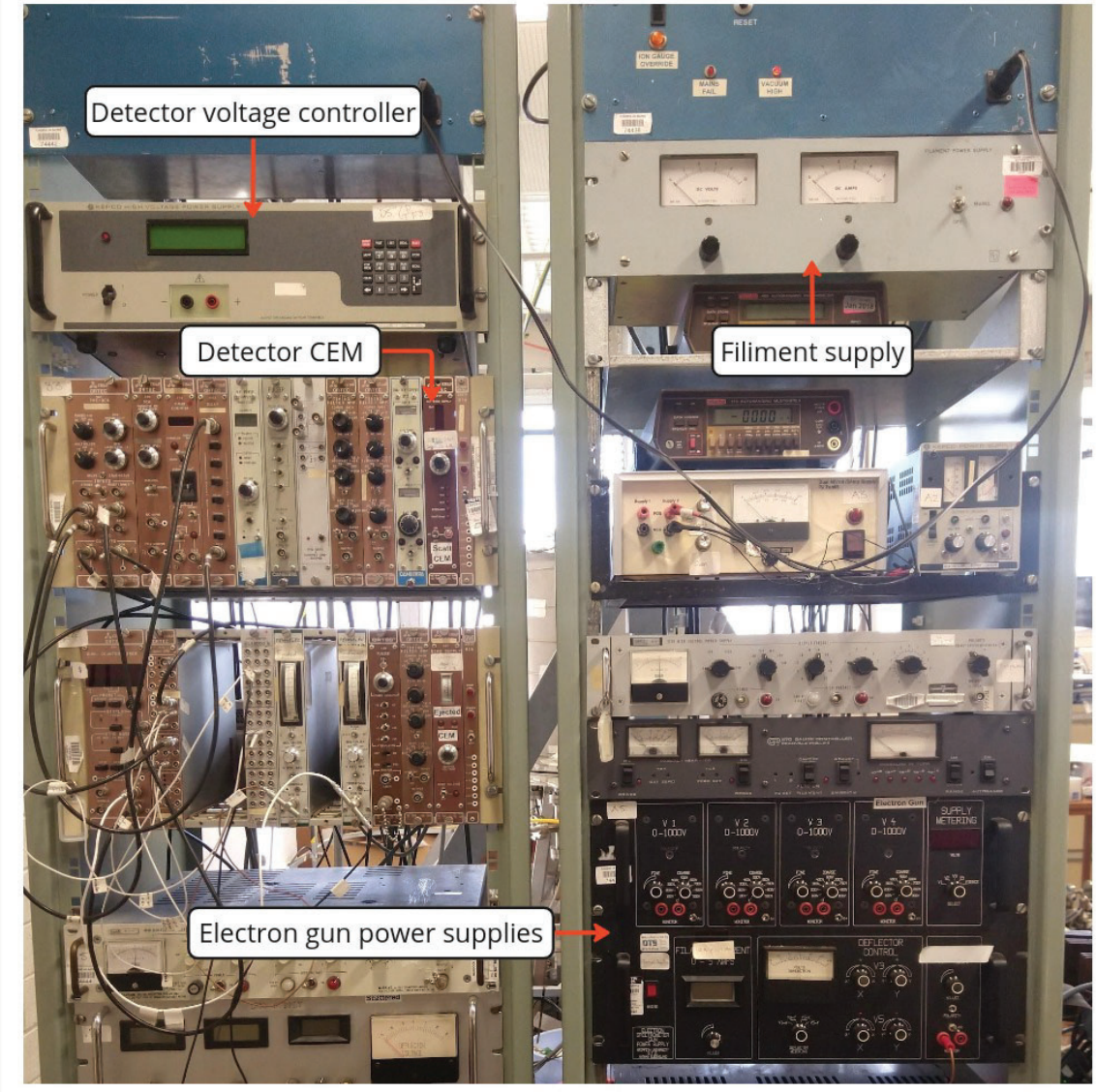

Figure 3.5: Labelled diagram of the electron gun and detector control racks.

assumption that a 15 µm nozzle would be used in the experiment. While it has been shown elsewhere that there exists a tapering of the jet width along its length [190], here we assume a constant cylindrical radius. The center of the jet is set as $(0,0)$. At each collision during the simulation, the velocity of each molecules is sampled from a Maxwellian distribution with a constant velocity shift of $100\,\mathrm{ms}^{-1}$ along the direction of the LµJ.

The jet itself is represented as radial boundaries that are used to calculate the time of flight for each particle to reach each boundary. Between each boundary, a neutral density is defined that governs each particles mean free path in that region. Each molecule is assumed to be confined within the 15 µm boundary of the jet. Outside of the jet, a low density vapour of the same molecule exists with a number density of $2\times10^{18}\,\mathrm{m}^{-3}$. In reality, the transition between the two regimes will exhibit some gradient but for simplicity in this simulation the change is assumed to be a step function as little variation in the results when compared to an inter-facial region similar to the one outlined by Garland *et al.* [191].

The electron gun is positioned at -2 cm on the x-axis relative to the centre of the jet. Electrons are initialised with a positive velocity in the x direction towards the jet with a Gaussian spatial distribution with a 1 mm FWHM in the y-axis and an energy distribution with a FWHM of 1.4 eV.

The detector is able to traverse in a circle around the centre position with a radius of 2 cm and an angular acceptance of $\pm1^\circ$. In the simulation, a radial boundary exists at 2 cm and each electron simulation is stopped once they reach this radius. The electron is then considered detected at a certain angle in the x-y components of its velocity vector lies within 1° of its spatial angle. In this fashion, as with the experiment, electrons are only detected if they originate from the scattering region of the LµJ itself. In addition, electrons that arrive at the detection radius with more than 5 mm displacement along the z-axis are not detected to approximate the 3 dimensional nature of the detector cone. To simulate the uncertainty inherent to the detector, when an electron is detected, its measurement is added to each energy and angle 'bin' within the stated uncertainty. In what follows, we use acceptance vales of ±1 eV and $\pm2^\circ$ for detection energy and angle respectively.

For this work, we use the electron cross section for H_2O vapour presented by Ness *et al.* [133] which are shown in Figure 3.6.

3.4 Results

In this section, we present the first results obtained of electron scattering from the liquid micro-jet along. In addition, we conduct Monte Carlo simulations of the LµJ and investigate their dependence on various cross section parameters. We begin with comparing the detected electron signal intensity as a function of LµJ position within the chamber for both the simulation and

experiment. We then compare this data with a simulated equivalent gas micro-jet and investigate the dependence on scattering angle and detection energy. In addition, we compare the simulated and experimental electron energy loss spectra for both a liquid jet and the background gas by moving the jet outside of the electron beam. Finally, we conduct a series of simulations to investigate the dependence of the energy loss spectra on both the differential cross section and density.

3.4.1 Alignment of the liquid micro-jet

Achieving an accurate alignment of the LμJ with respect to the electron gun and the detectors is a crucial step in the setup procedure of the experiment. In Figure 3.7 we show the simulated dependence of the detected electron signal on LμJ position, scattering angle and detection energy. For each Cartesian co-ordinate selected, a simulation is conducted and both energy and angle are stored for each detected electron.

It is clear that back-scattering angles results in a significantly stronger electron scattering signal when compared to forward-scattering angles. In addition, while a larger signal is observed when electrons with energies $> 5\,\text{eV}$ are included compared to the case when only the elastic signal is included ($> 95\,\text{eV}$), the dependence on LμJ position did not substantially differ in the two scenarios.

Shown in Figure 3.8, are elastic scattering intensity measurements taken from the LμJ

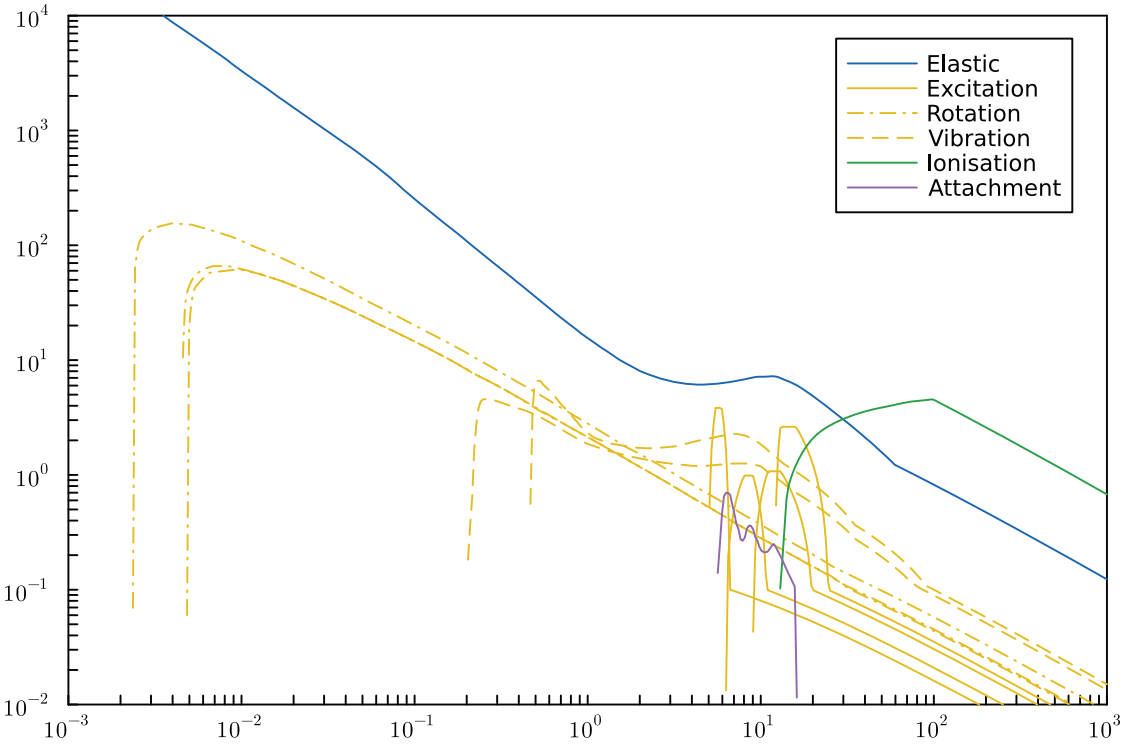

Figure 3.6: Electron scattering cross section sets for H_2O proposed by Ness *et al.* [133].

at a range of positions along the y-axis (perpendicular to the electron beam). Each step is approximately 1 µm with the initial position aligned by eye with the center of the electron beam. Two scans were conducted, one moving forward toward the housing, then another scan moving backward as the jet is returned to the center position. Interesting, these two scans resulted in substantially different counts of the electron signal. While the forward scan resulted in a distinct maxima near the 0 position, the backward scan exhibits only a small rise in signal as the LµJ

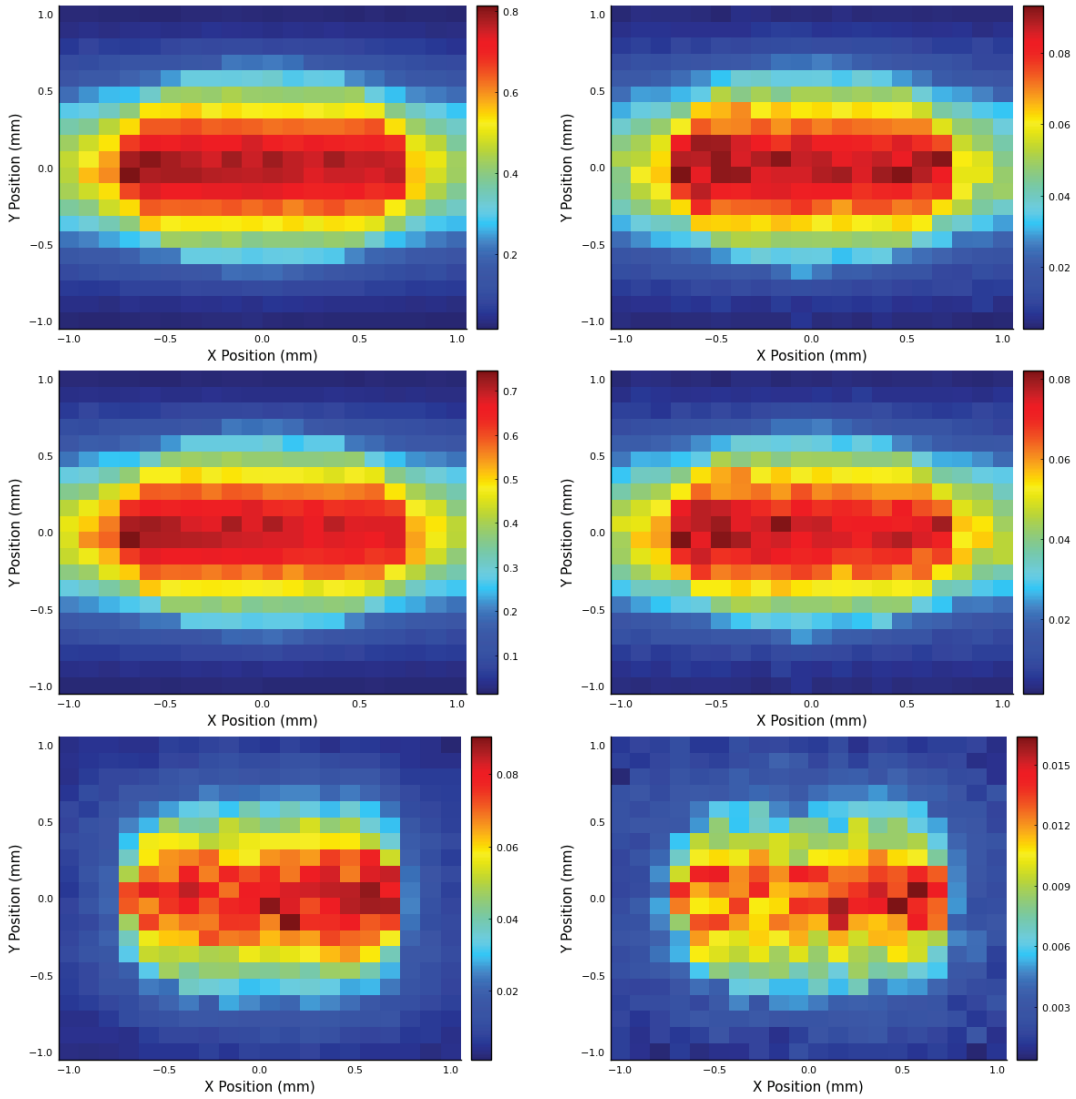

Figure 3.7: Detected electron signal for a 100 eV electron beam incident upon a 15 μm LµJ as a function of LµJ position. The electron beam is represented as a along the y-axis with a standard deviation of 1 mm and is directed along the positive x-axis. The LµJ is directed into the page. In each row, the detectors are limited to angle ranges; (top row) all angles, (middle row) back-scattering angles and (bottom row) forward-scattering angles. In the first column, all electrons above 5 eV are detected while in the second column only those with energies above 90 eV are detected to capture only elastic scattering. The heatmap scale is the percentage of the incident electrons that are detected. In each scenario, we find a similar profile for the total detected signal with a significant decrease in signal for forward-scattering angles compared to back-scattering angles.

returned to the center. Due to the physical limitations of the pipe connected to the catcher, the jet was unable to move beyond the positions shown in Figure 3.8.

Intervals of 20 'steps' of piezo motor was used with each measurement conducted over a period of 2 s. Several issues relating to miss-alignment of the jet were encountered while attempting these measurements. The drain tube connected to the catcher would exert a force on the catcher housing and result in a miss-alignment of the jet and the destruction of the vacuum. The observed discrepancies in the two scans could be due to density fluctuations as the LμJ moved, or due to electrokinetic charging of the jet over time. However, the exact reason is unclear at this time without more investigations.

3.4.2 Calibration of electron gun and detector

To calibrate the 0° position of the detectors relative to the electron beam, measurements of the electron elastic scattering signal were conducted for various angles. A distinct Gaussian shape is observed in Figure 3.9 with some asymmetry, which indicates a miss-aligned LμJ with respect to the electron beam. Angles between -5 and $-5°$ were omitted due to the risk of saturating the detectors from the unscattered electron beam.

The chamber is housed within 3 orthogonal Helmholtz coils to assist in negating Earth's magnetic fields. After calibration, east-west was set to 0.15 A, north-south was set to 1.2 A and the zenith was set to 3.0 A. Previously each coil was set to 0.3 A, 1.6 A and 2.3 A respectively.

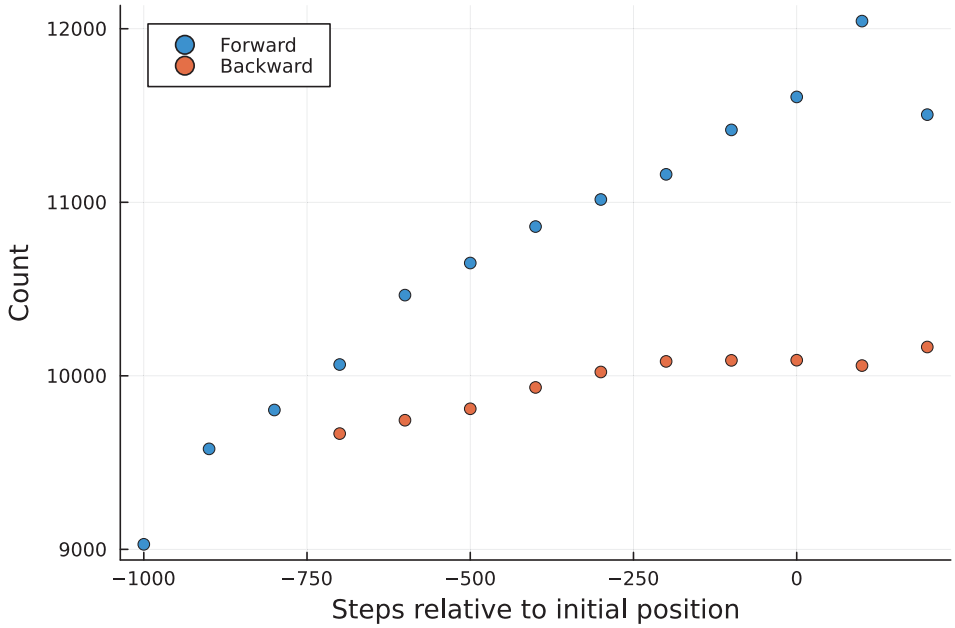

Figure 3.8: Perpendicular positional variation of the LμJ with respect to the electron beam direction. A 'step' refers to a command in the controller program which approximately moves the jet 1μm at a time. Note the difference in magnitude for forward/back. Electron gun current: 2.15 A, detector voltage: 2.2 kV, count time: 20 s, pressure: 5×10^{-5} Torr.

Figure 3.10 compares energy loss spectra with the previous coil parameters on versus without the coil to demonstrate its importance. An energy loss spectra comparing the newly calibrated coils was not possible due to time limitations and equipment failure. Due to the trial nature of the initial measurements presented in the following section, the Helmholtz coils were not used and so the electron beam is subject to Earth's magnetic fields.

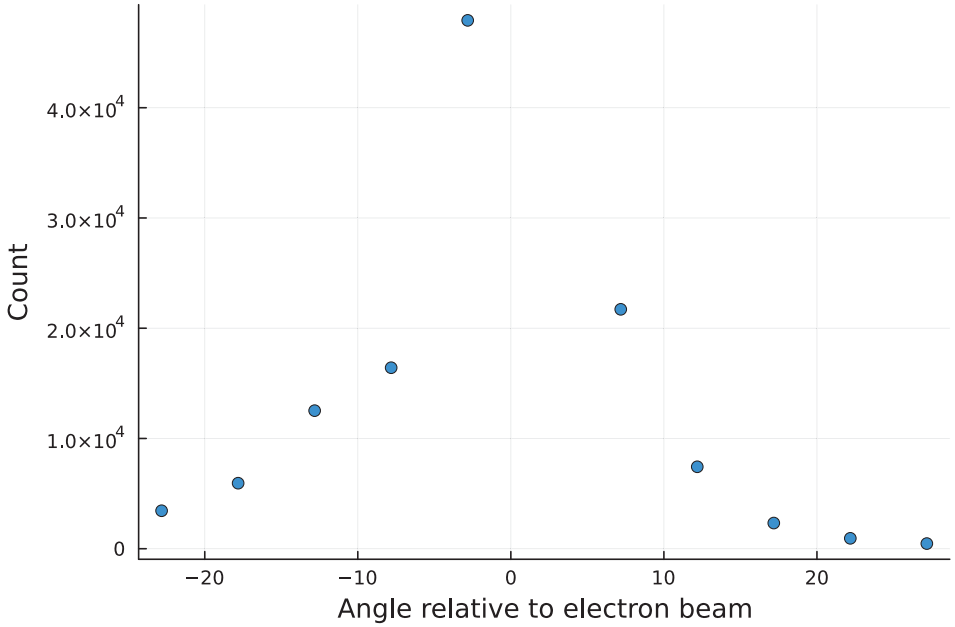

Figure 3.9: Detected electron counts for various scattering angles at elastic scattering energies. Some asymmetry is present which indicates an unaligned LμJ.

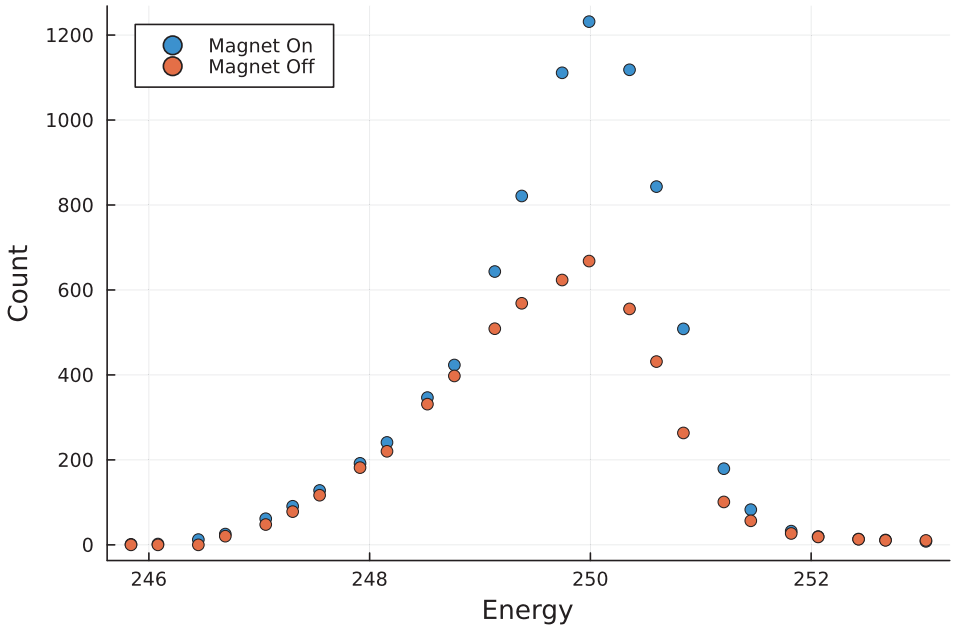

Figure 3.10: Influence of magnetic field for the previously calibrated Helmholtz coil currents. A spectra with the newly calibrated currents was not made due to time limitations and equipment failure.

3.5 Measurement of the electron energy loss spectra

Using an initial scattering beam of $\approx 250\,\text{eV}$, an energy loss spectra was measured from 251 eV to 220 eV. A strong elastic peak was found followed by a broad and tapering signal from inelastic and ionisation scattering processes. In Figure 3.11 we present the measured energy loss spectra for electrons scattered from the LμJ and compare that to spectra measured when the LμJ was moved to the side. For comparison, each liquid and gas pair of spectra were scaled by the maximum value of the liquid spectra in that pair.

Shown in Figure 3.11 are the simulated spectra for both the liquid and gas scenarios compared at select gas densities and analytic scattering angle distributions that represent the DCS. Each liquid spectra has been scaled by the maximum of the elastic peak that is centered around 250 eV. The maximum liquid value was then used to scale each corresponding gas spectra to compare their relative intensity. Generally, for the gas densities and DCS functions seleted, the simulation is able to reproduce the elastic peak observed. Clear from Figure 3.11, is a degeneracy between gas density and the DCS in these measurements. Comprehensive measurements of the angle dependence of the spectra could be utilised to determine the DCS in order to resolve the degeneracy in future investigations. In addition, the gas density could be determined by an appropriate ion gauge closer to the jet itself. An intensity profile of scattered electrons as the jet is moved across the electron beam also could be used in conjunction with simulated results to aid in reducing this degeneracy.

The most notable difference can be found between 230 and 247 eV where in the simulated spectra there exists two small inelastic peaks that are followed by the ionisation signal while in the measured data only a single, broad, peak is obvious. Without additional measurements to both validate the observed EELS and investigate the dependence upon initial energy and scattering angle, it is difficult to determine the cause for this discrepancy. The inclusion of explicit rotational processes may result in a similar broadening reflected in the smulated spectra. In addition, shifts in the energy loss threshold for excitation processes could result in each peak overlapping and merging into a single feature. We must emphasise here that these measurements are preliminary by nature and no conclusions about cross section set or measurement validity can be made from them.

Overall, these results emphasise the need for refined and extended measurements of the experiment presented here followed by an in-depth analysis of existing electron scattering cross sections for water.

3.6 Conclusion

Overall, a new electron-liquid scattering experiment using a liquid micro-jet in vacuum conditions has been established. The experiment features a crystal nozzle with a tapering channel that

produces liquid beams between 15 and 40 µm in diameter, depending on the nozzle used. The nozzle, in combination with its housing, is able to inject liquid into a vacuum scattering chamber where it quickly collected and removed by a catcher system.

The setup procedure for the experiment is outlined and results from initial calibration steps and measurements of electron energy loss spectra is presented. In addition, a Monte Carlo simulation is built that approximates the experimental conditions observed. The simulation is

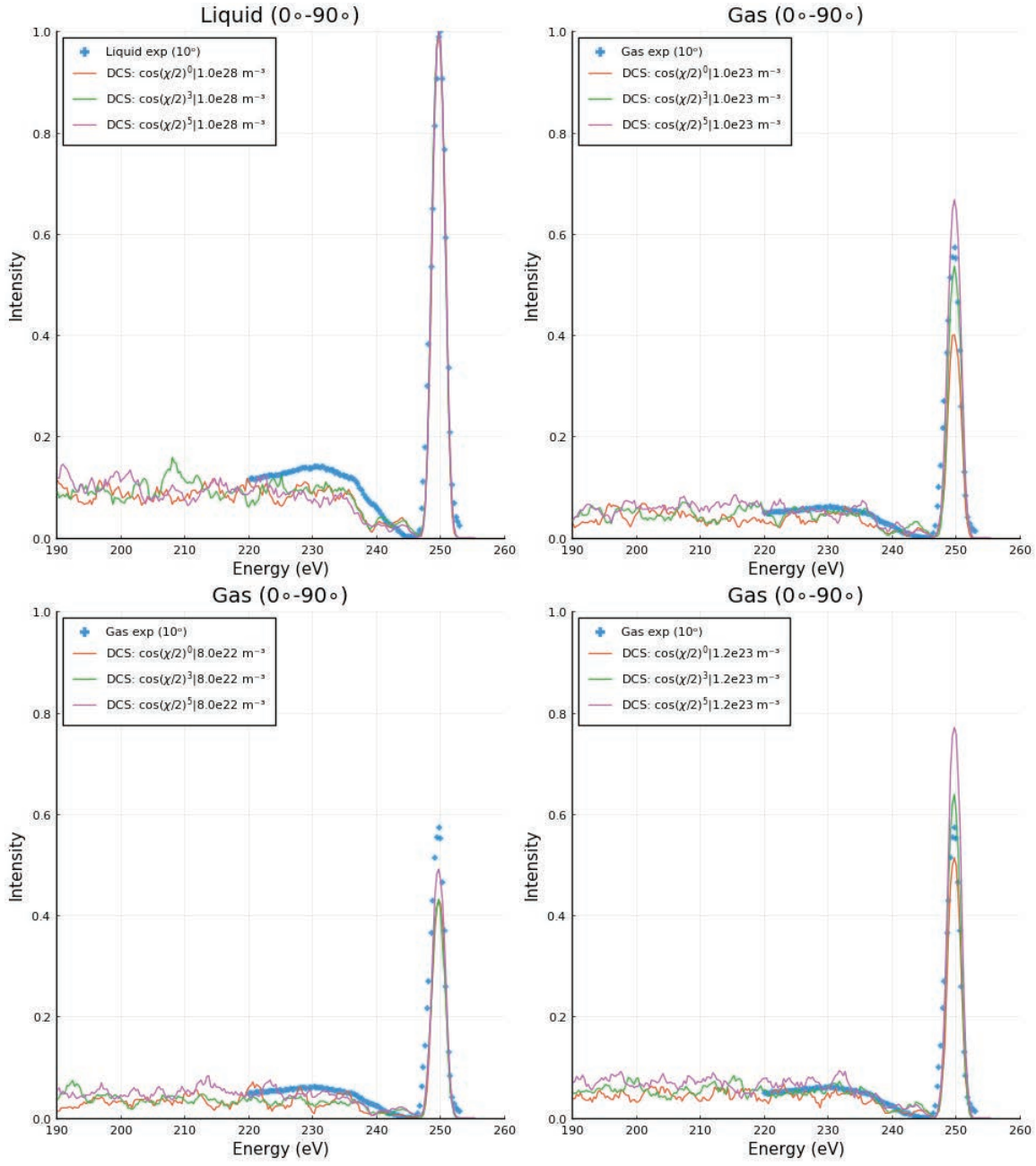

Figure 3.11: Electron energy loss spectra for a 250 eV electron beam incident upon a 40 μm LµJ compared to 'gas' phase measurements where the LµJ was moved to the side. In addition, various simulations were conducted using the H_2O cross section set of Ness *et al.* [133] for various gas phase densities and analytic differential cross sections (DCSs). Each pair of liquid and gas spectra were scaled by the maximum value of the liquid spectra.

used both for informing the design of the experiment and for comparison of existing theory to the initial results obtained.

First, we investigated the alignment of the LμJ by simulating the detected electron current as a function of jet position for various scenarios. We observed a significant increase in signal for back-scattering angles compared to the forward-scattering angles. Comparing these predictions to the experiment proved difficult due to the limited available movement and stability of the jet. However, we did observe a decreasing trend of the electron count rate as the jet was moved away from the electron gun.

We then conducted two electron energy loss spectra measurements to compare both liquid and gas scattering. A series of simulations were then produced to investigate the sensitivity of each measurement to both the background gas density and differential cross section. We found promising comparisons between simulation and experiment utilising the cross section set proposed by Ness *et al.* [133]. However, it was difficult to separate the effects of density variation from that of the differential cross section.

Due to time limitations, refined measurements were not conducted of the energy loss spectra presented here. Thus, the results of this investigation are preliminary by nature and only re-enforces the need for more measurements to be conducted of electron scattering from the LμJ.

Chapter 4

An iterative deep learning procedure for determining electron scattering cross sections from transport coefficients

This chapter includes the following publication:

[3] **D L Muccignat**, G J Boyle, N A Garland, P W Stokes and R D White, An iterative deep learning procedure for determining electron scattering cross-sections from transport coefficients, *Machine Learning: Science and Technology*, 5, 015047, 2024

As outlined in Chapter 1, this chapter, along with Chapter 5, is motivated by the need to determine complete and self-consistent electron scattering cross section sets for complex targets. This chapter outlines a new deep learning technique that was originally developed to determine a full cross section set for the molecule HFO1234ze(E), which is then detailed in Chapter 5. The method was developed to be general in nature and thus has many potential applications in the field of particle physics.

The foundation for the deep learning code used here was provided by P. W. Stokes. The code was adapted to include extrapolation of training data (see Appendix A.2), a branching network architecture (see Section 4.2.1) and an automated iterative method that uses deep learning to improve the predicted solution (see Section 4.2.2). To generate the training data for each network used, a multi-term Boltzmann solver written by P. W. Stokes was used and was only modified to include super-elastic collisions. All other work described in this chapter is my own.

4.1 Introduction

Electron transport models are crucial to enable the predictive control of low-temperature plasma systems [11]. Underpinning these techniques are the use of accurate and complete electron

scattering cross section sets. The derivation of scattering cross sections is typically conducted through experimental and theoretical techniques, coupled with verification through swarm scattering experiments to ensure their validity [44]. In regions where these techniques are limited, "educated guesses" and numerical techniques are often used to bridge the gap. This knowledge gap motivates the need for reliable and benchmarked numerical techniques to aid in the development of accurate and complete cross section sets.

Here, we focus on the determination of cross section sets from swarm data, otherwise known as the inverse swarm problem [1]. Presently, two primary numerical techniques exist that aim to solve the inverse swarm problem: the iterative swarm technique and, more recently, the application of Artificial Neural Networks (ANNs). The iterative swarm technique first used approximate distributions, such as a Maxwellian or Druyvesteyn distribution, of the electron energy distribution function to calculate transport coefficients that are compared to experimental transport coefficients and improved iteratively [99–101]. The accuracy of the iterative swarm technique was then improved with the inclusion of an accurate electron energy distribution functions derived from the solution of the Boltzmann equation [45, 102–104].

A substantial limitation to solutions of the inverse swarm problem lies in its ill-posed nature. In particular, the existence of multiple cross sections that describe similar scattering processes, such as similar threshold vibrational modes, results in substantial degeneracy of transport data for a given species [1, 98]. In this limit, the iterative swarm technique relies on the intuition and experience of an expert, which, along with the trial and error nature of the approach, results in an inefficient procedure that is difficult to reproduce. Several methods that attempt to automate this methodology have been proposed [192–198] to address this issue. Of interest to this study, is use of ANNs trained on existing cross section data to determine scattering cross sections for electron transport in gases.

In the early 1990s, Morgan *et al.* [46] first demonstrated a solution to the inverse swarm problem through an ANN trained on example cross sections and their associated transport coefficients. Recently, Stokes *et al.* [1] revisited this problem utilising advances in network architecture, model size and available cross section data to improve the network's predictive power. Since then, the method has been successfully applied to the improvement of tetrahydrofuran, α-tetrahydrofurfuryl and nitric oxide electron scattering cross sections [47, 106, 107]. Jetly *et al.* [105] evaluated the performance of three network architectures for the regression of single electron-scattering cross section and found that a DenseNet architecture resulted in the highest regression accuracy.

While the application of ANNs to the inverse swarm problem shows great promise, the method is constrained due to a number of key limitations. This study aims to address the following two limitations. First, we demonstrate that a conventional ANN limits the ability of the network to reliably and self-consistently model multiple independent cross section regressions

when compared to an equivalent network that is designed in a physics-informed manner to contain multiple parallel branches of densely connected layers. In this design, each possible scattering process that may occur for a given target is provided a separate branch, which assures the user that the total of all parallel branches reproduces the required total scattering cross section. Additionally, as the prediction of multiple cross sections is limited due to the degenerate nature of the inverse swarm problem, we propose an iterative procedure to enable the network to incrementally explore the solution space of the problem.

Reducing the impact of these limitations will extend the applications for the ANN method to complex bio-molecules critical for applications in fields such as plasma medicine [199] and dielectric insulators [54]. In previous work, Stokes *et al.* [1], used ANNs to approximate argon and helium's cross sections. However, argon and helium do not exhibit vibration and attachment collisions that are generally important in bio-molecules. Here, we use methane as a case study for the influence of vibration and attachment processes, as has been widely studied in the literature [200–204]. For example, the strong excitation processes demonstrated by methane lead to a breakdown of the two-term approximation that is often employed in the solution of Boltzmann's equations [204–206].

In Section 4.2, we outline each modification to the network architecture and methodology before evaluating their performance using methane as a case study. We then summarise the results in Section 4.3.

4.2 Artificial neural network regression of cross section sets

The application of ANNs towards determining complete cross section sets through the inversion of macroscopic experimental data has been the focus of a recent project at James Cook University [1, 2, 47, 106, 107,]. While the technique has predominately been used to improve existing cross section sets [47, 106, 107,], the determination of complete cross section sets for complex targets remains elusive due to the ill-posed nature of the problem. In this section, we present two modifications to the methodology that aim to improve the ability of the network to determine complete cross sections from transport data.

First, to aid the network in representing the independent nature of each cross section, we propose a Multi-Branch Artificial Neural Network (MBANN) and compare its performance through a regression of the cross section set for methane recommended by Biagi [179]. To reduce the impact of the non-unique nature of determining cross section sets with multiple similar scattering processes, we then propose an iterative procedure that incrementally explores the solution space by using perturbations of the previous regression. To demonstrate the iterative procedure, we compare the initial regression and the best regression found for methane's cross section set.

4.2.1 Multi-branch neural network regression

Stokes *et al.* [1] proposed an ANN where each element of the output corresponds to a single cross section. The simultaneous prediction of each cross section ensures that the full set of cross sections are self-consistent, which ensures an accurate replication of the target swarm transport data. In their investigation of various ANN architectures, Jetly *et al.* used separately trained networks to enforce independent feature maps for each cross section. The authors state that the simultaneous prediction of multiple cross sections would force the network to share feature maps across different types of cross sections and thus severely inhibit its predictive capability.

Here, we propose a Multi-Branch ANN (MBANN) to bridge the gap between the requirement for self-consistency and the desire for independent feature maps for each cross section. That is, for each cross section, there exists an independent block of dense layers that each extend from a single block of dense layers. Each parallel branch is then allowed to develop a feature set specific to a single cross section while still ensuring each regression is conducted in context of the full cross section set.

We utilise a MBANN of the form,

$$\sigma^{(\mathbf{x})} = \left[\mathbf{A}_5^{[n]} \circ \text{mish} \circ \mathbf{A}_4^{[n]} \circ \text{mish} \circ \mathbf{A}_3^{[n]} \circ \text{mish} \circ \mathbf{A}_2 \circ \text{mish} \circ \mathbf{A}_1\right](\mathbf{x}), \tag{4.1}$$

where $\mathbf{A}_i(\mathbf{x}) \equiv \mathbf{W}_i\mathbf{x} + \mathbf{b}_i$ are affine mappings defined by dense *weight* matrices $\mathbf{W}_i$ and *bias* vectors $\mathbf{b}_i$, and $\text{mish}(x) = x\tanh(\ln(1+e^x))$ is a nonlinear activation function [180] that is applied element-wise. The final output, $\sigma^{[n]}$, then represents the n^{th} cross section of interest within a set of N cross sections. $\mathbf{A}_3^{[n]}$, $\mathbf{A}_4^{[n]}$ and $\mathbf{A}_5^{[n]}$ form an array of N parallel branches that each utilise the output of $\mathbf{A}_2$ to independently represent the n^{th} cross section. $\mathbf{b}_3^{[n]}$ and $\mathbf{b}_4^{[n]}$ contain 32 elements each, $\mathbf{b}_5^{[n]}$ contains 1 for each output n, while those in the initial two layers contain 128. The *weight* matrices are sized accordingly.

From previous investigations and a simple hyper-parameter optimization procedure outlined in A.2.2, we found that approximately 32 neurons in each parallel layer is required for a suitable regression of each cross section with more neurons resulting in modest improvements. Here, we choose this minimum to isolate and demonstrate the differences between a MBANN and an equivalent ANN architecture. Each other parameter, such as the activation function and number of hidden layers, was chosen from a set of reasonable values using a comparison of validation accuracy and prior experience. A schematic representation of the MBANN architecture is shown in Figure 4.1.

For comparison, we use an ANN of the form,

$$\sigma(\mathbf{x}) = [\mathbf{A}_5 \circ \text{mish} \circ \mathbf{A}_4 \circ \text{mish} \circ \mathbf{A}_3 \circ \text{mish} \circ \mathbf{A}_2 \circ \text{mish} \circ \mathbf{A}_1](\mathbf{x}), \tag{4.2}$$

where $\mathbf{b}_3$ and $\mathbf{b}_4$ now contain $32 \times N$ elements while $\mathbf{b}_5$ contains N elements to match the number of outputs. The ANN thus contains the same number of neurons per layer as the

MBANN network outlined above. We note however that the number of trainable parameters is larger than that of the MBANN.

Each cross section is a function of the incoming projectile electron kinetic energy, ε, which, alongside the available swarm data, forms the input to the neural network,

$$\mathbf{x} = \begin{bmatrix} \varepsilon \\ \mathbf{W}\left(E/n_0\right) \\ n_0\mathbf{D}_{\mathrm{L}}\left(E/n_0\right) \\ \mathbf{k}_{\mathrm{eff}}\left(E/n_0\right) \end{bmatrix}, \tag{4.3}$$

where n_0, $\mathbf{W}$, $n_0\mathbf{D}_{\mathrm{L}}$ and $\mathbf{k}_{\mathrm{eff}}$ are the neutral density, bulk drift velocity, reduced bulk longitudinal diffusion and effective ionisation rate of the electron swarm evaluated at a number of reduced electric fields E/n_0.

To train each neural network, we generate an appropriate set of physically plausible example swarm transport data using augmentations of cross sections from the LXCat project [52, 72,

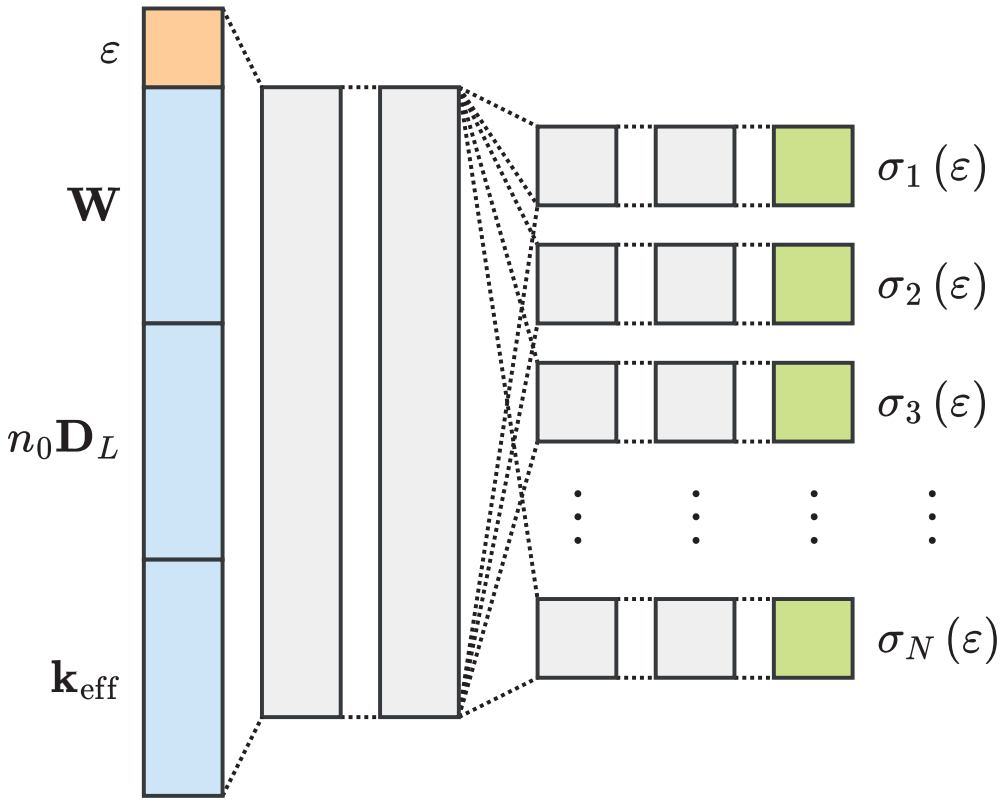

Figure 4.1: Diagram of the multi-branch artificial neural network used for the regression of cross sections (green) as a function of energy (orange), given an associated set of transport coefficients (blue). The first two hidden layers contain 128 neurons while each hidden layer within each parallel branch contains 32 (shown not to scale). While each transport coefficient forms an array of arbitrary length, ε is a single energy value that is varied to scan the energy space. Each output layer then contains 1 neuron and are concatenated to form an array of N elements to match the number of output cross sections.

73, 207]. The data generation process and subsequent training procedure follows the method outlined by Stokes *et al.* [1] with some modifications that are described in detail in A.2.1.

A total of 10^5 training iterations are performed, each consisting of a mini-batch of 32 cross section sampled at 128 energies from a total of 2×10^4 training examples for each cross section. For each training set, a multi-term Boltzmann equation solver was used to calculate $\mathbf{W}$, $n_0\mathbf{D}_\mathrm{L}$ and $\mathbf{k}_\mathrm{eff}$ at 80 log-spaced reduced electric fields between 10^{-3} and 10^4 Td (1 Td = 1 Townsend = $10^{-21}\,\mathrm{Vm}^2$) while the cross section regression was conducted between 0.01 and 200 eV. A detailed outline of the training procedure can be found in A.2.2.

To demonstrate the improvements offered by the proposed architecture, we present a regression of methane's cross section set for both the MBANN and an equivalent ANN network. The cross section set was retrieved from the LXCat database [52, 72, 73] and originates from Biagi's Magboltz code (version v7.1) [179]. In this work, we perform a regression of the elastic momentum transfer cross section (MTCS), total ionisation, total attachment, and each of the 6 excitation cross sections. In addition, while it has been shown that an ANN can determine some energy loss thresholds [1], any target cross section set that exhibits multiple similar threshold processes introduces a high degree of degeneracy. In this work, we assume knowledge of each energy loss threshold and leave their determination for future investigations.

A comparison between the resulting regression for both the ANN and MBANN architectures is shown in Figure 4.2. In each, the extent of the 100 best fits sampled during the training process is shown as a shaded region to provide an indication of the network's variability. The ANN regression resulted in a Mean Absolute Relative Percentage Difference (MARPD, see Equation A.19) of 2.2, 6.3 and 21 % for W, $n_0 D_\mathrm{L}$ and k_eff, respectively. The MBANN regression resulted in a comparable MARPD of 2.7, 5.2 and 21 % for W, $n_0 D_\mathrm{L}$ and k_eff, respectively.

While each network exhibited a similar global accuracy in the replication of transport coefficients, non-physical fluctuations are present in the ANN regression of the elastic and excitation cross sections between $0.1 - 0.4$ eV and $7 - 20$ eV. It is clear that the large gradients present in these regions, due to the energy loss thresholds of 0.162, 0.363, 7.5, 9.1, 12.36, 15.5 and 15.5 eV, resulted in the ANN being unable to independently represent each cross section's feature map when compared to the MBANN fit, despite the same number of neurons available to each architecture. Similar fluctuations were also observed in the best 100 regressions represented by the shaded regions in Figure 4.2. While a larger ANN would mitigate this effect, the MBANN is able to leverage its independent branches to ensure each cross section's feature map is physics-informed and intuitive. The branching architecture also offers a simple linear scaling for variations in the number of target cross sections through the addition, or removal of, individual branches.

As demonstrated by both networks presented here, there remains much room for improvement in the regression of methane's electron-scattering cross section set. While additional

improvements of the network architecture may be available, such as those seen in the work of Jetly *et al.* [105], the ill-posed nature of the inverse swarm problem places an inherent limit on the accuracy of methods that seek to learn the feature map between transport data and cross section sets. In what follows, we aim to mitigate this restriction through a new procedure that uses a sequence of MBANNs to incrementally explore the solution space.

4.2.2 An iterative approach to neural network regression

The regression of numerous similar cross sections poses a substantial challenge for solutions to the inverse swarm problem. As shown previously by Stokes *et al.* [1, 106, 107], the predictive power of the neural network can be improved by restricting the training data to perturbations

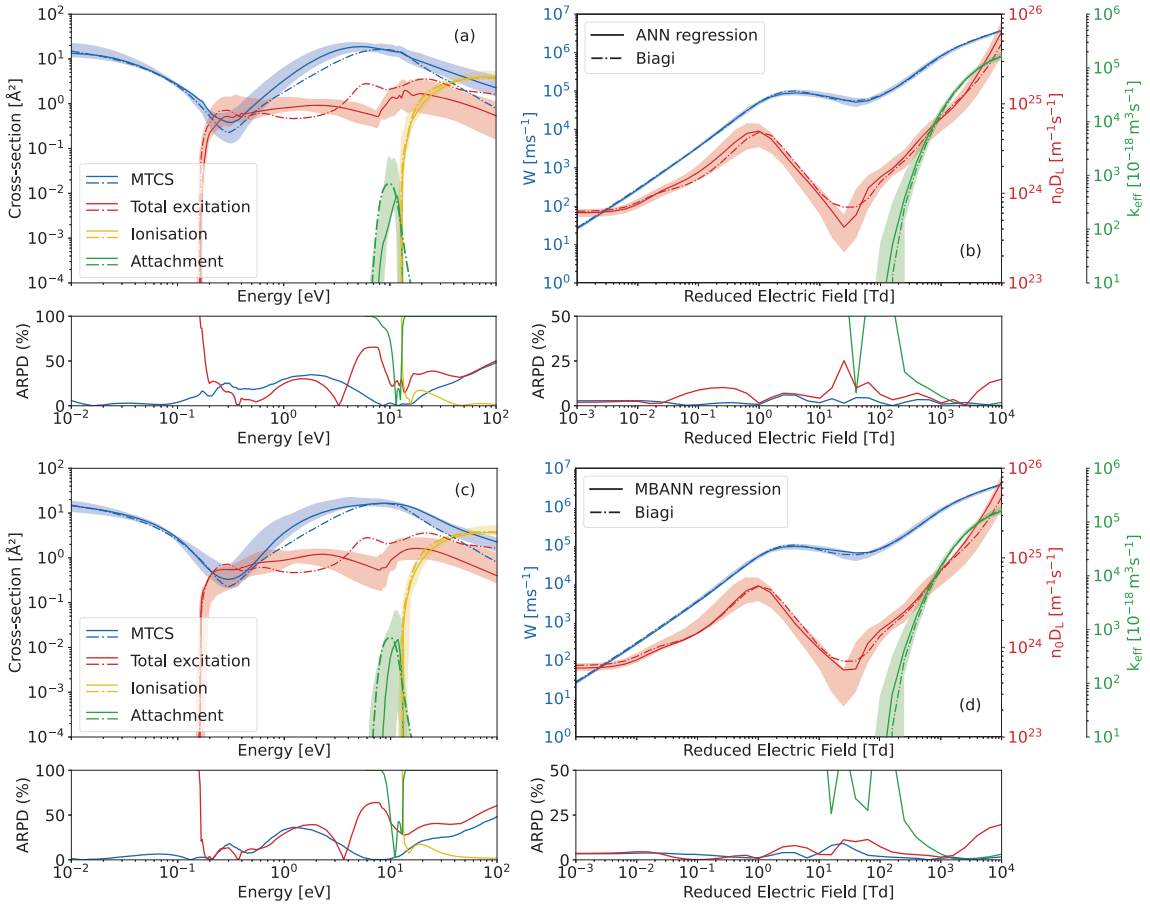

Figure 4.2: Comparison of a conventional (a) and an equivalent multi-branch artificial neural network (c) applied to the regression of Biagi's methane cross section set [179]. While only the total excitation cross section is shown here for simplicity, each of the six excitation processes present in the original set are included in the regression. The bulk drift velocity W, bulk reduced longitudinal diffusion ($n_0 D_L$) and the effective ionisation rate (k_{eff}) for each network is shown in (b) and (d). For simplicity, the legends in (b) and (d) are shared by (a) and (c) respectively. All transport coefficients displayed here are calculated with a multi-term Boltzmann equation solver. Shown as shaded regions, are the extent of the best 100 regressions for the initial regression. Below each figure, is the Absolute Relative Percentage Difference (ARPD) across the energy domain between each regression and the original set.

around a reference cross section set. We extend this work and propose an iterative procedure in which a sequence of networks are trained using a weighted mixing of the previous solution with example cross section data. As illustrated in Figure 4.3, the procedure consists of three phases; initialise, explore and refine.

In the intialise phase we follow the procedure outlined in A.2.2. In this phase, no prior information of the target cross section set is given to the network other than energy loss thresholds and the number of processes present. Each energy loss cross section in the training set is thus energy shifted to their respective target threshold energy. The resulting best 100 regressions then form an array of current fits $\boldsymbol{\sigma}_c$. During the following two phases, we seek to improve the

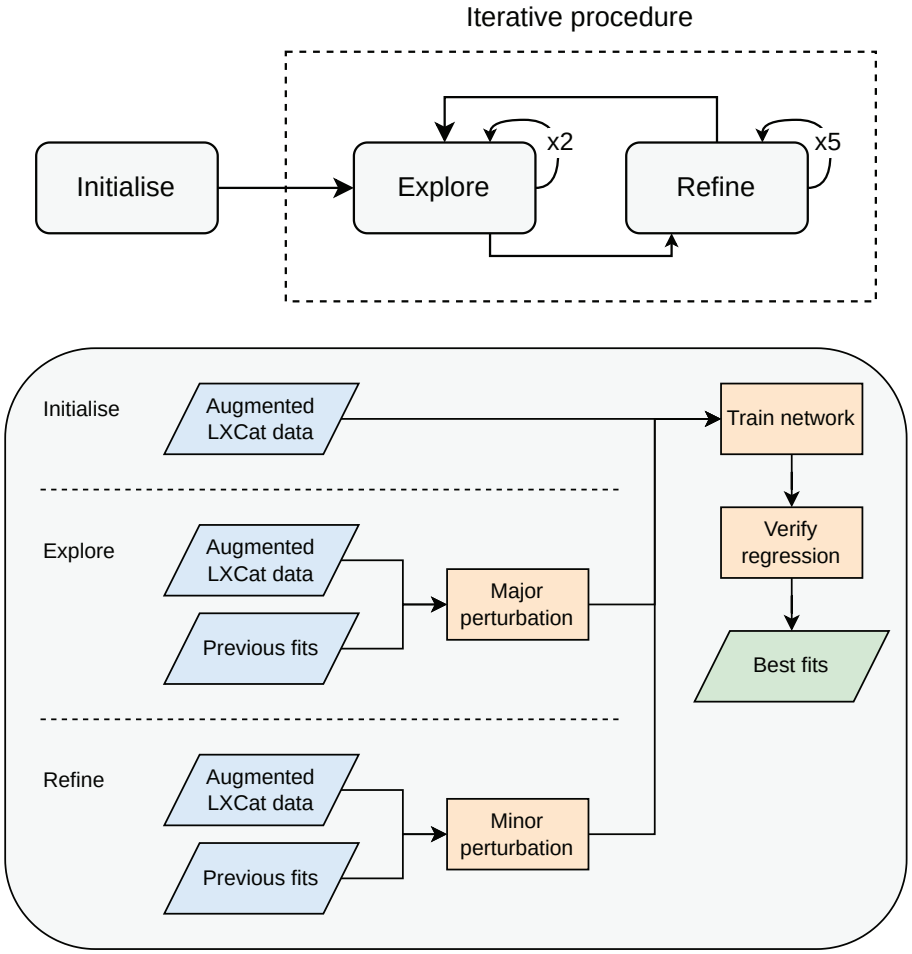

Figure 4.3: Illustrative diagram of iterative neural network procedure (top) along with a flow chart outlining each step (bottom). The procedure consists of 3 phases: initialise, explore and refine. The initialise step follows a similar methodology outlined by Stokes *et al.* [1]. First, training data is generated through augmentations of existing LXCat cross sections [52, 72, 73]. During training, the network's output is periodically sampled and their associated transport coefficients are verified against the target transport coefficients to determine the best 100 fits. In the explore and refine steps, augmented LXCat data are used to generate major and minor perturbations, respectively, of the previous best 100 fits before utilising the same training and verification procedure as the initialisation step.

regression by generating stochastic perturbations around each current fit through a weighted mixing with example cross section data.

To train each subsequent network, we use augmented LXCat cross sections to generate perturbations around each current fit. First, σ_s, is generated with the same method used in the initialisation phase. We then use σ_s to generate a perturbation around the i^{th} current fit $\sigma_{c,i}$ using a weighted sum in log space,

$$\sigma_s(\varepsilon) = \sigma_s^{1-r}(\varepsilon - \varepsilon_s + \varepsilon_t)\,\sigma_{c,i}^{r}(\varepsilon - \varepsilon_{c,i} + \varepsilon_t), \tag{4.4}$$

where i is a uniformly distributed random number and r is a pseudo-random number sampled from a scaled Laplace distribution. ε_s and $\varepsilon_{c,i}$ represent the respective threshold energies for each cross section while ε_t is the target threshold energy. The parameter r then defines how similar each training sample σ_s is to $\sigma_{c,i}$, where values close to 1 results in minor perturbation around $\sigma_{c,i}$ while values close to 0 results in major perturbations. Values of r greater than 1 can be used to produce accentuated perturbations around $\sigma_{c,i}$ to extend the solution space beyond the available data. The extent of these perturbations then define the network's ability to either explore the solution space or refine the existing solution. If the training data is restricted to minor perturbations, the solution may become trapped in a local minimum. Conversely, major perturbations may result in the network being unable to determine a sufficiently accurate cross section set. The explore and refine phases of the procedure aim to strike a balance between these two regimes. In the explore phase, major perturbations of $\boldsymbol{\sigma}_c$ are made to assist the network in traversing the solution space beyond the current fits while in the refine phase, minor perturbations are used to further refine $\boldsymbol{\sigma}_c$.

Through a trial and error process, we found the following parameters to be suitable for each training phase. In the explore phase, we conduct two iterations while in the refine phase we conduct five to help ensure sufficient refinement of a particular solution is conducted after each exploratory phase. For high energy ($> 10\,\mathrm{eV}$) processes, such as electronic excitation and ionisation, we sample r from the domain $[0.5, 0.8]$ for each iteration in the explore phase while during the refine phase we set $r = 0.8$. For low energy processes, such as vibration and elastic, r is sampled from $[0.5, 1.5]$ in the explore phase and $[0.8, 1.2]$ in the refine phase. In the case of low energy processes, r values greater than 1 are used to generate training examples that accentuate low energy cross section features that are present in the sample data.

Direct parallels can be drawn between the iterative MBANN technique and the well known iterative swarm technique. In each, an informed supervisor guides the procedure towards both a physical and accurate solution to the inverse problem. In the iterative swarm technique, this is generally the role of an expert in the field who may make adjustments to the solution or procedure where necessary. In the iterative MBANN technique this role is, in the ideal case, automated by the neural network. Depending on the application, the guidance of an expert may still be required to choose suitable parameters and monitor its performance.

We demonstrate the proposed iterative procedure through a regression of methane's cross section set presented in Section 4.2.1. While 32 neurons was chosen for the hidden layers in each parallel branch as the limiting case in the previous section, we increase this to 64 in what follows due to modest improvements in the validation accuracy. In Figure 4.4, we compare both the initial and the best regression found of methane's cross section set during the procedure, along with their associated transport coefficients.

The associated transport coefficients of the initial fit of methane's cross section set results in substantial discrepancies to the original set. The initial MBANN regression resulted in a MARPD of 1.8, 5.1 and 27 % for W, $n_0 D_\mathrm{L}$ and k_eff, respectively. After 40 iterations, the procedure was then able to substantially improve upon the initial regression with the best iteration resulting in a MARPD of 0.48, 1.69, and 5.84 % for W, $n_0 D_\mathrm{L}$ and k_eff, respectively.

Crucially, we also find substantial improvements in the agreement between the total cross sections for each collision type in the set and the target cross section set. Provided as shaded regions in Figure 4.4, is the extent of the best 100 regressions found in the initial fit. Both the total excitation and the attachment cross section of the best regression exist, in part, outside of the initial extent of $\boldsymbol{\sigma}_c$. The network was therefore able to effectively explore where necessary to improve the resulting fit of the target transport coefficients.

In its current form, the procedure assumes the prior knowledge of threshold energies. This assumption is particularly important when groupings of similar thresholds are present. If instead,

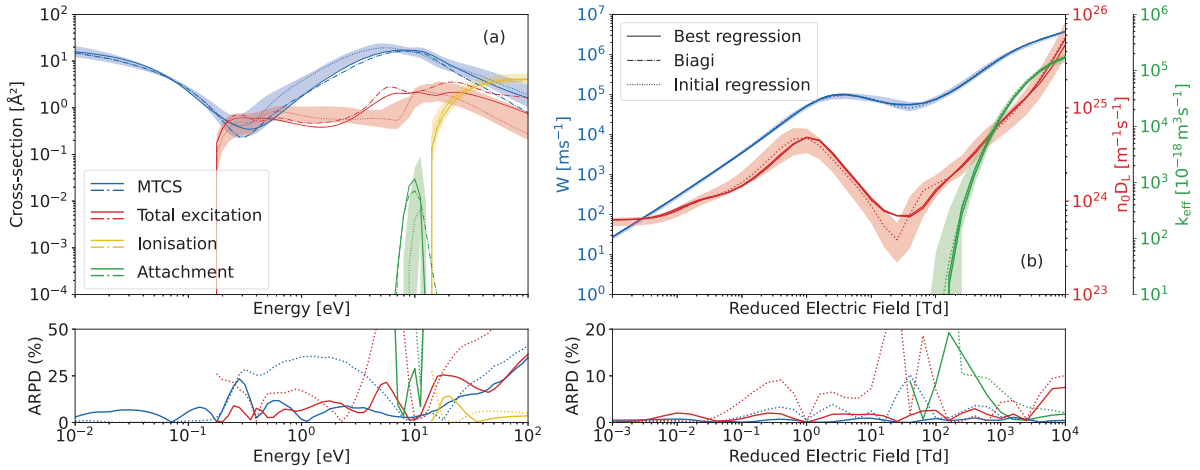

Figure 4.4: MBANN regression of Biagi's methane cross section set [179] using an iterative procedure. (a) compares the initial regression and the best regression found to the original cross section set. While only the total excitation cross section is shown here for simplicity, each of the six excitation processes present in the original set are included in the regression. The bulk drift velocity W, bulk reduced longitudinal diffusion ($n_0 D_\mathrm{L}$) and the effective ionisation rate (k_eff) for each regression is shown in (b). All transport coefficients displayed here are calculated with a multi-term Boltzmann equation solver. Shown as shaded regions, are the extent of the best 100 regressions for the initial regression. For simplicity, the legends in (b) is also shared by (a). Below each figure, is the Absolute Relative Percentage Difference (ARPD) across the energy domain between each regression and the original set.

effective excitation cross sections are utilised in the network to represent groupings of similar threshold energies, this assumption could be avoided at the expense of physical threshold energies in the resulting cross section set.

In this investigation, we utilise only calculated transport coefficients over a large range of reduced electric fields. In reality, such a range is not often available. While tailoring the energy domain of the cross section regression to the transport data available will alleviate the limitation in part, this has limited returns. We thus encourage the measurement of swarm coefficients over a broad range of electric field domains where possible. Finally, while we have made a concerted effort to develop a robust iterative procedure, depending on the particular problem and the extent of available transport data, the network may still produce non-physical cross sections or become trapped in a local minimum. The parameters utilised here should thus only serve as a guide for future applications to be modified as needed.

4.3 Conclusion

In this work, we demonstrate a new iterative procedure that uses a Multi-Branch Artificial Neural Network (MBANN) to solve the inverse swarm problem. Building upon the foundations outlined by Stokes *et al.* [1, 47, 106, 107] and Jetly [105], we address two key limitations of an ANN solution to the inverse swarm problem.

We first evaluate the use of a MBANN that includes an independent branch of dense layers for each output that each stem from common feature map of the input. We then compare the MBANN to an equivalent conventional ANN using Biagi's methane cross section set [179] and demonstrate that the use of parallel layers can improve the resulting regression as the network is able to efficiently and independently represent multiple distinct cross sections.

In addition, taking inspiration from the iterative swarm technique, we propose an iterative MBANN procedure to that incrementally explores the solution space to reduce the ill-posed nature of the problem. After an initial regression is found, we use a sequence of MBANNs that are each trained using perturbations around the previous regression. The iterative MBANN procedure then converges towards a particular solution of the inverse swarm problem.

To demonstrate the iterative MBANN procedure, we evaluate its performance using Biagi's methane cross section set [179]. In the 40 iterations that were conducted, the MARPD of the initial regression's resulting transport coefficients was substantially decreased from 1.8, 5.1 and 27 %, to 0.48, 1.69, and 5.84 % for W, $n_0 D_\mathrm{L}$ and k_eff, respectively. Additionally, the total cross section for each collision type within the best set found exhibited good agreement with the original set, in contrast to the initial regression.

Overall, we have demonstrated an improved artificial neural network solution to the inverse swarm problem that utilises both an iterative procedure and parallel branches of densely con-

nected layers that represent each cross section. In conjunction, these additions improve the ability of the network to generate both self-consistent and physical cross sections, particularly when large degeneracies may exist for a particular species.

In future work, we aim to apply this procedure to derive complete cross section sets for complex targets while also investigating the use of convolutional architectures.

Chapter 5

HFO1234ze(E): electron-scattering cross section set through an iterative deep learning procedure

In this chapter, we utilise the iterative deep learning technique developed in Chapter 4 to determine a complete electron scattering cross section set for HFO1234ze(E), a proposed replacement for SF_6 as an electrical insulation medium in high voltage applications.

The foundation for the deep learning code used here was provided by P. W. Stokes. The code was adapted to include extrapolation of training data (see Appendix A.2), a branching network architecture (see Section 4.2.1) and an automated iterative method that uses deep learning to improve the predicted solution (see Section 4.2.2). To generate the training data for each network used, a multi-term Boltzmann solver written by P. W. Stokes was used and was only modified to include super-elastic collisions. All other work described in this chapter is my own.

5.1 Introduction

Sulphur hexafluoride (SF_6) has long been extensively used as an electrical insulation medium with wider applications in refrigeration, aerospace, medical and chemical industries, among others [208]. However, its high global warming potential (GWP) of 23,800 and the toxicity of its decomposition products, has motivated the search for a suitable replacement. Recently, the molecule (1E)-1,3,3,3-Tetrafluoroprop-1-ene ($C_3H_2F_4$), often termed HFO1234ze(E) or R-1234ze, was proposed [209] as a SF_6 replacement with a GWP just 2 % that of SF_6 [210]. Currently, HFO1324ze(E) exhibits potential applications in many fields such as refrigeration [211–221], cooling technology [222, 223], vapour compression heat pumps [224, 225], resistive plate chambers [226–228], and Rankine cycle systems [229, 230], among others [231–234].

The suitability of HFO1234ze(E) as an electrical insulation medium has been the subject of numerous studies since its proposed use in 2014 [209]. A 2020 review of potential SF_6 replacements found HFO1234ze(E) and CF_3I to be suitable in medium voltage applications [208]. For high voltage applications, HFO1234ze(E) alone was not sufficient due to its high boiling point, except in mixtures with gases such as N_2, CO_2 and synthetic air [42]. In addition, it has been shown that the breakdown voltage for HFO1234ze(E) reduces with subsequent breakdowns at pressures above 2.5 bar, which correlates with the formation of carbon and fluorine on the electrodes [235, 236]. Carbon dust precipitation due to spark-overs in HFO1234ze(E) can also cause short-circuiting on insulation surfaces if appropriate measures are not taken to prevent it [42]. Basu *et al.* [236] thus concludes that HFO1234ze(E) is not promising for switching applications but can be considered for insulations in switchgear applications without discharges.

In addition to its physical properties as an insulation medium, there has been some work to determine the environmental impact of an increase use of HFO1234ze(E). Of particular interest is trifluoroacetic acid (TFA), which is a decomposition product of HFO1234ze(E) that exhibits a molar TFA yield of 10 % under typical conditions [237]. TFA can wash out of the atmosphere, dissolve into water and accumulate in oceans, salt lakes and playas [237–239]. Projections based upon on the replacement of HFC-134a by HFO1234yf, which exhibits a 100 % molar yield of TFA, results in a doubling of TFA concentrations in Eastern U.S. with a concentration of 1264 $\mathrm{ng\,L^{-1}}$, 80 times lower than the lowest level considered safe for aquatic organisms [237, 240, 241]. However, at the time of this study, no data was found on the projected concentrations based upon the proposed partial replacement of SF_6 by HFO1234ze(E). It is clear that more work is needed to understand the environmental impact of HFO1234ze(E).

Measurements of HFO123ze(E)'s critical field strength were made through both a pulsed Townsend experiment [54, 242] and an adapted existing model for breakdown field strengths in SF_6 [42]. It was found that at 130 kPa, HFO1234ze(E) exhibits an electric strength comparable to SF_6 [242]. While pure HFO1234ze(E) features an overall lower critical field strength when compared to SF_6, it's mixture with SF_6 exhibits positive synergy such that the mixture is found to have a higher critical field strength than each of its components [43].

A critical step in the development of predictive models is the derivation of complete electron scattering cross sections. The cross section set can then be utilised in Monte Carlo simulation software and Boltzmann equation solvers to achieve a high level of predictive control when developing new applications. To this end, Petrovic *et al.* [243] proposed the first cross section set for HFO1234ze using an iterative swarm transport method starting from the cross section set for octafluoropropane. Alongside this, in an unpublished paper, Bianchi *et al.* [244] used a similar procedure to obtain a cross section set for HFO1234ze(E) from pure HFO1234ze(E) swarm data and mixture data with CO_2.

Following this, Egüz *et al.* [245] conducted swarm measurements to investigate the positive

synergy effects of HFO1234ze/SF_6 mixtures. Egüz *et al.* found the current cross section sets were unable to replicate the positive synergy observed. To demonstrate their hypothesis that electrons are not sufficiently decelerated through inelastic and elastic processes in HFO1234ze(E), the excitation thresholds were modified according to infra-red spectroscopy measurements conducted by Antinolo *et al.* [246].

In this work, we seek to derive a complete cross section set for electron scattering from HFO1234ze(E) using the iterative deep learning procedure outlined in Chapter 4. In Section 5.2 we outline the current knowledge of HFO1234ze(E)'s cross section set. Following this in Section 5.3, we provide a brief description of the ML technique utilised before presenting and discussing the results. Finally in Section 5.4 we provide a summary of our findings.

5.2 Properties of electron scattering from HFO1234ze(E)

5.2.1 Existing cross sections

In 2016, Chachereau *et al.* [54, 242] presented transport data for pure HFO1234ze and mixtures of Ar, N_2 and CO_2. Petrovic *et al.* [247] later presented a cross section set based on octafluoropropane and derived through an iterative swarm analysis using data from Chachereau *et al.* [54] and de Urquijo *et al.* [248]. In addition, in a currently unpublished paper, Bianchi *et al.* [244] also developed a cross section set from transport data of pure HFO1234ze and a HFO1234ze/CO_2 mixture.

The cross section set of Petrovic *et al.*, presented in the abstract of POSMOL 2019, is replicated in Figure 5.1 for comparison with that of Bianchi *et al.*. We note that two attachment processes were not included in the figure presented of Petrovic's cross section set as the full set was subject to an embargo. In addition, we were unable to reproduce the transport coefficients presented in the work of Bianchi *et. al.* [244], which may be attributed to digitisation errors or missing cross sections. Hence, we only compare the cross section sets available and not their resulting transport coefficients.

Overall, both cross section sets differ significantly with only general trends being similar. A three-body attachment process is present in both as resonant type reactions centered around different energies. Each found a general dip in the elastic cross section between 0.01 and 10 eV, which corresponds with an increase in the total excitation cross sections. Petrovic's cross section set is more accentuated with larger excitation processes and a smaller elastic cross section. Petrovic's ionisation process exhibits a threshold energy around 10 eV while Bianchi's is closer to 8 eV.

5.2.2 Positive synergy in HFO1234ze/SF_6 mixtures

In 2022, Egüz *et al.* [245] conducted swarm measurements to investigate the positive synergy effects of HFO1234ze/SF_6 mixtures. The authors found the current cross section sets presented by Petrovic *et al.* were unable to replicate the positive synergy observed. Based on their investigation it was determined that an increase in negative HFO1234ze(E) ions in the presence of SF_6 is only partially responsible for the positive synergy observed. They proposed an alternative hypothesis that positive synergy can occur through a strong electron energy moderation in combination with thermal attachment. Through increasing the excitation thresholds according to infra-red spectroscopy conducted by Antinolo *et al.* [246], Egüz *et al.* showed that positive synergy can indeed be achieved through a moderation of electron energy.

5.2.3 Electron excitation and ionisation energies of HFO1234ze(E)

Since Egüz's investigation, Schwabedissen *et al.* [249] utilised single-crystal and gas-phase X-ray diffraction data to describe the vibrational spectra of HFO1234ze. Available in the supplementary material, the authors list both experimentally derived and calculated vibrational frequencies for the various phases of HFO1234ze. Restricting the vibrational frequencies labelled as medium in strength or greater, we find agreement with the thresholds selected by Egüz *et al.* other than an additional medium strength vibrational frequency at 0.087 eV.

In an unpublished paper, Benussi *et al.* [250] utilised the quantum chemistry calculation tool NWCHEM to calculate ionisation energies, electron affinities and the absorption spectrum for various potential eco-friendly gas replacements. The authors calculate the ionisation energy of HFO1234ze by optimising the geometry of both the neutral gas molecule and its positive charged ion for the spin-unrestricted Hartree-Fock wave functions. The vertical ionisation energy was then calculated through the difference in ground state energies between the two. The authors found the vertical ionisation energy to be 9.34 eV. In 2017, Liang *et al.* [251] used

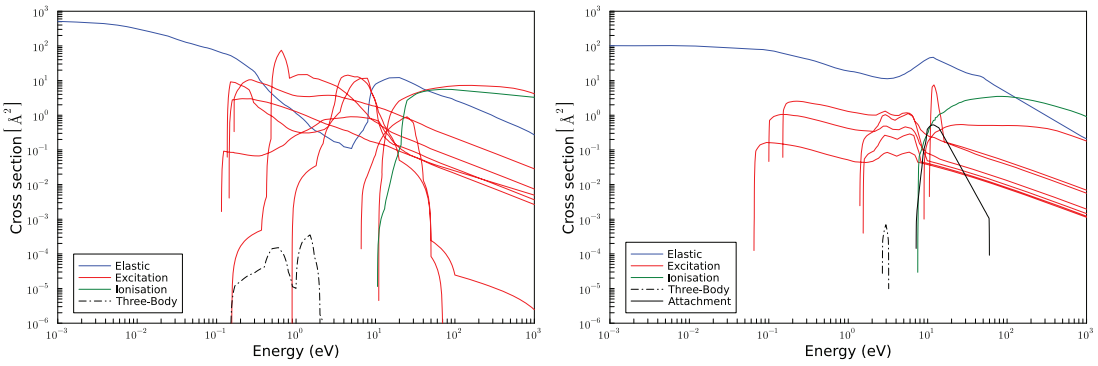

Figure 5.1: Comparison of the electron-scattering cross section sets of Petrovic *et al.* [247] (left) and Bianchi *et al.* [244] (right). Note that two attachment cross sections are missing in the set developed by Petrovic *et al.* due to an embargo.

density functional theory to investigate the structural and electrical properties of HFO1234ze(E). The authors found a variation in ionisation energy when electric field strength increased from -0.025 to 0.03 a.u.. At a field of 0 a.u., the ionisation energy of HFO1234ze(E) was found to be 10.8 eV. Following this, Ray *et al.* [252] utilised imaging photoelectron photoion coincidence spectrosopy to determine the adiabatic ionisation energy of HFO1234ze to be 10.91 ± 0.05 eV. Three dissociative processes were also observed at 12.247 ± 0.030 eV, 12.66 ± 0.10 eV and 12.80 ± 0.05 eV. Recently, Gan *et al.* [253] used Gaussian09 to calculate the structure and energies of all reactants and products of HFO1234ze(E). The authors found an ionisation energy of 11.24 eV for HFO1234ze(E). Additionally, Egüz *et al.* [245] utilised density functional theory to find an ionisation energy of 10.6 eV and first electronic excitation energy of 6.6 eV.

Overall, numerical predictions of the ionisation energy for HFO1234ze(E) vary from 9.34 to 11.24 eV while reported experimental measurements vary from 10.8 to 10.91 eV. In addition, dissociative processes were observed above 12.24 eV and a first electronic excitation energy of 6.6 eV was found using density functional theory. These parameters will serve to inform and constrain the cross section set presented in what follows.

5.3 Deep learning regression of HFO1234ze(E)'s electron scattering cross section set

In what follows, we use the iterative machine learning technique outlined in the previous section. For simplicity, pressure is directly used as the scaling factor for the three-body attachment cross section. For the vibrational, electronic and dissociative processes we use the threshold energies presented by Hösl *et al.* [43] while for the ionisation threshold defer to the experimentally derived value of 10.91 eV determined by Ray *et al.* [252] as there is some variation in theory.

Initially, only a single three-body and a single two-body attachment cross section were included in the fitting procedure. When utilising mixture data with CO_2, the network would tend to predict two distinct cross section features for the single two-body process. One of these was located at low energies (< 0.1 eV) with the other between 1 and 10 eV. This indicated the existence of a separate thermal attachment process. To accommodate this, we sorted the example attachment cross sections taken from LXCat into two categories; thermal and attachment. The thermal category was defined by a cross section magnitude greater than 10^{-5} Å at 0.1 eV. While this is a crude definition, upon visual inspection of the examples we determined that this was sufficient to create two distinct types of attaching processes. During training, the network was then tasked with predicting three attachment; thermal, normal and three-body.

For this work, we use the swarm data from the ETH Zurich, High Voltage Laboratory (ETHZ) group available on LXCat [254]. The database contains drift velocity, longitudinal diffusion and effective ionisation rate transport coefficients for HFO1234ze(E) and its mixtures with Ar,

N_2, CO_2 and SF_6 for a variety of mixture ratios and pressures. Including every dataset in the deep learning procedure was infeasible however due to substantial computational burden of the Boltzmann solver so we select a representative sample of mixture ratios and pressures. Listed in Table 5.1 are the parameters available (normal font) and those chosen for use in this work (**bold font**). Note that mixtures of HFO1234ze(E) with N_2 were not used in the results that follow as a suitable cross section set for N_2 that included rotational scattering cross sections was not compiled. Attempts were made to include Ar mixture data but, as we outline at the end of this discussion, their inclusion proved problematic for the resulting regression.

To demonstrate the effect of the inclusion of mixture swarm data on the resulting network regression, we incrementally include mixture data from CO_2 and SF_6 and show the resulting regression. First, in Figure 5.2, we utilise only the pure HFO1234ze(E) transport data in the iterative deep learning procedure. In this fit, the thermal attachment cross section was not implemented as the transport data present was not sufficient to resolve it. Shown below the best regression found are the resulting transport coefficients compared to the experimental data for the pure case along with mixtures with CO_2 and SF_6. For the pure swarm data, we find good agreement between the regression and experiment. As expected, both the reduced longitudinal diffusion and effective ionisation rate for the two mixtures investigated exhibit significant discrepancies. The drift velocities for both mixtures found reasonable agreement with experiment. Given the procedure was given no information for each mixture in this fit, it is promising that this cross section set was broadly able to replicate the measured transport coefficients with reasonable accuracy. The Mean Absolute Relative Percentage Difference for each scenario investigated can be found in Table 5.2.

As discussed previously, HFO1234ze(E) may find applications as a dielectric insulator in high voltage applications. Due to this we are most interested in the critical field strength and positive synergy effects observed in mixtures with SF_6. Thus, of particular concern for this

Mixture gas	HFO1234ze(E) percentage (%)	Pressure (kPa)
Pure	**100**	0.3, **3**, **6**, 8, **10**, 12, 15, 20,
	100	25, **30**, 35, 40, 45
CO_2	0.5, 1.2, **10**, 30.1	**10**
	50	**6**, 8, **10**
	75.0	3, 4, 6, 8, **10**
SF_6	99.965	1,2,3,4,5,6,7,8,9,10,11
	1.30, 6.00, 16.50, 24.80, 34.70, **40.06**,	$\approx$ **0.4**
	45.57, 50.12, 60.19, 64.89, 69.92, 75.00,	$\approx$ **0.4**
	79.89, 84.90, 90.10, 95.11, 96.99, **98.89**,	$\approx$ **0.4**
	99.00	$\approx$ **0.4**

Table 5.1: Available swarm transport data from the ETHZ group on LXCat [254]. We note that for the last row of SF_6 data, the pressure varies from 0.36 to 0.48 for each ratio, each other parameter has been rounded to the second decimal place where more precision was stated.

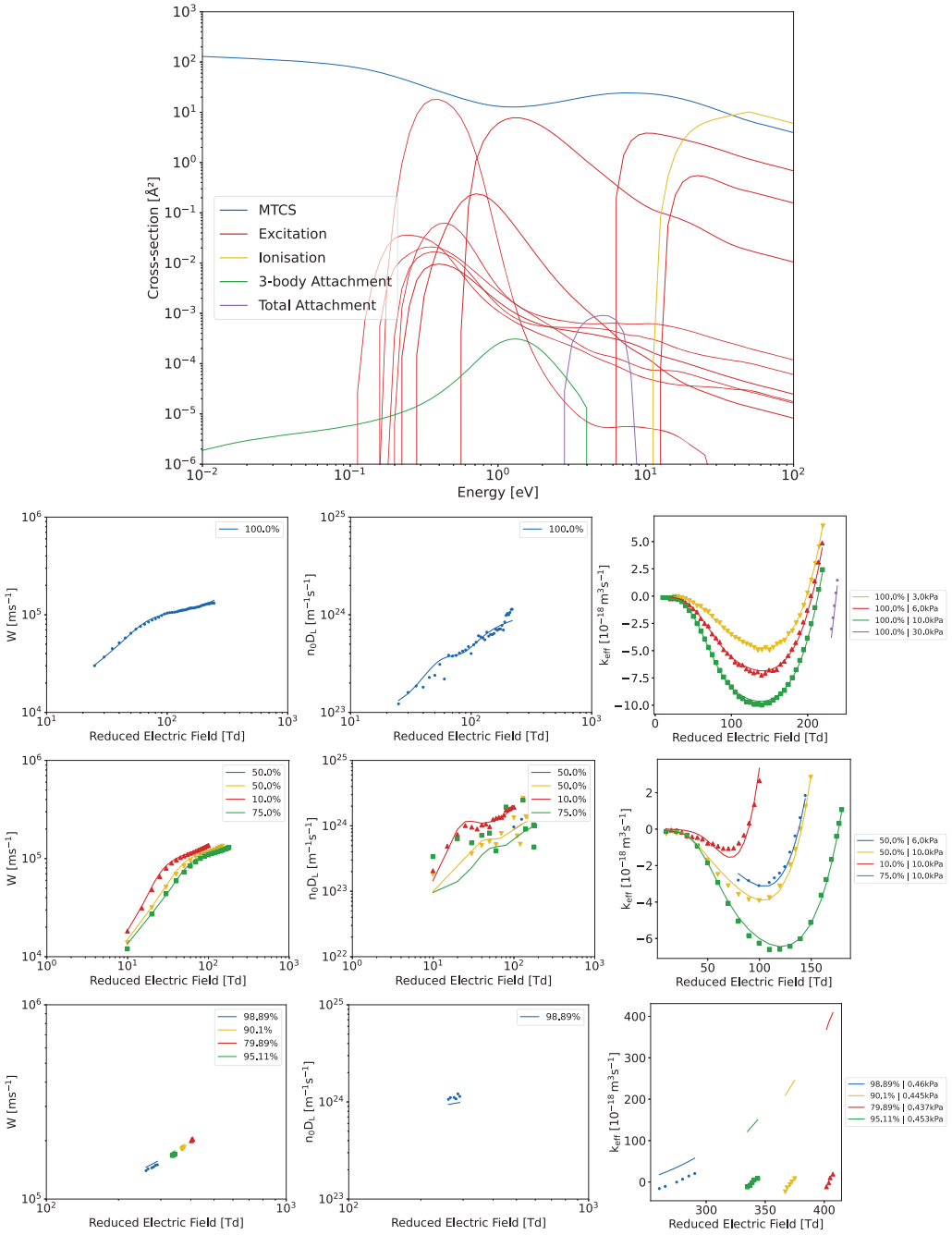

Figure 5.2: Iterative deep learning fit of HFO1234ze(E)'s electron scattering cross section set using only the pure gas transport coefficients. Shown here is the final cross section set (top) along with its associated effective ionisation rates (right column), bulk drift velocity (left column) and reduced longitudinal diffusion coefficient (center column) compared with the ETHZ experimental data [54, 242, 255]. Transport coefficients for the pure (top row) are shown along with HFO1234ze(E)/CO_2 (middle row) and HFO1234ze(E)/SF_6 (bottom row) mixture data. Only the mixture ratios and pressures included in the iterative MBANN procedure are shown here.

investigation is the large discrepancies observed in the effective ionisation rate in mixtures with SF_6.

Shown in Figure 5.3, we then include the HFO1234ze(E)/CO_2 mixture data, in addition to the pure data, in the training data of the procedure. We find an improved fit of the CO_2 effective ionisation rate and a worsened fit of the effective ionisation rate in the pure case. There was modest improvement in $n_0 D_L$ for the CO_2 mixture and a decrease in accuracy for the pure case. Drift velocity saw a decrease in fit accuracy for all three scenarios. Overall, the network struggled to fit both the pure and mixture transport coefficients. While it was hoped that the inclusion of additional mixture data would improve the cross section prediction, the decrease in accuracy could be the result of the increased complexity of the data. Given the assumed threshold energies in this work, if the true threshold energies are not represented then the network would be unable to, by nature, find a cross section set close to the true solution. In this case, the addition of mixture transport data would only worsen the resulting prediction. We also note that the diffusion data available for CO_2 contains large variations that could be the result of data that is too sparse to capture the appropriate features, or large experimental noise. While it was not attempted here, it would be informative to replicate the fitting procedure without the longitudinal diffusion data for CO_2 in order to determine its affect on the resulting cross section set.

Finally, in Figure 5.4, we include both HFO1234ze(E)/CO_2 and HFO1234ze(E)/SF_6 mixtures in the network regression, in addition to the pure data. We find that while k_{eff} exhibits an improved fit for SF_6 mixtures, the corresponding fit of both the pure and CO_2 mixture data has degraded. The cross section set predicted here replicates the positive synergy observed in experimental data while retaining a reasonable fit of the pure and CO_2 mixture transport coefficients, which, to our knowledge, has not been demonstrated elsewhere. This cross-section set was utilised in a recent publication by Garland *et al.* [256]. Shown in Figures 5.5- 5.7, are the same predictions shown in Figures 5.2- 5.4, but with all available transport data displayed in the interest of completeness.

During this work, several attempts were made to include Ar mixture data in the regression. However it became clear that the network was unable to produce a suitable fit when Ar was included. We do note that the diffusion data for pure Ar for the ETHZ group differs by a consistent amount for high reduced electric fields than those available elsewhere on LXCat. This

	Pure			HFO1234ze(E)/CO_2			HFO1234ze(E)/SF_6		
Training data	ΔW	ΔD_L	Δk_{eff}	ΔW	ΔD_L	Δk_{eff}	ΔW	ΔD_L	Δk_{eff}
Pure	0.93	5.07	9.44	1.44	15.38	20.24	1.78	7.25	91.79
Pure, CO_2	3.24	6.27	16.54	1.32	14.96	10.64	2.91	8.80	88.68
Pure, CO_2, SF_6	2.73	13.48	22.02	1.42	13.27	28.21	3.01	4.05	63.92

Table 5.2: Mean Absolute Relative Percetange Difference of drift velocity (W), longitudinal diffusion (D_L) and effective ionisation rate (k_{eff}) for each combination of training data used.

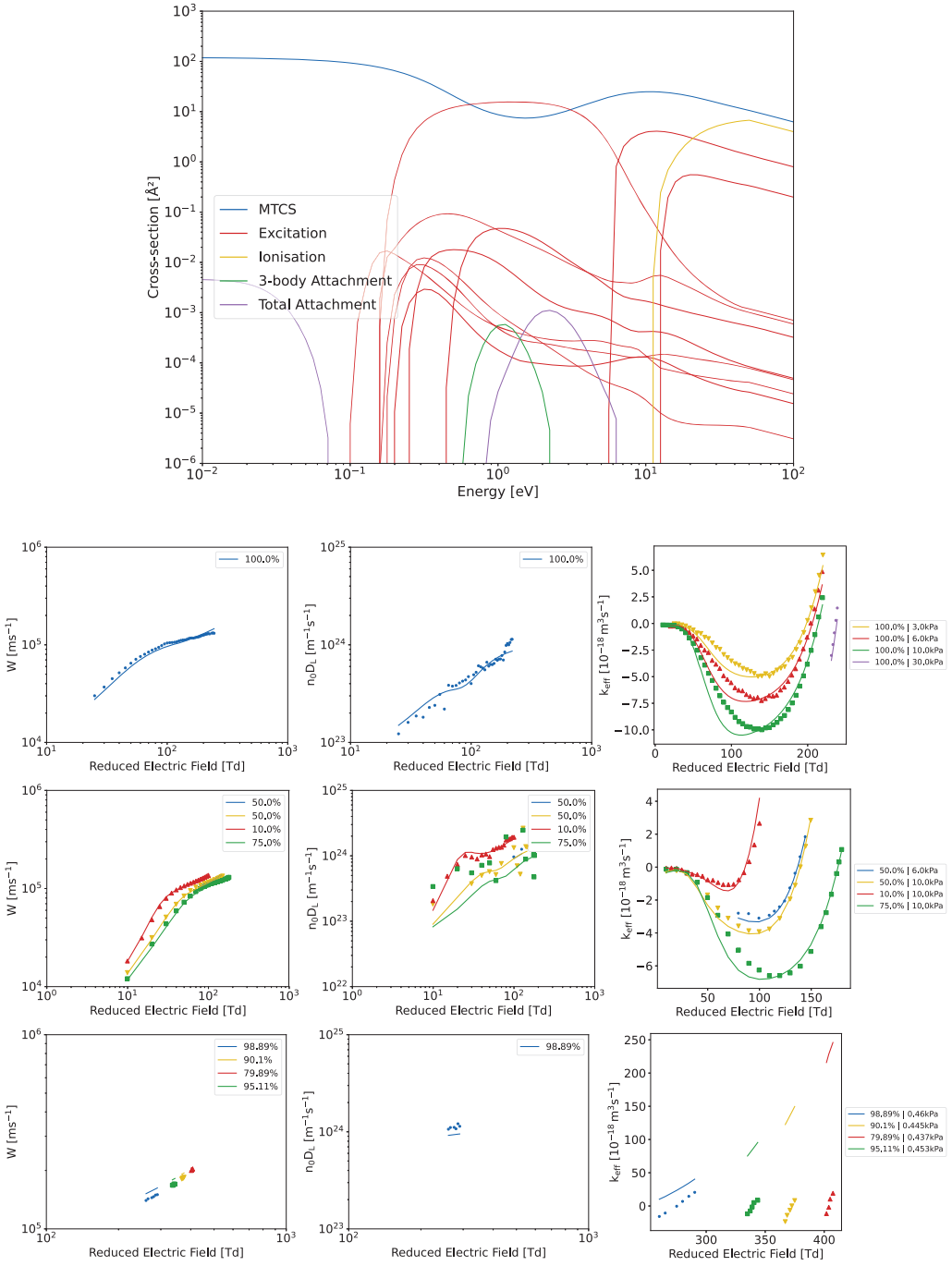

Figure 5.3: Iterative deep learning fit of HFO1234ze(E)'s electron scattering cross section set using both pure and HFO1234ze(E)/CO_2 transport coefficients. Shown here is the final cross section set (top) along with its associated effective ionisation rates (right column), bulk drift velocity (left column) and reduced longitudinal diffusion coefficient (center column) compared with the ETHZ experimental data [54, 242, 255]. Transport coefficients for the pure (top row) are shown along with HFO1234ze(E)/CO_2 (middle row) and HFO1234ze(E)/SF_6 (bottom row) mixture data. Only the mixture ratios and pressures included in the iterative MBANN procedure are shown here.

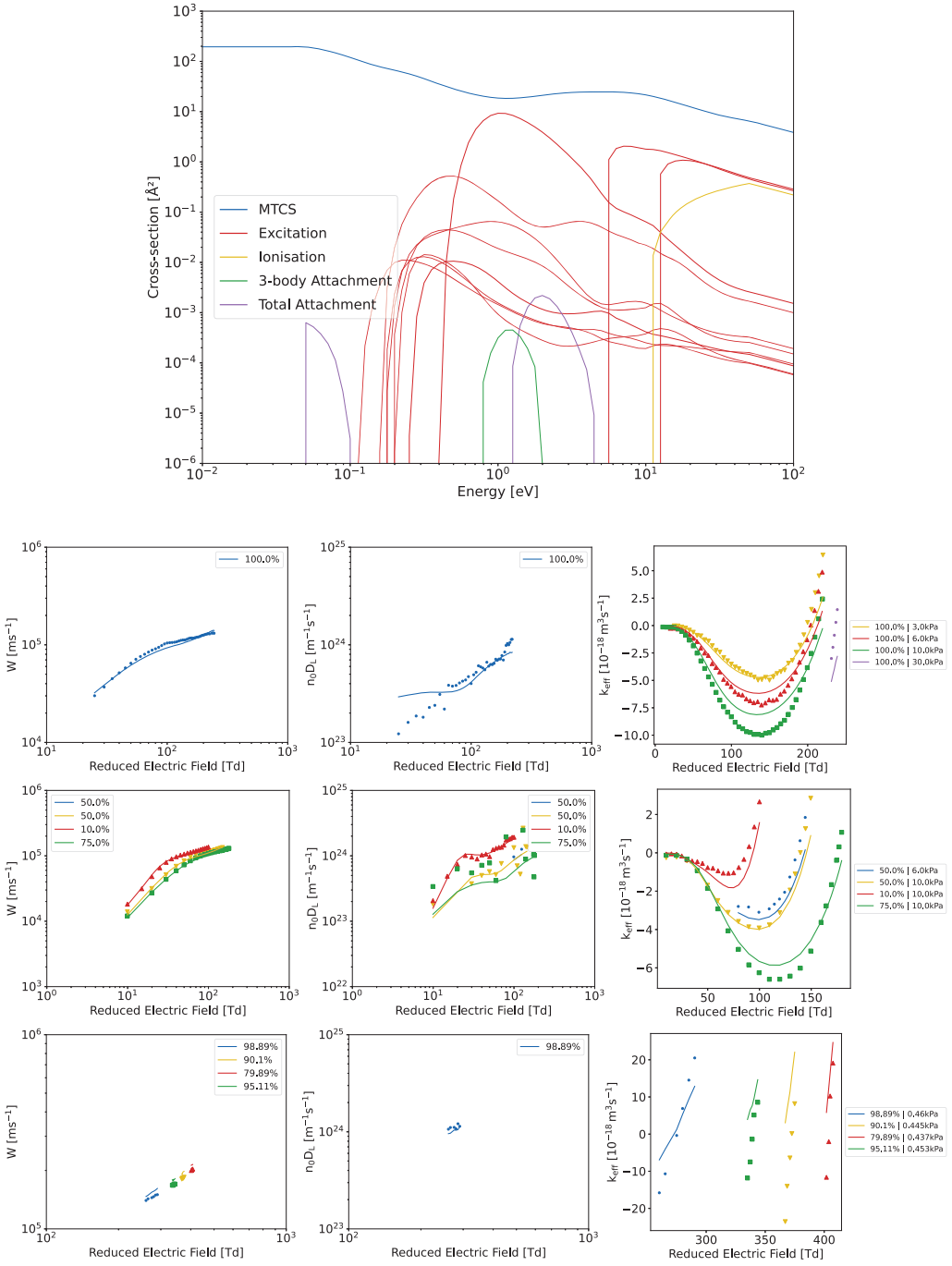

Figure 5.4: Iterative deep learning fit of HFO1234ze(E)'s electron scattering cross section set using pure, HFO1234ze(E)/CO_2 and HFO1234ze(E)/SF_6 transport coefficients. Shown here is the final cross section set (top) along with its associated effective ionisation rates (right column), bulk drift velocity (left column) and reduced longitudinal diffusion coefficient (center column) compared with the ETHZ experimental data [54, 242, 255]. Transport coefficients for the pure (top row) are shown along with HFO1234ze(E)/CO_2 (middle row) and HFO1234ze(E)/SF_6 (bottom row) mixture data. Only the mixture ratios and pressures included in the iterative MBANN procedure are shown here.

could indicate a systematic difference in the experimental procedure between groups and would require a new Ar cross section set that matches these results. At this time it is unclear how significant this affect could be and the investigation of it is left for future work.

5.4 Conclusion

We have presented initial results from an iterative deep learning regression of HFO1234ze(E), a potential candidate to substantially reduce the prevalence of SF_6 in dielectric insulators. We first investigated the suitability of the current proposed cross section sets for HFO1234ze(E) available in the literature and review the current knowledge of electron-scattering processes from HFO1234ze(E). We then utilise the swarm experiment data of the ETHZ group available on LXCat [254] in an iterative deep learning procedure that was outlined in Chapter 4 to develop a full electron-scattering cross section set.

Overall, we find promising results when HFO1234ze(E)/CO_2 and HFO1234ze(E)/SF_6 mixture data are included in the regression. Discrepancies in the reduced longitudinal diffusion coefficient and effective ionisation rate were still present however. These discrepancies suggest that either the true cross section set exists outside the training data used in this work or experimental noise was affecting the consistency of data between mixture ratios. In particular, it is crucial to verify the excitation thresholds used where possible as incorrect threshold energies would hinder the resulting prediction.

The inclusion of HFO1234ze(E)/Ar was found to be particularly problematic for the network regression, which could be a result of differences in the stated diffusion coefficient between the ETHZ group and others. However, the significance of this difference was not investigated here and is left for future work. In addition, HFO1234ze-N_2 mixtures were not used in this work as a complete cross section set that included rotation cross sections was not compiled. The inclusion of N_2 would provide additional leverage to unfold the true cross section set and is left for future work.

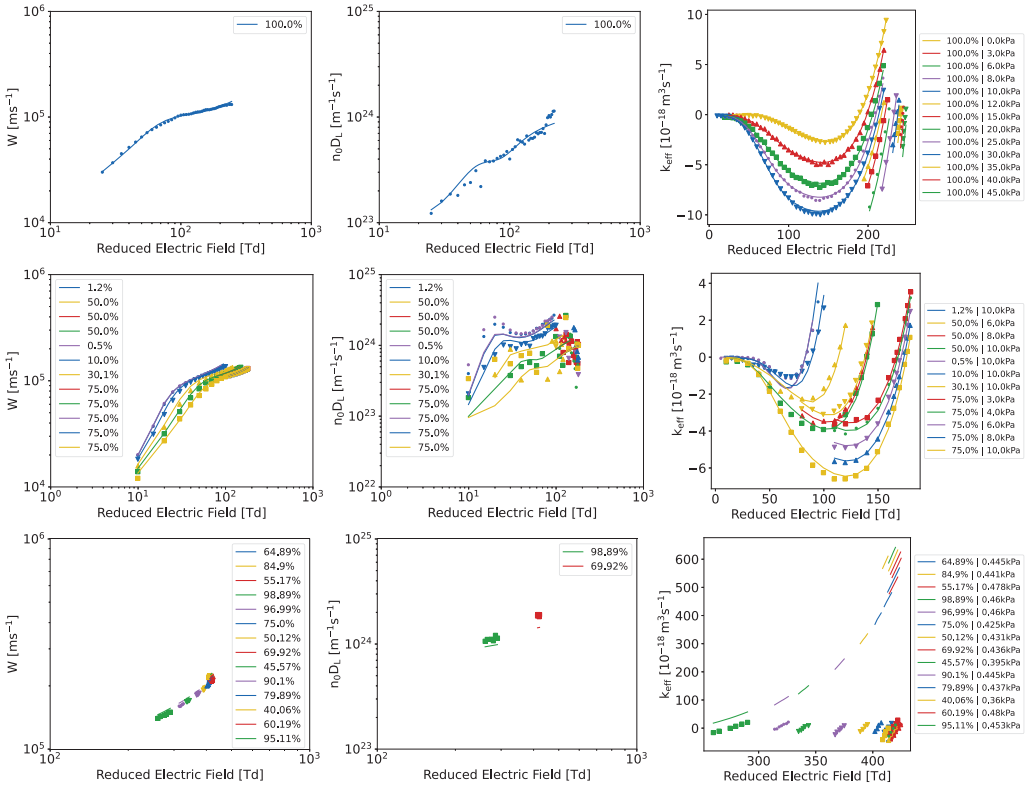

Figure 5.5: Iterative deep learning fit of HFO1234ze(E)'s electron scattering cross section set using only the pure gas transport coefficients. Shown here is all the associated effective ionisation rates (right column), bulk drift velocity (left column) and reduced longitudinal diffusion coefficient (center column) compared with the ETHZ experimental data [54, 242, 255]. Transport coefficients for the pure (top row) are shown along with HFO1234ze(E)/CO_2 (middle row) and HFO1234ze(E)/SF_6 (bottom row) mixture data.

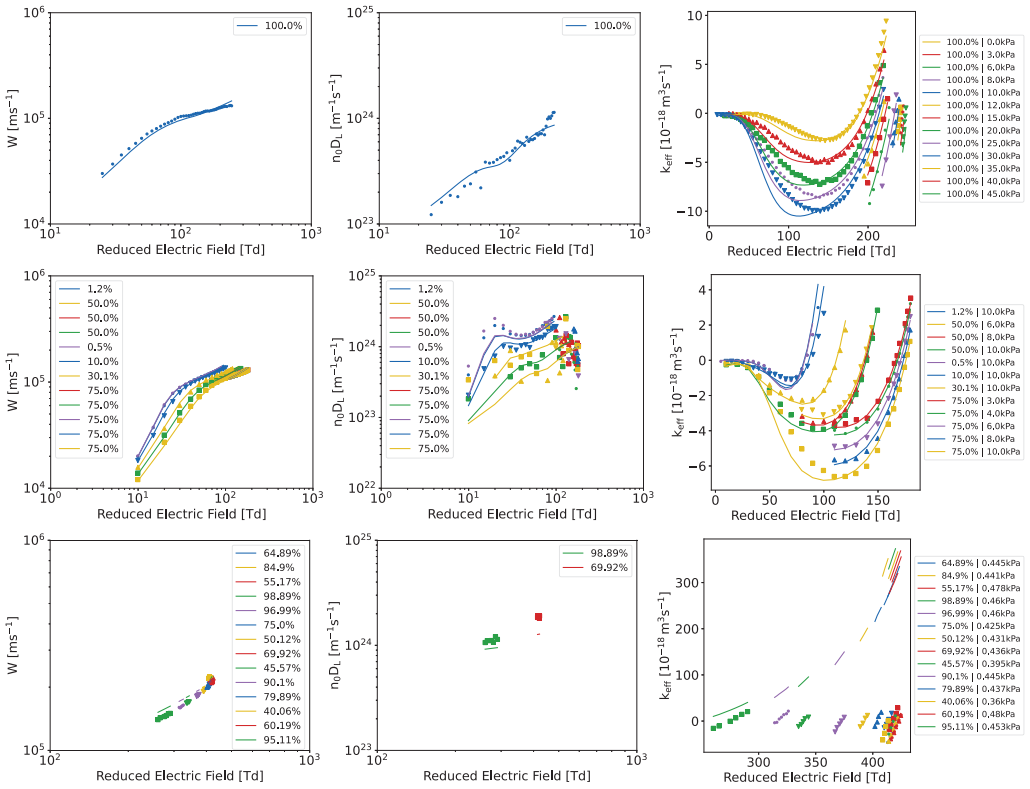

Figure 5.6: Iterative deep learning fit of HFO1234ze(E)'s electron scattering cross section set using both pure and HFO1234ze(E)/CO_2 transport coefficients. Shown here is a all the associated effective ionisation rates (right column), bulk drift velocity (left column) and reduced longitudinal diffusion coefficient (center column) compared with the ETHZ experimental data [54, 242, 255]. Transport coefficients for the pure (top row) are shown along with HFO1234ze(E)/CO_2 (middle row) and HFO1234ze(E)/SF_6 (bottom row) mixture data.

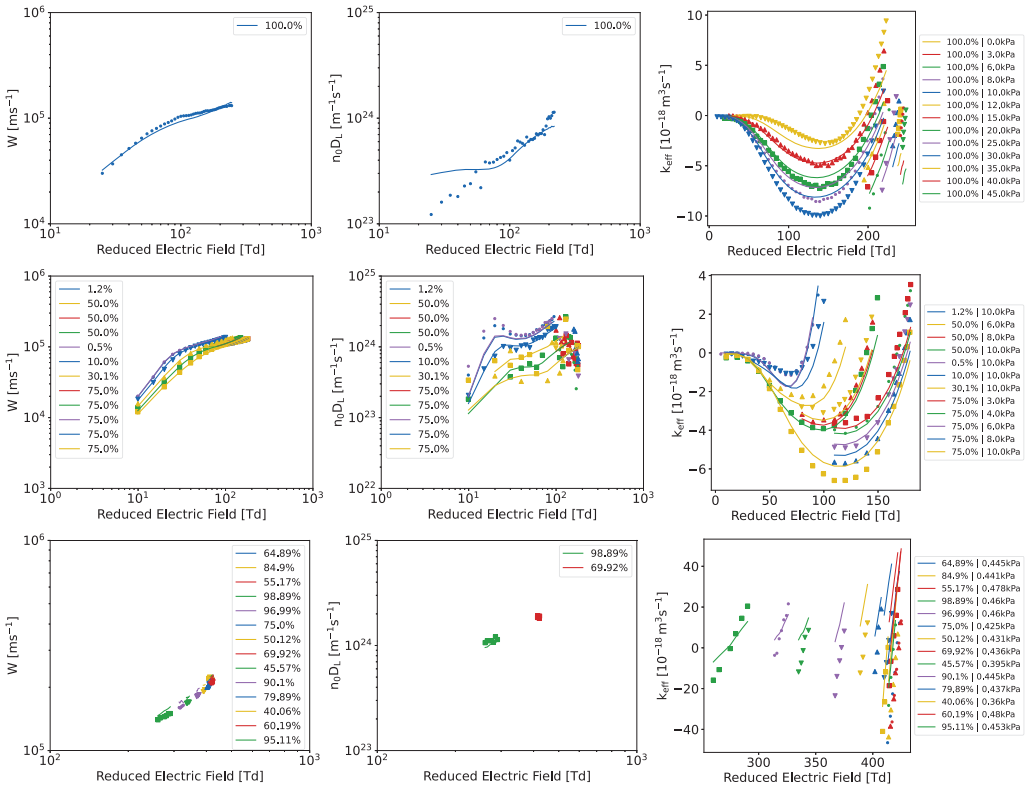

Figure 5.7: Iterative deep learning fit of HFO1234ze(E)'s electron scattering cross section set using pure, HFO1234ze(E)/CO_2 and HFO1234ze(E)/SF_6 transport coefficients. Shown here is all the associated effective ionisation rates (right column), bulk drift velocity (left column) and reduced longitudinal diffusion coefficient (center column) compared with the ETHZ experimental data [54, 242, 255]. Transport coefficients for the pure (top row) are shown along with HFO1234ze(E)/CO_2 (middle row) and HFO1234ze(E)/SF_6 (bottom row) mixture data.

Chapter 6

Conclusion

6.1 Summary

Understanding of electron transport through gases and soft-condensed matter is crucial for the development of a number of crucial technologies and applications. Applications of electron scattering are widely varying and include important fields such as radiation therapy, plasma medicine, dielectric insulators and liquid particle detectors. The advancement of these technologies relies on utilising an understanding of microscopic electron interactions with complex targets to inform modeling methods and gain predictive control of the system. The scope of this thesis has been to develop new techniques and improve existing methods that aid in developing our understanding of electron scattering mechanics through liquids and complex biological matter. There exist two gaps in existing methods that motivate this work.

The first gap is a limited ability of experimental techniques to measure electron scattering directly from liquid targets in a vacuum environment. In this work, we have presented a new experiment that utilises a $15-40\,\mu$m jet of liquid water to produce a stable scattering surface within a vacuum environment. To aid in the development of the experiment, a Monte Carlo simulation package was extended and used to conduct a sensitivity study of the experiment. We found some promising dependence of the electron signal on the relative magnitude of cross sections and the differential cross section. However, the effects of multiple-scattering substantially convoluted this dependence, resulting in a highly ill-posed problem.

Considering this, we implemented a deep learning approach that has previously shown promise in aiding the derivation of cross sections from the ill-posed inverse swarm problem. Using simulations of the experiment to generate a wealth of training data for the network, we have shown that deriving both the elastic momentum transfer and ionisation cross sections of neon was feasible, assuming knowledge of each other cross section. The extension to deriving each excitation cross section however was not possible, without further improvements to the methods used or additional measurements.

Following this, the liquid micro-jet experiment was setup at Flinders University and initial tests were conducted. We first calibrated the scattering chamber with the aid of the Monte Carlo simulation package before presenting initial measurements of the energy loss spectra for both the liquid jet and an effective gas jet. Due to time limitations, the measurements have limited validity due to a) the presence of magnetic fields and b) instabilities of the jet that may have caused inconsistencies in the chamber pressure. Regardless, promising similarities were found between the measurement obtained and an equivalent simulation using an existing cross section set for water. Some discrepancies in the excitation signal were observed however, which, in addition to the need for robust and well calibrated measurements, motivates the need for further investigation.

The second gap in existing knowledge that we aimed to address in this work, is the ill-posed nature of the inverse swarm problem for the determination of complete sets of electron impact cross-sections. Two improvements were made that extend the existing deep learning solution of the problem. First, we developed a branching network architecture and demonstrate that, when compared to an equivalent conventional network, leverages a physics-informed design to efficiently derive physically sound cross section sets. We then developed an iterative approach that further refines the initial solution found by the network using training sets consisting of perturbations of the previous solution found. By restricting the solution space in subsequent networks, we demonstrate that the network is able to substantially improve the solution to both match the target transport coefficients and replicate the underlying cross section set.

Finally, we applied this technique to the derivation of an electron scattering cross section set for HFO1234ze(E), a proposed lower global warming potential alternative to SF_6 in dielectric insulators. We present for the first time, as far as we are aware, a self-consistent cross section set for HFO1234ze(E) that replicates the positive synergy effect observed in mixtures with SF_6. We also investigate the importance of using mixture data to inform derivation techniques through the incremental inclusion of mixtures with CO_2 and SF_6. While we find reasonable fits of the transport data available, the results indicate that there is still room for improvement in the iterative deep learning procedure, or the assumptions used here, to achieve a robust and general regression of complete cross section sets.

Overall, through this work we have advanced both experimental and numerical techniques used for the derivation electron scattering cross section sets for liquids and complex gases. We have presented a new experiment that is able to directly measure electron scattering from liquids under vacuum conditions. A Monte Carlo package was also developed to investigate the potential applications of the experiment and guide its design before conducting the first direct electron-liquid scattering measurements at Flinders University. In addition, we have presented a new deep learning technique that addresses, in part, the ill posed nature of solving the inverse swarm problem for complex molecules. Finally, we applied this technique to produce the first

self-consistent electron-scattering cross section set for HFO1234ze(E), a proposed low global warming potential alternative for the insulation of high voltage equipment.

Together, these advances broaden the horizon for particle physics through new techniques that leverage the union of deep learning and electron-scattering experiments.

6.2 Recommendations for future work

Both the liquid micro-jet experiment and iterative deep learning method developed here present several opportunities to both refine their methods and extend their application.

6.2.1 Liquid micro-jet

While the methodology presented here shows promise, we were unable to validate the stability of the jet over longer time periods and the reproducibility of the measured data. Validating this procedure and making any necessary modifications to improve stability and reproducibility is required for future investigations. This could include:

- Alignment rods fed through each detector could be used to ensure the interaction region may be located precisely.
- A Faraday cup could be used to determine a reference intensity for the electron beam and the alignment of the jet.
- As seen in the work of Nag *et al.* [257], switch samples while ensuring continuous flow would allow the use of high vapour pressure samples like isopropyl alcohol to start the jet under vacuum by preventing freezing due to the inconsistent nature of initial sample flow.
- Measurements of the positional dependence of the electron signal to investigate the cause for the inconsistency observed in this work.
- Reproduction of each measurement presented here with minimal interference from Earth's magnetic field through the use of the Helmholtz coils.

In addition, there are unanswered questions surrounding the derivation of cross sections from the LμJ experiment:

- While an attempt was made to use deep learning to resolve the differential cross section from angle dependent scattering data, this work was not completed. Initial results indicated that the degree of forward or backward scattering could be determined, but that the functional features within the DCS were more difficult to resolve. This indicated that the data provided, which were angle dependent intensity spectra only, was degenerate in nature.

- The methods discussed in Chapter 4 could be utilised to improve the predictions made in Chapter 2. The iterative deep learning technique is designed to alleviate some of the problems of solving problems with degenerate solution spaces and thus could be used.
- Additional experimental data, particular those that could provide a reference intensity for the measured spectra such as a Faraday cup or gas phase measurements, could also reduce the degenerate nature of the problem.
- In Chapter 3, improvements were made to the Monte Carlo simulation to better reflect the experimental noise in the measurements and the true dimensions of the experimental setup. Despite this, it is important that the cause for the discrepancies observed between the measured and simulated data are identified and accounted for in the simulation. While these might make minimal improvements to the predictions made, it would be informative to replicate the procedure with the improved simulation.

6.2.2 Iterative deep learning technique

The iterative deep learning technique presented in Chapter 4 leaves several open questions and opportunities to explore in future investigations.

- The iterative deep learning procedure presented was demonstrated using only methane as a case study due to computational limitations. While methane is an optimal case study for this method, extensive benchmarking of the network across multiple test cases would provide valuable insights into its limitations and provide a robust foundation for its application to new targets.
- In its application to HFO1234ze(E) in Chapter 5, we used only a select few mixture ratios and pressures as inputs into the network. One reason for this was computational efficiency, but another was that the network performance would degrade with increasing inputs. This could be due to experimental inconsistencies or the network being unable to appropriately prioritise features within the input array. Several techniques could be implemented to improve this so that all available data can be utilised:
  - The transport data could be parameterised by an appropriate function
  - The use of ‘attention’ type network architectures could be investigated so that the network ‘learns’ the important features of the input.
  - A different activation function for the input layer could potentially assist the network in discriminating between inputs.
  - Random sampling of transport mixture ratios and pressures between iterations could improve the generality of the regression.

- The inclusion of convolutional network layers and other deep learning frameworks could reveal additional improvements to the procedure.

- Genetic algorithms may be a viable alternative to the traditional deep learning approach.

- In the work presented here, we assume knowledge of the energy loss thresholds. This is not strictly necessary for the network. However, including the prediction of thresholds would introduce substantial degeneracy in the training data. Some options include:

  - Restricting the network to effective thresholds that are limited to certain energy regions. For example, an energy loss processes for each of rotation, vibration, excitation and dissociation would make a logical first step.

  - Starting with fewer threshold processes and splitting or adding processes according to some random and/or deterministic criteria at subsequent iterations. This would be similar to a genetic algorithm.

- In the work of Jetly *et. al.* [105], dropout was used to approximate the uncertainty of the network. This, or other techniques like mixture density networks or Bayesian networks, could be used in conjunction with the iterative technique to provide an additional constraint to the training data of subsequent iterations. An attempt was made to include dropout for this purpose, which showed some promise, but this work was not completed.

The development of a self-consistent and complete set of cross sections for HFO1234ze(E) requires further research to answer the following:

- In this work, we restricted the iterative deep learning technique to vibrational threshold energies determined from infra-red spectroscopy. There remains some uncertainty electronic excitation and dissociation processes however. Density functional theory was used by Eguž *et al.* [245] to determine the first electron excitation energy but its accuracy and whether other processes might exist is unclear. An attempt was made to include an excitation process between 5 and 12 eV but it was difficult to determine the improvements offered by its inclusion due to the significant computational burden of the technique.

- Due to the number of similar vibrational processes, future work could be restricted to effective cross sections to reduce the dimension and degeneracy of the fit if the accuracy of threshold energies were not important to the potential application of this cross section set.

- Mixture data with Ar and N_2 were not included here. For Ar, a cross section set that replicates the pure Ar transport data from the ETHZ group could resolve the difficulties encountered in this work using that data. The same could be said for N_2, SF_6 and CO_2 if indeed there are systematic difference in the transport data produced between different

experiments. For N_2, a full set including its rotation cross sections was not obtained for this work.

In addition to the research questions outlined above, it is useful to note that during this work, an ecosystem of packages was developed using the Julia programming language. The Monte Carlo simulation software, the Boltzmann solver and the deep learning code were developed as packages with the goal of seamless integration of data structures between each package. Every attempt was made to ensure each package is flexible and general in nature. This ecosystem provides a powerful engine for electron and positron transport problems. The inclusion of packages that interpret raw experimental data from experiments such as the pulsed Townsend experiment and fluid simulation packages holds great potential for numerous future applications. The publication of these packages as open source software would be beneficial to increase the reproducibility of this and future work.

Bibliography

[1] P. W. Stokes, M. J. E. Casey, D. G. Cocks, J. de Urquijo, G. García, M. J. Brunger, R. D. White, Self-consistent electron–THF cross sections derived using data-driven swarm analysis with a neural network model, Plasma Sources Science and Technology 29 (10) (2020) 105008. doi:10.1088/1361-6595/abb4f6.

[2] D. L. Muccignat, P. W. Stokes, D. G. Cocks, J. R. Gascooke, D. B. Jones, M. J. Brunger, R. D. White, Simulating the Feasibility of Using Liquid Micro-Jets for Determining Electron–Liquid Scattering Cross-Sections, International Journal of Molecular Sciences 23 (6) (2022) 3354. doi:10.3390/ijms23063354.

[3] D. L. Muccignat, G. G. Boyle, N. A. Garland, P. W. Stokes, R. D. White, An iterative deep learning procedure for determining electron scattering cross-sections from transport coefficients, Machine Learning: Science and Technology 5 (1) (2024) 015047. doi:10.1088/2632-2153/ad2fed.

[4] N. A. Garland, D. L. Muccignat, G. J. Boyle, R. D. White, Robust approximation rules for critical electric field of dielectric gas mixtures, Journal of Physics D: Applied Physics (2024). doi:10.1088/1361-6463/ad2dbc.

[5] L. Campbell, D. L. Muccignat, M. J. Brunger, Inclusion of Electron Interactions by Rate Equations in Chemical Models, Atoms 10 (2) (2022) 62. doi:10.3390/atoms10020062.

[6] C. G. N. Lee, K. J. Kanarik, R. A. Gottscho, The grand challenges of plasma etching: A manufacturing perspective, Journal of Physics D: Applied Physics 47 (27) (2014) 273001. doi:10.1088/0022-3727/47/27/273001.

[7] D. G. Williams, P. C., Linear Accelerators for Radiation Therapy, 2nd Edition, CRC Press, Boca Raton, 2017. doi:10.1201/9780429246562.

[8] G. Fridman, G. Friedman, A. Gutsol, A. B. Shekhter, V. N. Vasilets, A. Fridman, Applied Plasma Medicine, Plasma Processes and Polymers 5 (6) (2008) 503–533. doi:10.1002/ppap.200700154.

[9] M. G. Kong, G. Kroesen, G. Morfill, T. Nosenko, T. Shimizu, J. Van Dijk, J. L. Zimmermann, Plasma medicine: An introductory review, New Journal of Physics 11 (11) (2009) 115012. doi:10.1088/1367-2630/11/11/115012.

[10] S. Samukawa, M. Hori, S. Rauf, K. Tachibana, P. Bruggeman, G. Kroesen, J. C. Whitehead, A. B. Murphy, A. F. Gutsol, S. Starikovskaia, et al., The 2012 plasma roadmap, Journal of Physics D: Applied Physics 45 (2012) 253001. doi:10.1088/0022-3727/45/25/253001.

[11] I. Adamovich, S. D. Baalrud, A. Bogaerts, P. J. Bruggeman, M. Cappelli, V. Colombo, U. Czarnetzki, U. Ebert, J. G. Eden, P. Favia, D. B. Graves, S. Hamaguchi, G. Hieftje, M. Hori, I. D. Kaganovich, U. Kortshagen, M. J. Kushner, N. J. Mason, S. Mazouffre, S. M. Thagard, H.-R. Metelmann, A. Mizuno, E. Moreau, A. B. Murphy, B. A. Niemira, G. S. Oehrlein, Z. L. Petrovic, L. C. Pitchford, Y.-K. Pu, S. Rauf, O. Sakai, S. Samukawa, S. Starikovskaia, J. Tennyson, K. Terashima, M. M. Turner, M. C. M. Van De Sanden, A. Vardelle, The 2017 Plasma Roadmap: Low temperature plasma science and technology, Journal of Physics D: Applied Physics 50 (32) (2017) 323001. doi:10.1088/1361-6463/aa76f5.

[12] M. A. Lieberman, A. J. Lichtenberg, Principles of Plasma Discharges and Materials Processing, John Wiley & Sons, 2005.

[13] P. J. Bruggeman, M. J. Kushner, B. R. Locke, J. G. E. Gardeniers, W. G. Graham, D. B. Graves, R. C. H. M. Hofman-Caris, D. Maric, J. P. Reid, E. Ceriani, D. F. Rivas, J. E. Foster, S. C. Garrick, Y. Gorbanev, S. Hamaguchi, F. Iza, H. Jablonowski, E. Klimova, J. Kolb, F. Krcma, P. Lukes, Z. Machala, I. Marinov, D. Mariotti, S. M. Thagard, D. Minakata, E. C. Neyts, J. Pawlat, Z. L. Petrovic, R. Pflieger, S. Reuter, D. C. Schram, S. Schröter, M. Shiraiwa, B. Tarabová, P. A. Tsai, J. R. R. Verlet, T. von Woedtke, K. R. Wilson, K. Yasui, G. Zvereva, Plasma–liquid interactions: A review and roadmap, Plasma Sources Science and Technology 25 (5) (2016) 053002. doi:10.1088/0963-0252/25/5/053002.

[14] A. D. Lindsay, D. B. Graves, S. C. Shannon, Fully coupled simulation of the plasma liquid interface and interfacial coefficient effects, Journal of Physics D: Applied Physics 49 (23) (2016) 235204. doi:10.1088/0022-3727/49/23/235204.

[15] P. Rumbach, D. M. Bartels, R. M. Sankaran, D. B. Go, The solvation of electrons by an atmospheric-pressure plasma, Nature Communications 6 (1) (2015) 7248. doi:10.1038/ncomms8248.

[16] P. Rumbach, D. M. Bartels, R. M. Sankaran, D. B. Go, The effect of air on solvated electron chemistry at a plasma/liquid interface, Journal of Physics D: Applied Physics 48 (42) (2015) 424001. doi:10.1088/0022-3727/48/42/424001.

[17] R. Gopalakrishnan, E. Kawamura, A. J. Lichtenberg, M. A. Lieberman, D. B. Graves, Solvated electrons at the atmospheric pressure plasma–water anodic interface, Journal of Physics D: Applied Physics 49 (29) (2016) 295205. doi:10.1088/0022-3727/49/29/295205.

[18] P. Rumbach, D. M. Bartels, D. B. Go, The penetration and concentration of solvated electrons and hydroxyl radicals at a plasma-liquid interface, Plasma Sources Science and Technology 27 (11) (2018) 115013. doi:10.1088/1361-6595/aaed07.

[19] D. C. Martin, D. M. Bartels, P. Rumbach, D. B. Go, Experimental confirmation of solvated electron concentration and penetration scaling at a plasma–liquid interface, Plasma Sources Science and Technology 30 (3) (2021) 03LT01. doi:10.1088/1361-6595/abe11c.

[20] S. A. Norberg, W. Tian, E. Johnsen, M. J. Kushner, Atmospheric pressure plasma jets interacting with liquid covered tissue: Touching and not-touching the liquid, Journal of Physics D: Applied Physics 47 (2014) 475203. doi:10.1088/0022-3727/47/47/475203.

[21] N. Y. Babaeva, W. Tian, M. J. Kushner, The interaction between plasma filaments in dielectric barrier discharges and liquid covered wounds: Electric fields delivered to model platelets and cells, Journal of Physics D: Applied Physics 47 (23) (2014) 235201. doi:10.1088/0022-3727/47/23/235201.

[22] M. Michaud, A. Wen, L. Sanche, Cross sections for low-energy (1-100 eV) electron elastic and inelastic scattering in amorphous ice, Radiation Research 159 (1) (2003) 3–22. doi:10.1667/0033-7587(2003)159[0003:csflee]2.0.co;2.

[23] B. Boudaïffa, D. Hunting, P. Cloutier, M. A. Huels, L. Sanche, Induction of single- and double-strand breaks in plasmid DNA by 100–1500 eV electrons, International Journal of Radiation Biology 76 (9) (2000) 1209–1221. doi:10.1080/09553000050134447.

[24] G. J. Boyle, R. P. McEachran, D. G. Cocks, R. D. White, Electron scattering and transport in liquid argon, The Journal of Chemical Physics 142 (15) (2015) 154507. doi:10.1063/1.4917258.

[25] G. J. Boyle, R. P. McEachran, D. G. Cocks, M. J. Brunger, S. J. Buckman, S. Dujko, R. D. White, Ab initio electon scattering cross-sections and transport in liquid xenon, Journal of Physics D: Applied Physics 49 (35) (2016) 355201. doi:10.1088/0022-3727/49/35/355201.

[26] M. Faubel, S. Schlemmer, J. P. Toennies, A molecular beam study of the evaporation of water from a liquid jet, Zeitschrift für Physik D: Atoms, Molecules and Clusters 10 (2-3) (1988) 269–277. doi:10.1007/bf01384861.

[27] D. W. Swan, Drift velocity of electrons in liquid argon, and the influence of molecular impurities, Proceedings of the Physical Society 83 (4) (1964) 659. doi:10.1088/0370-1328/83/4/319.

[28] K. Yoshino, U. Sowada, W. F. Schmidt, Effect of molecular solutes on the electron drift velocity in liquid Ar, Kr, and Xe, Physical Review A 14 (1) (1976) 438–444. doi:10.1103/PhysRevA.14.438.

[29] H. Schnyders, S. A. Rice, L. Meyer, Electron Drift Velocities in Liquefied Argon and Krypton at Low Electric Field Strengths, Physical Review 150 (1) (1966) 127–145. doi:10.1103/PhysRev.150.127.

[30] S. Kubota, T. Takahashi, J.-z. Ruan(gen), Hot Electron Relaxation in Solid and Liquid Argon, Krypton and Xenon, Journal of the Physical Society of Japan 51 (10) (1982) 3274–3277. doi:10.1143/JPSJ.51.3274.

[31] M. Faubel, B. Steiner, J. P. Toennies, Photoelectron spectroscopy of liquid water, some alcohols, and pure nonane in free micro jets, The Journal of Chemical Physics 106 (22) (1997) 9013–9031. doi:10.1063/1.474034.

[32] R. Weber, B. Winter, P. M. Schmidt, W. Widdra, I. V. Hertel, M. Dittmar, M. Faubel, Photoemission from Aqueous Alkali-Metal-Iodide Salt Solutions Using EUV Synchrotron Radiation, The Journal of Physical Chemistry 108 (15) (2004) 4729–4736. doi:10.1021/jp030776x.

[33] B. Winter, M. Faubel, Photoemission from Liquid Aqueous Solutions, Chemical Reviews 106 (4) (2006) 1176–1211. doi:10.1021/cr040381p.

[34] D. Ogletree, H. Bluhm, E. L. D. Hebenstreit, M. Salmeron, Photoelectron spectroscopy under ambient pressure and temperature conditions, Nuclear Instruments & Methods in Physics Research Section A-accelerators Spectrometers Detectors and Associated Equipment 601 (2009) 151–160. doi:10.1016/J.NIMA.2008.12.155.

[35] N. Ottosson, M. Faubel, S. E. Bradforth, P. Jungwirth, B. Winter, Photoelectron spectroscopy of liquid water and aqueous solution: Electron effective attenuation lengths and emission-angle anisotropy, Journal of Electron Spectroscopy and Related Phenomena 177 (2-3) (2009) 60–70. doi:10.1016/j.elspec.2009.08.007.

[36] A. Shreve, T. A. Yen, D. Neumark, Photoelectron spectroscopy of hydrated electrons, Chemical Physics Letters 493 (2010) 216–219. doi:10.1016/J.CPLETT.2010.05.059.

[37] A. Lübcke, F. Buchner, N. Heine, I. Hertel, T. Schultz, Time-resolved photoelectron spectroscopy of solvated electrons in aqueous NaI solution., Physical chemistry chemical physics : PCCP 12 43 (2010) 14629–34. doi:10.1039/c0cp00847h.

[38] R. Seidel, S. Thürmer, B. Winter, Photoelectron Spectroscopy Meets Aqueous Solution: Studies from a Vacuum Liquid Microjet, The Journal of Physical Chemistry Letters 2 (6) (2011) 633–641. doi:10.1021/jz101636y.

[39] S. Thürmer, R. Seidel, M. Faubel, W. Eberhardt, J. C. Hemminger, S. E. Bradforth, B. Winter, Photoelectron Angular Distributions from Liquid Water: Effects of Electron Scattering, Physical Review Letters 111 (17) (2013) 173005. doi:10.1103/PhysRevLett.111.173005.

[40] A. Beroual, A. M. Haddad, Recent Advances in the Quest for a New Insulation Gas with a Low Impact on the Environment to Replace Sulfur Hexafluoride (SF6) Gas in High-Voltage Power Network Applications, Energies 10 (8) (2017) 1216. doi:10.3390/en10081216.

[41] M. Rabie, C. M. Franck, Assessment of Eco-friendly Gases for Electrical Insulation to Replace the Most Potent Industrial Greenhouse Gas SF_6, Environmental Science & Technology 52 (2) (2018) 369–380. doi:10.1021/acs.est.7b03465.

[42] M. Koch, C. M. Franck, High voltage insulation properties of HFO1234ze, IEEE Transactions on Dielectrics and Electrical Insulation 22 (6) (2015) 3260–3268. doi:10.1109/tdei.2015.005118.

[43] A. Hosl, J. Pachin, E. Eguz, A. Chachereau, C. M. Franck, Positive synergy of SF_6 and HFO1234ze(E), IEEE Transactions on Dielectrics and Electrical Insulation 27 (1) (2020) 322–324. doi:10.1109/tdei.2019.008406.

[44] M. J. Brunger, S. J. Buckman, Electron–molecule scattering cross-sections. I. Experimental techniques and data for diatomic molecules, Physics Reports 357 (3-5) (2002) 215–458. doi:10.1016/s0370-1573(01)00032-1.

[45] L. S. Frost, A. V. Phelps, Rotational Excitation and Momentum Transfer Cross Sections for Electrons in H_2 and N_2 from Transport Coefficients, Physical Review 127 (5) (1962) 1621–1633. doi:10.1103/PhysRev.127.1621.

[46] W. L. Morgan, Use of numerical optimization algorithms to obtain cross sections from electron swarm data, Physical Review A 44 (3) (1991) 1677–1681. doi:10.1103/physreva.44.1677.

[47] P. W. Stokes, D. G. Cocks, M. J. Brunger, R. D. White, Determining cross sections from transport coefficients using deep neural networks, Plasma Sources Science and Technology 29 (5) (2020) 055009. doi:10.1088/1361-6595/ab85b6.

[48] L. Boltzmann, Weitere studien über das wärmegleichgewicht unter gasmolekülen, in: Kinetische Theorie II: Irreversible Prozesse Einführung Und Originaltexte, Vieweg+Teubner Verlag, Wiesbaden, 1970, pp. 115–225. doi:10.1007/978-3-322-84986-1_3.

[49] C. S. Wang Chang, G. E. Uhlenbeck, J. de Boer, The heat conductivity and viscosity of polyatomic gases, in: Studies of Statistical Mechanics, Vol. 2, NY: Wiley, New York, 1962, pp. 241–268.

[50] R. Robson, R. White, M. Hildebrandt, Fundamentals of Charged Particle Transport in Gases and Condensed Matter, 2017. doi:10.4324/9781315120935.

[51] T. Makabe, R. White, Expression for momentum-transfer scattering in inelastic collisions in electron transport in a collisional plasma, Journal of Physics D: Applied Physics 48 (48) (2015) 485205. doi:10.1088/0022-3727/48/48/485205.

[52] S. Pancheshnyi, S. Biagi, M. C. Bordage, G. J. Hagelaar, W. L. Morgan, A. V. Phelps, L. C. Pitchford, The LXCat project: Electron scattering cross sections and swarm parameters for low temperature plasma modeling, Chemical Physics 398 (1) (2012) 148–153. doi:10.1016/j.chemphys.2011.04.020.

[53] P. Delahay, Quasi-Free Electrons in Polar Liquids, in: J. Jortner, N. R. Kestner (Eds.), Electrons in Fluids: The Nature of Metal—Ammonia Solutions, Springer, Berlin, Heidelberg, 1973, pp. 131–138. doi:10.1007/978-3-642-61962-5_9.

[54] A. Chachereau, M. Rabie, C. M. Franck, Electron swarm parameters of the hydrofluoroolefine HFO1234ze, Plasma Sources Science and Technology 25 (4) (2016) 045005. doi:10.1088/0963-0252/25/4/045005.

[55] J. de Urquijo, O. González-Magaña, E. Basurto, A. M. Juárez, Two- and three-body attachment, electron transport and ionisation in water-air mixtures, Journal of Physics D: Applied Physics 57 (12) (2023) 125205. doi:10.1088/1361-6463/ad164a.

[56] R. D. White, D. Cocks, G. Boyle, M. Casey, N. Garland, D. Konovalov, B. Philippa, P. Stokes, J. de Urquijo, O. González-Magaña, R. P. McEachran, S. J. Buckman, M. J.

Brunger, G. Garcia, S. Dujko, Z. L. Petrovic, Electron transport in biomolecular gaseous and liquid systems: Theory, experiment and self-consistent cross-sections, Plasma Sources Science and Technology 27 (5) (2018) 053001. doi:10.1088/1361-6595/aabdd7.

[57] G. Boyle, W. Tattersall, D. Cocks, R. McEachran, R. White, A multi-term solution of the space-time Boltzmann equation for electrons in gases and liquids, Plasma Sources Science and Technology 26 (2017). doi:10.1088/1361-6595/aa51ef.

[58] Z. L. Petrović, D. Marić, M. Savić, S. Marjanović, S. Dujko, G. Malović, Using Swarm Models as an Exact Representation of Ionized Gases, Plasma Processes and Polymers 14 (1-2) (2017) 1600124. doi:10.1002/ppap.201600124.

[59] J. C. Stephens, A multi-term, multi-harmonic Boltzmann equation model for kinetic behavior in intense microwave and terahertz excited low temperature plasmas, Physics of Plasmas 25 (10) (2018) 103502. doi:10.1063/1.5047809.

[60] M. Flynn, A. Neuber, J. Stephens, Benchmarking the calculation of electrically insulating properties of complex gas mixtures using a multi-term Boltzmann equation model, Journal of Physics D: Applied Physics 55 (1) (2021) 015201. doi:10.1088/1361-6463/ac29e7.

[61] G. J. Boyle, N. A. Garland, R. P. McEachran, K. A. Mirihana, R. E. Robson, J. P. Sullivan, R. D. White, Electron scattering and transport in simple liquid mixtures, Journal of Physics B: Atomic, Molecular and Optical Physics 57 (1) (2024) 015202. doi:10.1088/1361-6455/ad1d35.

[62] N. Metropolis, A. W. Rosenbluth, M. N. Rosenbluth, A. H. Teller, E. Teller, Equation of State Calculations by Fast Computing Machines, The Journal of Chemical Physics 21 (6) (1953) 1087–1092. doi:10.1063/1.1699114.

[63] B. J. Alder, T. E. Wainwright, Studies in Molecular Dynamics. I. General Method, The Journal of Chemical Physics 31 (2) (1959) 459–466. doi:10.1063/1.1730376.

[64] C. Champion, C. Le Loirec, B. Stosic, EPOTRAN: A full-differential Monte Carlo code for electron and positron transport in liquid and gaseous water, International Journal of Radiation Biology 88 (2012) 54–61. doi:10.3109/09553002.2011.641451.

[65] Z. L. Petrović, S. Marjanović, S. Marjanovic, S. Dujko, A. Bankovic, G. Malović, S. Buckman, G. García, R. D. White, M. J. Brunger, On the use of Monte Carlo simulations to model transport of positrons in gases and liquids, Applied Radiation and Isotopes 83 (2014) 148–154. doi:10.1016/j.apradiso.2013.01.010.

[66] W. Tattersall, Positron cross sections and transport in water (2016). doi:10.25911/5d7392d196252.

[67] S. Dujko, D. Bošnjaković, M. Vass, P. Hartmann, I. Korolov, N. R. Pinhão, D. Loffhagen, Z. Donkó, Scanning drift tube measurements and kinetic studies of electron transport in CO, Plasma Sources Science and Technology 32 (2) (2023) 025014. doi:10.1088/1361-6595/acbc96.

[68] M. Brennan, Optimization of Monte Carlo codes using null collision techniques for experimental simulation at low E/N, IEEE Transactions on Plasma Science 19 (2) (1991) 256–261. doi:10.1109/27.106822.

[69] D. Tskhakaya, K. Matyash, R. Schneider, F. Taccogna, The Particle-In-Cell Method, Contributions to Plasma Physics 47 (8-9) (2007) 563–594. doi:10.1002/ctpp.200710072.

[70] O. Buneman, Dissipation of Currents in Ionized Media, Physical Review 115 (3) (1959) 503–517. doi:10.1103/PhysRev.115.503.

[71] J. Dawson, One-Dimensional Plasma Model, The Physics of Fluids 5 (4) (1962) 445–459. doi:10.1063/1.1706638.

[72] L. C. Pitchford, L. L. Alves, K. Bartschat, S. F. Biagi, M. C. Bordage, I. Bray, C. E. Brion, M. J. Brunger, L. Campbell, A. Chachereau, B. Chaudhury, L. G. Christophorou, E. Carbone, N. A. Dyatko, C. M. Franck, D. V. Fursa, R. K. Gangwar, V. Guerra, P. Haefliger, G. J. M. Hagelaar, A. Hoesl, Y. Itikawa, I. V. Kochetov, R. P. McEachran, W. L. Morgan, A. P. Napartovich, V. Puech, M. Rabie, L. Sharma, R. Srivastava, A. D. Stauffer, J. Tennyson, J. de Urquijo, J. van Dijk, L. A. Viehland, M. C. Zammit, O. Zatsarinny, S. Pancheshnyi, LXCat: An Open-Access, Web-Based Platform for Data Needed for Modeling Low Temperature Plasmas, Plasma Processes and Polymers 14 (1-2) (2017) 1600098. doi:10.1002/ppap.201600098.

[73] E. Carbone, W. Graef, G. Hagelaar, D. Boer, M. M. Hopkins, J. C. Stephens, B. T. Yee, S. Pancheshnyi, J. van Dijk, L. Pitchford, Data Needs for Modeling Low-Temperature Non-Equilibrium Plasmas: The LXCat Project, History, Perspectives and a Tutorial, Atoms 9 (1) (2021) 16. doi:10.3390/atoms9010016.

[74] M. C. Zammit, D. V. Fursa, J. S. Savage, I. Bray, Electron and positron molecule scattering: Development of the molecular convergent close-coupling method, Journal of Physics B: Atomic, Molecular and Optical Physics 50 (12) (2017) 123001. doi:10.1088/1361-6455/aa6e74.

[75] M. C. Zammit, D. V. Fursa, I. Bray, Electron scattering from the molecular hydrogen ion and its isotopologues, Physical Review A 90 (2) (2014) 022711. doi:10.1103/PhysRevA.90.022711.

[76] J. C. Nickel, P. W. Zetner, G. Shen, S. Trajmar, Principles and procedures for determining absolute differential electron-molecule (atom) scattering cross sections, Journal of Physics E: Scientific Instruments 22 (9) (1989) 730. doi:10.1088/0022-3735/22/9/010.

[77] S. Trajmar, J. W. McConkey, Benchmark Measurements of Cross Sections for Electron Collisions: Analysis of Scattered Electrons, in: M. Inokuti (Ed.), Advances In Atomic, Molecular, and Optical Physics, Vol. 33 of Cross Section Data, Academic Press, 1994, pp. 63–96. doi:10.1016/S1049-250X(08)60033-6.

[78] S. J. Buckman, R. J. Gulley, M. Moghbelalhossein, S. J. Bennett, Spatial profiles of effusive molecular beams and their dependence on gas species, Measurement Science and Technology 4 (10) (1993) 1143. doi:2011050110102800.

[79] M. J. Brunger, S. J. Buckman, D. S. Newman, Low Energy Electron Scattering From H_2, Australian Journal of Physics 43 (5) (1990) 665–682. doi:10.1071/ph900665.

[80] A. Lun, X. J. Chen, L. J. Allen, K. Amos, Inversion of electron-water elastic-scattering data, Physical Review A 49 (5) (1994) 3788–3798. doi:10.1103/PhysRevA.49.3788.

[81] D. R. Lun, X. J. Chen, L. J. Allen, K. Amos, Inversion of He-Ne elastic-scattering data, Physical Review A 50 (5) (1994) 4025–4030. doi:10.1103/PhysRevA.50.4025.

[82] W. Sun, M. A. Morrison, W. A. Isaacs, W. K. Trail, D. T. Alle, R. J. Gulley, M. J. Brennan, S. J. Buckman, Detailed theoretical and experimental analysis of low-energy electron-$_2$ scattering, Physical Review A 52 (2) (1995) 1229–1256. doi:10.1103/PhysRevA.52.1229.

[83] S. J. Buckman, B. Lohmann, Low-energy total cross section measurements for electron scattering from helium and argon, Journal of Physics B: Atomic and Molecular Physics 19 (16) (1986) 2547. doi:10.1088/0022-3700/19/16/013.

[84] S. Trajmar, J. C. Nickel, Cross-Section Measurements for Electron Impact on Excited Atomic Species, in: D. Bates, B. Bederson (Eds.), Advances In Atomic, Molecular, and Optical Physics, Vol. 30, Academic Press, 1992, pp. 45–103. doi:10.1016/S1049-250X(08)60173-1.

[85] S. Trajmar, D. C. Cartwright, W. Williams, Differential and Integral Cross Sections for the Electron-Impact Excitation of the $a^1\Delta_g$ and $b^1\Sigma_G^+$ States of O_2, Physical Review A 4 (4) (1971) 1482–1492. doi:10.1103/PhysRevA.4.1482.

[86] H. Siegbahn, K. Siegbahn, ESCA applied to liquids, Journal of Electron Spectroscopy and Related Phenomena 2 (3) (1973) 319–325. doi:10.1016/0368-2048(73)80023-4.

[87] H. Siegbahn, S. Svensson, M. Lundholm, A new method for ESCA studies of liquid-phase samples, Journal of Electron Spectroscopy and Related Phenomena 24 (1981) 205–213. doi:10.1016/0368-2048(81)80007-2.

[88] D. Starr, H. Bluhm, Z. Liu, A. Knop-Gericke, M. Hävecker, Application of Ambient-Pressure X-ray Photoelectron Spectroscopy for the In-situ Investigation of Heterogeneous Catalytic Reactions (2013). doi:10.1002/9781118355923.CH12.

[89] K. R. Wilson, R. Schaller, D. T. Co, R. Saykally, B. Rude, T. Catalano, J. Bozek, Surface relaxation in liquid water and methanol studied by x-ray absorption spectroscopy, Journal of Chemical Physics 117 (2002) 7738–7744. doi:10.1063/1.1508364.

[90] M. J. E. Casey, P. W. Stokes, D. Cocks, D. Bošnjaković, I. Simonovic, M. Brunger, M. J. Brunger, S. Dujko, Z. Lj. Petrović, Z. L. Petrović, R. Robson, R. D. White, Foundations and interpretations of the pulsed-Townsend experiment, Plasma Sources Science and Technology 30 (3) (2021) 035017. doi:10.1088/1361-6595/abe729.

[91] E. W. McDaniel, M. R. C. McDowell, Case Studies in Atomic Collision Physics, Elsevier, 1972.

[92] L. G. H. Huxley, The Diffusion and Drift of Electrons in Gases, Wiley, New York,.

[93] H. Massey, E. H. S. Burhop, H. B. Gilbody (Eds.), Electronic and Ionic Impact Phenomena., 2nd Edition, Clarendon Press., Oxford, 1974.

[94] Front Matter, in: L. G. Christophorou (Ed.), Electron–Molecule Interactions and Their Applications, Academic Press, 1984, p. iii. doi:10.1016/B978-0-12-174401-4.50001-8.

[95] M. Charlton, J. W. Humberston, Positron Physics, Cambridge Monographs on Atomic, Molecular and Chemical Physics, Cambridge University Press, Cambridge, 2000. doi:10.1017/CBO9780511535208.

[96] M. Charlton, Positron transport in gases, Journal of Physics: Conference Series 162 (1) (2009) 012003. doi:10.1088/1742-6596/162/1/012003.

[97] P. Haefliger, C. M. Franck, Detailed precision and accuracy analysis of swarm parameters from a pulsed Townsend experiment, Review of Scientific Instruments 89 (2) (2018) 023114. doi:10.1063/1.5002762.

[98] M. J. Brunger, S. J. Buckman, K. Ratnavelu, Positron scattering from molecules: An experimental cross section compilation for positron transport studies and benchmarking theory, Journal of Physical and Chemical Reference Data 46 (2) (2017) 023102. doi:10.1063/1.4982827.

[99] H. F. Mayer, Über das Verhalten von Molekülen gegenüber freien langsamen Elektronen, Annalen der Physik 369 (5) (1921) 451–480. doi:10.1002/andp.19213690503.

[100] C. Ramsauer, Über den Wirkungsquerschnitt der Gasmoleküle gegenüber langsamen Elektronen, Annalen der Physik 369 (6) (1921) 513–540. doi:10.1002/andp.19213690603.

[101] J. S. Townsend, V. A. Bailey, The motion of electrons in argon, The London, Edinburgh, and Dublin Philosophical Magazine and Journal of Science 43 (255) (1922) 593–600. doi:10.1080/14786442208633916.

[102] A. G. Engelhardt, A. V. Phelps, Elastic and Inelastic Collision Cross Sections in Hydrogen and Deuterium from Transport Coefficients, Physical Review 131 (5) (1963) 2115–2128. doi:10.1103/physrev.131.2115.

[103] A. G. Engelhardt, A. V. Phelps, C. G. Risk, Determination of Momentum Transfer and Inelastic Collision Cross Sections for Electrons in Nitrogen Using Transport Coefficients, Physical Review 135 (6A) (1964) A1566–A1574. doi:10.1103/physrev.135.a1566.

[104] R. D. Hake, A. V. Phelps, Momentum-Transfer and Inelastic-Collision Cross Sections for Electrons in O_2, CO, and CO_2, Physical Review 158 (1) (1967) 70–84. doi:10.1103/physrev.158.70.

[105] V. Jetly, B. Chaudhury, Extracting electron scattering cross sections from swarm data using deep neural networks, Machine Learning: Science and Technology 2 (3) (2021) 035025. doi:10.1088/2632-2153/abf15a.

[106] P. W. Stokes, R. D. White, L. Campbell, M. J. Brunger, Toward a complete and comprehensive cross section database for electron scattering from NO using machine learning, The Journal of Chemical Physics 155 (8) (2021) 084305. doi:10.1063/5.0064376.

[107] P. W. Stokes, S. P. Foster, M. J. E. Casey, D. G. Cocks, O. González-Magaña, J. de Urquijo, G. García, M. J. Brunger, R. D. White, An improved set of electron-THFA cross sections refined through a neural network-based analysis of swarm data, The Journal of Chemical Physics 154 (8) (2021) 084306. doi:10.1063/5.0043759.

[108] Advanced Microfluidic Systems GmbH, https://admisys-gmbh.com/.

[109] D. Muccignat, Monte Carlo simulation of non-equilibrium electron-liquid transport, Honours Thesis, James Cook University (2018).

[110] T. Shimizu, B. Steffes, R. Pompl, F. Jamitzky, W. Bunk, K. Ramrath, M. Georgi, W. Stolz, H.-U. Schmidt, T. Urayama, S. Fujii, G. E. Morfill, Characterization of Microwave Plasma Torch for Decontamination, Plasma Processes and Polymers 5 (6) (2008) 577–582. doi:10.1002/ppap.200800021.

[111] H. Tanaka, M. Mizuno, K. Ishikawa, K. Nakamura, H. Kajiyama, H. Kano, F. Kikkawa, M. Hori, Plasma-Activated Medium Selectively Kills Glioblastoma Brain Tumor Cells by Down-Regulating a Survival Signaling Molecule, AKT Kinase, Plasma Medicine 1 (3-4) (2011) 265–277. doi:10.1615/PlasmaMed.2012006275.

[112] D. W. Taylor, M. Petrera, M. Hendry, J. S. Theodoropoulos, A Systematic Review of the Use of Platelet-Rich Plasma in Sports Medicine as a New Treatment for Tendon and Ligament Injuries, Clinical Journal of Sport Medicine 21 (4) (2011) 344–352. doi:10.1097/JSM.0b013e31821d0f65.

[113] J. Schlegel, J. Köritzer, V. Boxhammer, Plasma in cancer treatment, Clinical Plasma Medicine 1 (2013) 2–7. doi:10.1016/j.cpme.2013.08.001.

[114] M. Keidar, Plasma for cancer treatment, Plasma Sources Science and Technology 24 (3) (2015) 033001. doi:10.1088/0963-0252/24/3/033001.

[115] S. Bekeschus, A. Schmidt, K.-D. Weltmann, T. Von Woedtke, The plasma jet kINPen – A powerful tool for wound healing, Clinical Plasma Medicine 4 (1) (2016) 19–28. doi:10.1016/j.cpme.2016.01.001.

[116] T. Bernhardt, M. L. Semmler, M. Schäfer, S. Bekeschus, S. Emmert, L. Boeckmann, Plasma Medicine: Applications of Cold Atmospheric Pressure Plasma in Dermatology, Oxidative Medicine and Cellular Longevity 2019 (2019) 1–10. doi:10.1155/2019/3873928.

[117] T. Von Woedtke, A. Schmidt, S. Bekeschus, K. Wende, K.-D. Weltmann, Plasma Medicine: A Field of Applied Redox Biology, In Vivo 33 (4) (2019) 1011–1026. doi:10.21873/invivo.11570.

[118] Z. Liu, Z. Liu, W. Cai, Wei Cai, Z.-Q. J. Xu, Zhi-Qin John Xu, Multi-scale Deep Neural Network (MscaleDNN) for Solving Poisson-Boltzmann Equation in Complex Domains, Communications in Computational Physics (Jul. 2020). doi:10.4208/cicp.oa-2020-0179.

[119] J. Meesungnoen, J.-P. Jay-Gerin, A. Filali-Mouhim, S. Mankhetkorn, Low-Energy Electron Penetration Range in Liquid Water, Radiation Research 158 (5) (2002) 657–660. doi:10.1667/0033-7587(2002)158[0657:LEEPRI]2.0.CO;2.

[120] M. Faubel, B. Steiner, Photoelectron Spectroscopy at Liquid Water Surfaces, in: Linking the Gaseous and Condensed Phases of Matter, Springer US, 1994, pp. 517–523.

[121] M. Faubel, B. Steiner, J. P. Toennies, Measurement of HeI photoelectron spectra of liquid water, formamide and ethylene glycol in fast-flowing microjets, Journal of Electron Spectroscopy and Related Phenomena 95 (2-3) (1998) 159–169. doi:10.1016/s0368-2048(98)00208-4.

[122] B. Winter, R. Weber, I. V. Hertel, M. Faubel, P. Jungwirth, E. C. Brown, S. E. Bradforth, Electron binding energies of aqueous alkali and halide ions: EUV photoelectron spectroscopy of liquid solutions and combined ab initio and molecular dynamics calculations, Journal of the American Chemical Society 127 (19) (2005) 7203–7214. doi:10.1021/ja042908l.

[123] H. Winter, J. Burgdörfer, J. Burgdörfer (Eds.), Slow Heavy-Particle Induced Electron Emission from Solid Surfaces, no. 225 in Springer Tracts in Modern Physics, Springer, Berlin Heidelberg New York, 2007.

[124] B. Winter, Liquid microjet for photoelectron spectroscopy, Nuclear Instruments and Methods in Physics Research Section A: Accelerators, Spectrometers, Detectors and Associated Equipment 601 (1-2) (2009) 139–150. doi:10.1016/j.nima.2008.12.108.

[125] M. A. Brown, A. B. Redondo, I. Jordan, N. Duyckaerts, M.-T. Lee, M. Ammann, F. Nolting, A. Kleibert, T. Huthwelker, J.-P. Mächler, M. Birrer, J. Honegger, R. Wetter, H. J. Wörner, J. A. Van Bokhoven, A new endstation at the Swiss Light Source for ultraviolet photoelectron spectroscopy, X-ray photoelectron spectroscopy, and X-ray absorption spectroscopy measurements of liquid solutions, Review of Scientific Instruments 84 (7) (2013) 073904. doi:10.1063/1.4812786.

[126] J. W. Riley, B. Wang, M. A. Parkes, H. H. Fielding, Design and characterization of a recirculating liquid-microjet photoelectron spectrometer for multiphoton ultraviolet photoelectron spectroscopy, Review of Scientific Instruments 90 (8) (2019) 083104. doi:10.1063/1.5099040.

[127] T. Buttersack, P. E. Mason, R. S. McMullen, T. Martinek, K. Brezina, D. Hein, H. Ali, C. Kolbeck, C. Schewe, S. Malerz, B. Winter, R. Seidel, O. Marsalek, P. Jungwirth, S. E. Bradforth, Valence and Core-Level X-ray Photoelectron Spectroscopy of a Liquid Ammonia Microjet, Journal of the American Chemical Society 141 (5) (2019) 1838–1841. doi:10.1021/jacs.8b10942.

[128] K. D. Mudryk, R. Seidel, B. Winter, I. Wilkinson, The electronic structure of the aqueous permanganate ion: Aqueous-phase energetics and molecular bonding studied using liquid

jet photoelectron spectroscopy, Physical Chemistry Chemical Physics 22 (36) (2020) 20311–20330. doi:10.1039/d0cp04033a.

[129] J. Nishitani, S. Karashima, C. W. West, T. Suzuki, Surface potential of liquid microjet investigated using extreme ultraviolet photoelectron spectroscopy, The Journal of Chemical Physics 152 (14) (2020) 144503. doi:10.1063/5.0005930.

[130] R. W. Crompton, Benchmark measurements of cross sections for electron collisions: Electron swarm methods, Advances in Atomic, Molecular, and Optical Physics 33 (1994) 97–148. doi:10.1016/S1049-250X(08)60034-8.

[131] Z. L. Petrović, M. Šuvakov, Ž. Nikitović, S. Dujko, O. Šašić, J. Jovanović, G. Malović, V. Stojanović, Kinetic phenomena in charged particle transport in gases, swarm parameters and cross section data, Plasma Sources Science and Technology 16 (2007) S1. doi:10.1088/0963-0252/16/1/S01.

[132] Z. L. Petrović, A. Banković, S. Dujko, S. Marjanović, G. Malović, J. P. Sullivan, S. J. Buckman, Data for modeling of positron collisions and transport in gases, AIP Conference Proceedings 1545 (2013) 115–131. doi:10.1063/1.4815846.

[133] K. F. Ness, R. E. Robson, Transport properties of electrons in water vapor, Physical Review A 38 (3) (1988) 1446–1456. doi:10.1103/PhysRevA.38.1446.

[134] M. Yousfi, M. D. Benabdessadok, Boltzmann equation analysis of electron-molecule collision cross sections in water vapor and ammonia, Journal of Applied Physics 80 (12) (1996) 6619–6630. doi:10.1063/1.363785.

[135] R. E. Robson, R. D. White, K. F. Ness, Transport coefficients for electrons in water vapor: Definition, measurement, and calculation, The Journal of Chemical Physics 134 (6) (2011) 064319. doi:10.1063/1.3544210.

[136] K. F. Ness, R. E. Robson, M. J. Brunger, R. D. White, Transport coefficients and cross sections for electrons in water vapour: Comparison of cross section sets using an improved Boltzmann equation solution, The Journal of Chemical Physics 136 (2) (2012) 024318. doi:10.1063/1.3675921.

[137] J. de Urquijo, E. Basurto, A. M. Juárez, K. F. Ness, R. E. Robson, M. J. Brunger, R. D. White, Electron drift velocities in He and water mixtures: Measurements and an assessment of the water vapour cross-section sets, The Journal of Chemical Physics 141 (1) (2014) 014308. doi:10.1063/1.4885357.

[138] M. J. E. Casey, J. de Urquijo, L. N. S. Loli, D. G. Cocks, G. J. Boyle, D. B. Jones, M. J. Brunger, R. D. White, Self-consistency of electron-THF cross sections using electron

swarm techniques, The Journal of Chemical Physics 147 (19) (2017) 195103. doi:10.1063/1.5004717.

[139] J. Nam, H. Yong, J. Hwang, J. Choi, Training an artificial neural network for recognizing electron collision patterns, Physics Letters A 387 (2021) 127005. doi:10.1016/j.physleta.2020.127005.

[140] W. J. Tattersall, D. G. Cocks, G. J. Boyle, S. J. Buckman, R. D. White, Monte Carlo study of coherent scattering effects of low-energy charged particle transport in Percus-Yevick liquids, Physical Review E (Statistical, Nonlinear, and Soft Matter Physics) 91 (4) (2015) 043304. doi:10.1103/PhysRevE.91.043304.

[141] R. Zahoor, G. Belšak, S. Bajt, B. Šarler, Simulation of liquid micro-jet in free expanding high-speed co-flowing gas streams, Microfluidics and Nanofluidics 22 (8) (2018) 1–20. doi:10.1007/s10404-018-2110-0.

[142] R. Zahoor, S. Bajt, B. Šarler, Influence of Gas Dynamic Virtual Nozzle Geometry on Micro-Jet Characteristics, International Journal of Multiphase Flow 104 (2018) 152–165. doi:10.1016/j.ijmultiphaseflow.2018.03.003.

[143] R. Zahoor, S. Bajt, B. Šarler, Numerical investigation on influence of focusing gas type on liquid micro-jet characteristics, International Journal of Hydromechatronics 1 (2) (2018) 222. doi:10.1504/ijhm.2018.092732.

[144] M. Ekimova, W. Quevedo, M. Faubel, P. Wernet, E. T. J. Nibbering, A liquid flatjet system for solution phase soft-x-ray spectroscopy, Structural Dynamics 2 (5) (2015) 054301. doi:10.1063/1.4928715.

[145] R. E. Grisenti, R. A. C. Fraga, N. Petridis, R. Dörner, J. Deppe, Cryogenic microjet for exploration of superfluidity in highly supercooled molecular hydrogen, Europhysics Letters (EPL) 73 (4) (2006) 540–546. doi:10.1209/epl/i2005-10433-3.

[146] J. B. Kim, S. Göde, S. H. Glenzer, Development of a cryogenic hydrogen microjet for high-intensity, high-repetition rate experiments, Review of Scientific Instruments 87 (11) (2016) 11E328. doi:10.1063/1.4961089.

[147] W. L. Holstein, M. R. Hammer, G. F. Metha, M. A. Buntine, Time-of-flight mass spectrometric detection of mono- and di-substituted benzenes at parts per million concentrations by way of liquid microjet injection and laser ionisation, International Journal of Mass Spectrometry 207 (1-2) (2001) 1–12. doi:10.1016/S1387-3806(00)00448-6.

[148] O. Hemberg, M. Otendal, H. M. Hertz, Liquid-metal-jet anode electron-impact x-ray source, Applied Physics Letters 83 (7) (2003) 1483–1485. doi:10.1063/1.1602157.

[149] T. Higashiguchi, M. Hamada, S. Kubodera, Development of a liquid tin microjet target for an efficient laser-produced plasma extreme ultraviolet source, Review of Scientific Instruments 78 (3) (2007) 036106. doi:10.1063/1.2712787.

[150] Y. Ueno, T. Ariga, G. Soumagne, T. Higashiguchi, S. Kubodera, I. Pogorelsky, I. Pavlishin, D. Stolyarov, M. Babzien, K. Kusche, V. Yakimenko, Efficient extreme ultraviolet plasma source generated by a CO_2 laser and a liquid xenon microjet target, Applied Physics Letters 90 (19) (2007) 191503. doi:10.1063/1.2738190.

[151] A. Lar'kin, D. Uryupina, K. Ivanov, A. Savel'ev, T. Bonnet, F. Gobet, F. Hannachi, M. Tarisien, M. Versteegen, K. Spohr, J. Breil, B. Chimier, F. Dorchies, C. Fourment, P.-M. Leguay, V. T. Tikhonchuk, Microjet formation and hard x-ray production from a liquid metal target irradiated by intense femtosecond laser pulses, Physics of Plasmas 21 (9) (2014) 093103. doi:10.1063/1.4894099.

[152] K. M. Lange, R. Könnecke, S. Ghadimi, R. Golnak, M. A. Soldatov, K. F. Hodeck, A. Soldatov, E. F. Aziz, High resolution X-ray emission spectroscopy of water and aqueous ions using the micro-jet technique, Chemical Physics 377 (1-3) (2010) 1–5. doi:10.1016/j.chemphys.2010.08.023.

[153] K. M. Lange, M. Soldatov, R. Golnak, M. Gotz, N. Engel, R. Könnecke, J.-E. Rubensson, E. F. Aziz, X-ray emission from pure and dilute H_2O and D_2O in a liquid microjet: Hydrogen bonds and nuclear dynamics, Physical Review B 85 (15) (2012) 155104. doi:10.1103/PhysRevB.85.155104.

[154] B. Dierker, E. Suljoti, K. Atak, K. M. Lange, N. Engel, R. Golnak, M. Dantz, K. Hodeck, M. Khan, N. Kosugi, E. F. Aziz, Probing orbital symmetry in solution: Polarization-dependent resonant inelastic soft x-ray scattering on liquid micro-jet, New Journal of Physics 15 (9) (2013) 093025. doi:10.1088/1367-2630/15/9/093025.

[155] O. J. Maselli, J. R. Gascooke, W. D. Lawrance, M. A. Buntine, The dynamics of evaporation from a liquid surface, Chemical Physics Letters 513 (1) (2011) 1–11. doi:10.1016/j.cplett.2011.06.010.

[156] A. M. Duffin, R. J. Saykally, Electrokinetic Power Generation from Liquid Water Microjets, The Journal of Physical Chemistry C 112 (43) (2008) 17018–17022. doi:10.1021/jp8015276.

[157] C. Li, P. Meng, H. Jiang, X. Hu, Power generation from microjet array of liquid water, Journal of Physics D: Applied Physics 51 (28) (2018) 285501. doi:10.1088/1361-6463/aacaa5.

[158] H.-j. Jang, E. Hur, Y. Kim, S.-H. Lee, N. G. Kang, J. J. Yoh, Laser-induced microjet injection into preablated skin for more effective transdermal drug delivery, Journal of Biomedical Optics 19 (11) (2014) 118002. doi:10.1117/1.JBO.19.11.118002.

[159] M. Faubel, Photoelectron spectroscopy at liquid surfaces, in: Photoionization and Photodetachment, World Scientific, 2000, pp. 634–690. doi:10.1142/9789812813473_0012.

[160] J. W. S. Rayleigh, J. W. S. B. Rayleigh, The Theory of Sound, Volume Two, Courier Corporation, 1945.

[161] J. Bockris, M. Devanathan, K. Müller, On the structure of charged interfaces, in: Electrochemistry, Elsevier, 1965, pp. 832–863.

[162] N. Kurahashi, S. Karashima, Y. Tang, T. Horio, B. Abulimiti, Y.-I. Suzuki, Y. Ogi, M. Oura, T. Suzuki, Photoelectron spectroscopy of aqueous solutions: Streaming potentials of NaX (X=Cl, Br, and I) solutions and electron binding energies of liquid water and X^-, The Journal of Chemical Physics 140 (17) (2014) 174506. doi:10.1063/1.4871877.

[163] SJ. Cavanagh, B. Lohmann, Coplanar asymmetric (e, 2e) measurements of ionization of N_2O, Journal of Physics B: Atomic, Molecular and Optical Physics 32 (12) (1999) L261. doi:10.1088/0953-4075/32/12/102.

[164] N. J. McCormick, Inverse Radiative Transfer Problems: A Review, Nuclear Science and Engineering 112 (3) (1992) 185–198. doi:10.13182/NSE112-185.

[165] K. M. Case, Inverse problem in transport theory, The Physics of Fluids 16 (10) (1973) 1607–1611. doi:10.1063/1.1694186.

[166] B. Davison, J. B. Sykes, Neutron Transport Theory, Clarendon Press, 1957.

[167] E. W. Larsen, J. B. Keller, Asymptotic solution of neutron transport problems for small mean free paths, Journal of Mathematical Physics 15 (1) (1974) 75–81. doi:10.1063/1.1666510.

[168] E. W. Larsen, Solution of three dimensional inverse transport problems, Transport Theory and Statistical Physics 17 (2-3) (1988) 147–167. doi:10.1080/00411458808230860.

[169] M. Vos, Extracting detailed information from reflection electron energy loss spectra, Journal of Electron Spectroscopy and Related Phenomena 191 (2013) 65–70. doi:10.1016/j.elspec.2013.10.007.

[170] M. Vos, A model dielectric function for low and very high momentum transfer, Nuclear Instruments and Methods in Physics Research Section B: Beam Interactions with Materials and Atoms 366 (2016) 6–12. doi:10.1016/j.nimb.2015.09.091.

[171] V. P. Afanas'ev, A. S. Gryazev, D. S. Efremenko, P. S. Kaplya, Differential inverse inelastic mean free path and differential surface excitation probability retrieval from electron energy loss spectra, Vacuum 136 (2017) 146–155. doi:10.1016/j.vacuum.2016.10.021.

[172] M. Michaud, L. Sanche, Absolute vibrational excitation cross sections for slow-electron (1–18 eV) scattering in solid H_2O, Physical Review A 36 (1987) 4684.

[173] M. Michaud, L. Sanche, Total cross sections for slow-electron (1–20 eV) scattering in solid H_2O, Physical Review A 36 (1987) 4672.

[174] M. Wojcik, M. Tachiya, Electron transport and electron–ion recombination in liquid argon: Simulation based on the Cohen–Lekner theory, Chemical Physics Letters 363 (3-4) (2002) 381–388. doi:10.1016/S0009-2614(02)01177-6.

[175] R. Winter, F. Hensel, T. Bodensteiner, W. Gläser, The static structure factor of cesium over the whole liquid range up to the critical point, Berichte der Bunsengesellschaft für physikalische Chemie 91 (12) (1987) 1327–1330. doi:10.1002/bbpc.19870911205.

[176] A. J. Greenfield, J. Wellendorf, N. Wiser, X-Ray Determination of the Static Structure Factor of Liquid Na and K, Physical Review A 4 (4) (1971) 1607–1616. doi:10.1103/PhysRevA.4.1607.

[177] J. L. Yarnell, M. J. Katz, R. G. Wenzel, S. H. Koenig, Structure Factor and Radial Distribution Function for Liquid Argon at 85 °K, Physical Review A 7 (6) (1973) 2130–2144. doi:10.1103/PhysRevA.7.2130.

[178] N. A. Garland, I. Simonović, G. J. Boyle, D. G. Cocks, S. Dujko, R. D. White, Electron swarm and streamer transport across the gas–liquid interface: A comparative fluid model study, Plasma Sources Science and Technology 27 (10) (2018) 105004. doi:10.1088/1361-6595/aae05c.

[179] Biagi database (Feb. 2023).

[180] D. Misra, Mish: A self regularized non-monotonic activation function, arXiv preprint arXiv:1908.08681 (2019). arXiv:1908.08681.

[181] M. Innes, Flux: Elegant machine learning with julia, Journal of Open Source Software 3 (2018) 602. doi:10.21105/joss.00602.

[182] X. Glorot, Y. Bengio, Understanding the difficulty of training deep feedforward neural networks, in: Y. W. Teh, M. Titterington (Eds.), Proceedings of the Thirteenth International Conference on Artificial Intelligence and Statistics, Vol. 9 of Proceedings of Machine Learning Research, PMLR, 2010-05-13/2010-05-15, pp. 249–256.

[183] J. Zhuang, t. tang, s. tatikonda, N. C. Dvornek, Y. Ding, X. Papademetris, J. s Duncan, AdaBelief optimizer: Adapting stepsizes by theBelief in observed gradients, in: NeurIPS 2020 Workshop: Deep Learning through Information Geometry, 2020.

[184] Y. Nesterov, A method of solving a convex programming problem with convergence rate $O(1/k^2)$, Soviet Mathematics Doklady 27 (1983) 372–376.

[185] T. Dozat, Incorporating Nesterov Momentum into Adam, in: Proceedings of 4th International Conference on Learning Representations, Workshop Track, 2016.

[186] J. D. Builth-Williams, Dynamical (e,2e) Studies of Bio-Molecules, https://theses.flinders.edu.au/view/6b9197c3-ad5f-44b2-8822-9abe9cc356fa/1 (2013).

[187] S. J. Cavanagh, B. Lohmann, Coplanar asymmetric (e, 2e) measurements of ionization of N_2O, Journal of Physics B: Atomic, Molecular and Optical Physics 32 (12) (1999) L261. doi:10.1088/0953-4075/32/12/102.

[188] D. A. Dahl, Simion for the personal computer in reflection, International Journal of Mass Spectrometry 200 (1) (2000) 3–25. doi:10.1016/S1387-3806(00)00305-5.

[189] N. Preissler, F. Buchner, T. Schultz, A. Lübcke, Electrokinetic charging and evidence for charge evaporation in liquid microjets of aqueous salt solution., The journal of physical chemistry. B 117 8 (2013) 2422–8. doi:10.1021/jp304773n.

[190] W. van Hoeve, S. Gekle, J. H. Snoeijer, M. Versluis, M. P. Brenner, D. Lohse, Breakup of diminutive Rayleigh jets, Physics of Fluids 22 (12) (2010) 122003. doi:10.1063/1.3524533.

[191] N. Garland, G. Boyle, D. Cocks, R. White, Approximating the nonlinear density dependence of electron transport coefficients and scattering rates across the gas?liquid interface, Plasma Sources Science and Technology 27 (2) (2018). doi:10.1088/1361-6595/aaaa0c.

[192] C. W. Duncan, I. C. Walker, Collision cross-sections for low energy electrons in methane, Journal of the Chemical Society, Faraday Transactions 2 68 (1972) 1514. doi:10.1039/f29726801514.

[193] T. F. O'Malley, R. W. Crompton, Electron-neon scattering length and S-wave phaseshifts from drift velocities, Journal of Physics B: Atomic and Molecular Physics 13 (17) (1980) 3451–3464. doi:10.1088/0022-3700/13/17/023.

[194] T. Taniguchi, M. Suzuki, K. Kawamura, F. Noto, H. Tagashira, A calculation method for estimating a cross section using a Boltzmann equation analysis, Journal of Physics D: Applied Physics 20 (8) (1987) 1085–1087. doi:10.1088/0022-3727/20/8/020.

[195] W. L. Morgan, The feasibility of using neural networks to obtain cross sections from electron swarm data, IEEE Transactions on Plasma Science 19 (2) (1991) 250–255. doi:10.1109/27.106821.

[196] W. L. Morgan, Test of a numerical optimization algorithm for obtaining cross sections for multiple collision processes from electron swarm data, Journal of Physics D: Applied Physics 26 (2) (1993) 209–214. doi:10.1088/0022-3727/26/2/007.

[197] M. J. Brennan, K. F. Ness, Momentum Transfer Cross Section for e+Kr Scattering, Australian Journal of Physics 46 (2) (1993) 249. doi:10.1071/ph930249.

[198] M. Flynn, J. Agan, A. Neuber, J. Stephens, Generation and optimization of cross-sections for electron-C_4F_7N collisions, Journal of Physics D: Applied Physics 56 (48) (2023) 485207. doi:10.1088/1361-6463/acf3db.

[199] M. Laroussi, Plasma Medicine: A Brief Introduction, Plasma 1 (1) (2018) 47–60. doi:10.3390/plasma1010005.

[200] H. Cho, Y. S. Park, E. A. y Castro, G. L. C. de Souza, I. Iga, L. E. Machado, L. M. Brescansin, M.-T. Lee, A comparative experimental–theoretical study on elastic electron scattering by methane, Journal of Physics B: Atomic, Molecular and Optical Physics 41 (4) (2008) 045203. doi:10.1088/0953-4075/41/4/045203.

[201] N. Işık, M. Doğan, S. Bahçeli, Triple differential cross section measurements for the outer valence molecular orbitals (1t2) of a methane molecule at 250 eV electron impact, Journal of Physics B: Atomic, Molecular and Optical Physics 49 (6) (2016) 065203. doi:10.1088/0953-4075/49/6/065203.

[202] A. Gadoum, D. Benyoucef, Set of the Electron Collision Cross Sections for Methane Molecule, IEEE Transactions on Plasma Science 47 (3) (2019) 1505–1513. doi:10.1109/TPS.2018.2885610.

[203] M. Harvey, A. Sakaamini, M. Patel, S. Amami, D. Madison, A. J. Murray, Triple differential cross-section measurements for electron-impact ionization of methane from a coplanar geometry to the perpendicular plane, The Journal of Chemical Physics 151 (19) (2019) 194305. doi:10.1063/1.5127121.

[204] D. Bouwman, A. Martinez, B. J. Braams, U. Ebert, Neutral dissociation of methane by electron impact and a complete and consistent cross section set, Plasma Sources Science and Technology 30 (7) (2021) 075012. doi:10.1088/1361-6595/ac0b2b.

[205] K. F. Ness, Multi-term solution of the Boltzmann equation for electron swarms in crossed electric and magnetic fields, Journal of Physics D: Applied Physics 27 (9) (1994) 1848. doi:10.1088/0022-3727/27/9/007.

[206] R. D. White, K. F. Ness, R. E. Robson, Velocity distribution functions for electron swarms in methane in electric and magnetic fields, Journal of Physics D: Applied Physics 32 (15) (1999) 1842. doi:10.1088/0022-3727/32/15/312.

[207] J. Stephens, L. Pitchford, M. Hopkins, B. Yee, Status Report on the LXCat Project, in: 2022 IEEE International Conference on Plasma Science (ICOPS), 2022, pp. 1–1. doi:10.1109/ICOPS45751.2022.9813059.

[208] S. Tian, X. Zhang, Y. Cressault, J. Hu, B. Wang, S. Xiao, Y. Li, N. Kabbaj, Research status of replacement gases for SF_6 in power industry, AIP Advances 10 (5) (2020) 050702. doi:10.1063/1.5134727.

[209] Y. Kieffel, F. Biquez, SF_6 alternative development for high voltage switchgears, in: International Conference on Advances in Communication and Computing Technologies, 2014. doi:10.1109/ICACACT.2014.7223577.

[210] A. V. Tatarinov, I. V. Bilera, S. V. Avtaeva, V. A. Shakhatov, P. V. Solomakhin, R. Maladen, C. Prévé, D. Piccoz, Dielectric Barrier Discharge Processing of trans-CF_3CH=CHF and CF_3C(O)CF(CF_3)2, Their Mixtures with Air, N_2, CO_2 and Analysis of Their Decomposition Products, Plasma Chemistry and Plasma Processing 35 (5) (2015) 845–862. doi:10.1007/s11090-015-9635-8.

[211] R. Akasaka, Vapor–liquid equilibrium modeling for mixtures of HFC-32 + isobutane and HFC-32 + HFO-1234ze(E), International Journal of Air-Conditioning and Refrigeration 19 (02) (2011) 93–97. doi:10.1142/s2010132511000478.

[212] S. Jribi, B. B. Saha, S. Koyama, A. Chakraborty, K. C. Ng, Study on activated carbon/HFO-1234ze(E) based adsorption cooling cycle, Applied Thermal Engineering 50 (2) (2011) 1570–1575. doi:10.1016/j.applthermaleng.2011.11.066.

[213] G. A. Longo, C. Zilio, G. Righetti, J. S. Brown, Experimental assessment of the low GWP refrigerant HFO-1234ze(Z) for high temperature heat pumps, Experimental Thermal and Fluid Science 57 (2014) 293–300. doi:10.1016/j.expthermflusci.2014.05.004.

[214] G. Righetti, C. Zilio, G. A. Longo, Comparative performance analysis of the low GWP refrigerants HFO1234yf, HFO1234ze(E) and HC600a inside a roll-bond evaporator, International Journal of Refrigeration 54 (2015) 1–9. doi:10.1016/j.ijrefrig.2015.02.010.

[215] A. Mota-Babiloni, J. Navarro-Esbrí, F. Molés, Á. B. Cervera, B. Peris, G. Verdú, A review of refrigerant R1234ze(E) recent investigations, Applied Thermal Engineering 95 (2015) 211–222. doi:10.1016/j.applthermaleng.2015.09.055.

[216] C. Aprea, A. Greco, A. Maiorino, C. Masselli, A. Metallo, HFO1234ze as Drop-in Replacement for R134a in Domestic Refrigerators: An Environmental Impact Analysis, Energy Procedia 101 (2016) 964–971. doi:10.1016/j.egypro.2016.11.122.

[217] C. Aprea, A. Greco, A. Maiorino, An experimental evaluation of the greenhouse effect in the substitution of R134a with pure and mixed HFO in a domestic refrigerator, International Journal of Heat and Technology 35 (Special Issue1) (2017) S413–S418. doi:10.18280/ijht.35sp0156.

[218] K. Śmierciew, J. Gagan, D. Butrymowicz, M. Lukaszuk, H. Kubiczek, Experimental investigation of the first prototype ejector refrigeration system with HFO-1234ze(E), Applied Thermal Engineering 110 (2017) 115–125. doi:10.1016/j.applthermaleng.2016.08.140.

[219] S. Daviran, A. Kasaeian, S. Golzari, O. Mahian, S. Nasirivatan, S. Wongwises, A comparative study on the performance of HFO-1234yf and HFC-134a as an alternative in automotive air conditioning systems, Applied Thermal Engineering 110 (2017) 1091–1100. doi:10.1016/j.applthermaleng.2016.09.034.

[220] C. Aprea, A. Greco, A. Maiorino, C. Masselli, The drop-in of HFC134a with HFO1234ze in a household refrigerator, International Journal of Thermal Sciences 127 (2018) 117–125. doi:10.1016/j.ijthermalsci.2018.01.026.

[221] X. Wang, Y. Yan, B. Li, X. Hao, N. Gao, G. Chen, Prospect of solar-driven ejector-compression hybrid refrigeration system with low GWP refrigerants in summer of Guangzhou and Beijing, International Journal of Refrigeration 117 (2020) 230–236. doi:10.1016/j.ijrefrig.2020.04.035.

[222] B. R. R. Bapu, S. Kayalvizhi, S. Murugavalli, Two phase cooling with nano-fluid for highly dense electronic systems-on-chip – A pilot study, Microelectronics Reliability 108 (2020) 113640. doi:10.1016/j.microrel.2020.113640.

[223] L. Ye, M. A. Islam, T. H. Rupam, I. Jahan, B. B. Saha, Study on the adsorption characteristics of Maxsorb III/HFO-1234ze(E) pair for adsorption refrigeration applications, International Journal of Refrigeration 146 (2023) 248–260. doi:10.1016/j.ijrefrig.2022.11.005.

[224] S. Koyama, N. Takata, S. Fukuda, Drop-in Experiments on Heat Pump Cycle Using HFO-1234ze(E) and Its Mixtures with HFC-32, International Refrigeration and Air Conditioning Conference at Purdue, July 12-15, 2010, 2010.

[225] S. Mishra, M. E. Khan, Theoretical Exergy Analysis of Actual Vapour Compression System with HFO-1234yf and HFO-1234ze as an Alternative Replacement of HFC-134a, Int. J. Sci. Res 5 (2016) 1684–1689.

[226] M. Abbrescia, P. V. Auwegem, L. Benussi, S. Bianco, S. Cauwenbergh, M. Ferrini, S. Muhammad, L. Passamonti, D. Pierluigi, D. Piccolo, F. Primavera, A. Russo, G. Saviano, M. Tytgat, Preliminary results of Resistive Plate Chambers operated with eco-friendly gas mixtures for application in the CMS experiment, Journal of Instrumentation 11 (09) (2016) C09018–C09018. doi:10.1088/1748-0221/11/09/c09018.

[227] A. Bianchi, S. Delsanto, P. Dupieux, A. Ferretti, M. Gagliardi, B. Joly, S. P. Manen, M. Marchisone, L. Micheletti, A. Rosano, E. Vercellin, Characterization of tetrafluoropropene-based gas mixtures for the Resistive Plate Chambers of the ALICE muon spectrometer, Journal of Instrumentation 14 (11) (2019) P11014–P11014. doi:10.1088/1748-0221/14/11/p11014.

[228] G. Proto, G. Aielli, E. A. Camelia, P. Camarri, R. Cardarelli, A. D. Ciaccio, L. D. Stante, B. Liberti, A. Paoloni, E. Pastori, L. Pizzimento, A. Rocchi, R. Santonico, E. Tusi, Characterization of new eco friendly gas mixtures based on HFO for RPCs, Journal of Instrumentation 16 (02) (2021) C02001–C02001. doi:10.1088/1748-0221/16/02/c02001.

[229] F. Molés, J. Navarro-Esbrí, B. Peris, A. Mota-Babiloni, Á. Barragán-Cervera, K. K. Kontomaris, Thermo-economic evaluation of low global warming potential alternatives to HFC-245fa in Organic Rankine Cycles, Energy Procedia 142 (2017) 1199–1205. doi:10.1016/j.egypro.2017.12.381.

[230] R. Gunawan, M. Z. Irriyanto, H. S. Cahyadi, M. Irshad, H.-S. Lim, B.-S. Choi, S.-K. Kwak, A. A. Myint, J.-H. Kim, Mechanism of thermal decomposition of HFO-1234ze(E) under supercritical fluid conditions, The Journal of Supercritical Fluids 160 (2020) 104792. doi:10.1016/j.supflu.2020.104792.

[231] L. Yang, S. R. P. da Rocha, Understanding Solvation in the Low Global Warming Hydrofluoroolefin HFO-1234ze Propellant, The Journal of Physical Chemistry B 118 (36) (2014) 10675–10687. doi:10.1021/jp5059319.

[232] C. M. Invernizzi, P. Iora, M. Preißinger, G. Manzolini, HFOs as substitute for R-134a as working fluids in ORC power plants: A thermodynamic assessment and thermal

stability analysis, Applied Thermal Engineering 103 (2016) 790–797. doi:10.1016/j.applthermaleng.2016.04.101.

[233] V. Rapinel, C. Breil, C. Makerri, M. Jacotet-Navarro, N. Rakotomanomana, A. Vallageas, F. Chemat, Feasibility of using liquefied gas HFO-1234ze (trans-1,3,3,3-tetrafluoroprop-1-ene) as an alternative to conventional solvents for solid–liquid extraction of food ingredients and natural products, LWT - Food Science and Technology 83 (2017) 225–234. doi:10.1016/j.lwt.2017.05.027.

[234] R. W. Macpherson, M. P. Wilson, S. J. MacGregor, I. V. Timoshkin, M. J. Given, T. Wang, Characterization and Statistical Analysis of Breakdown Data for a Corona-Stabilized Switch in Environmentally Friendly Gas Mixtures, IEEE Transactions on Plasma Science 46 (10) (2018) 3557–3565. doi:10.1109/tps.2018.2844954.

[235] P. Ranjan, L. Chen, A. Alabani, F. O. Bahdad, I. Cotton, L. van der Zel, Anomalous First Breakdown Behavior for HFO1234ze(E), IEEE Transactions on Dielectrics and Electrical Insulation 28 (5) (2021) 1620–1627. doi:10.1109/tdei.2021.009676.

[236] D. Basu, J. Pachin, E. Eguz, C. Franck, Improved Estimation of Uniform AC Electric Breakdown Field Strength of HFO1234ze(E), IEEE Transactions on Dielectrics and Electrical Insulation 30 (1) (2023) 263–270. doi:10.1109/tdei.2022.3214179.

[237] K. R. Solomon, G. J. M. Velders, S. R. Wilson, S. Madronich, J. Longstreth, P. J. Aucamp, J. F. Bornman, Sources, fates, toxicity, and risks of trifluoroacetic acid and its salts: Relevance to substances regulated under the Montreal and Kyoto Protocols, Journal of Toxicology and Environmental Health, Part B 19 (7) (2016) 289–304. doi:10.1080/10937404.2016.1175981.

[238] A. G. Berends, J. C. Boutonnet, C. G. D. Rooij, R. S. Thompson, Toxicity of trifluoroacetate to aquatic organisms, Environmental Toxicology and Chemistry 18 (5) (1999) 1053–1059. doi:10.1002/etc.5620180533.

[239] A. Lindley, A. McCulloch, T. Vink, Contribution of Hydrofluorocarbons (HFCs) and Hydrofluoro-Olefins (HFOs) Atmospheric Breakdown Products to Acidification (“Acid Rain”) in the EU at Present and in the Future, Open Journal of Air Pollution 08 (04) (2019) 81–95. doi:10.4236/ojap.2019.84004.

[240] D. J. Luecken, R. L. Waterland, S. Papasavva, K. N. Taddonio, W. T. Hutzell, J. P. Rugh, S. O. Andersen, Ozone and TFA Impacts in North America from Degradation of 2,3,3,3-Tetrafluoropropene (HFO-1234yf), A Potential Greenhouse Gas Replacement, Environmental Science & Technology 44 (1) (2009) 343–348. doi:10.1021/es902481f.

[241] H. Flerlage, G. J. M. Velders, J. de Boer, A review of bottom-up and top-down emission estimates of hydrofluorocarbons (HFCs) in different parts of the world, Chemosphere 283 (2021) 131208. doi:10.1016/j.chemosphere.2021.131208.

[242] A. Chachereau, C. Franck, Characterization of HFO1234ze mixtures with N_2 and CO_2 for use as gaseous electrical insulation media, in: 20th International Symposium on High Voltage Engineering (ISH 2017), Asociación Cooperadora de la Facultad de Ciencias Exactas y Tecnología de la . . . , 2017, p. 257.

[243] Z. L. Petrović, J. Atić, D. Marić, S. Dujko, G. Malović, J. de Urquijo, M. Ise, T. Hammer, Cross Sections for Scattering of Electrons on Tetrafluoropropene HFO1234ze Obtained from The Swarm Data (2019).

[244] A. Bianchi, A. Ferretti, M. Gagliardi, E. Vercellin, Electron collision cross sections in tetrafluoropropene HFO1234ze (2021). doi:10.48550/arXiv.2103.08643.

[245] EA. Egüz, J. Pachin, CM. Franck, Discussion on the mechanism leading to positive synergism in SF6 mixtures with HFO1234ze(E), Journal of Physics D: Applied Physics 55 (31) (2022) 315203. doi:10.1088/1361-6463/ac6cb5.

[246] M. Antiñolo, I. Bravo, E. Jiménez, B. Ballesteros, J. Albaladejo, Atmospheric Chemistry of E- and Z-CF_3CH=CHF (HFO-1234ze): OH Reaction Kinetics as a Function of Temperature and UV and IR Absorption Cross Sections, The Journal of Physical Chemistry A 121 (43) (2017) 8322–8331. doi:10.1021/acs.jpca.7b06174.

[247] Z. Petrovic, Electron Scattering Cross Sections and Calculated Transport Data for a New Class of Cooling Gases, in: APS Annual Gaseous Electronics Meeting Abstracts, APS Meeting Abstracts, 2021, p. DT23.003.

[248] J. de Urquijo.

[249] J. Schwabedissen, T. Glodde, Y. V. Vishnevskiy, H.-G. Stammler, L. Flierl, A. J. Kornath, N. W. Mitzel, Structures and Properties of \emphtrans-1,3,3,3-Tetrafluoro- propene (HFO-1234ze) and 2,3,3,3-Tetrafluoropropene (HFO-1234yf) Refrigerants, ChemistryOpen 9 (9) (2020) 921–928. doi:10.1002/open.202000172.

[250] L. Benussi, S. Bianco, M. Ferrini, L. Passamonti, D. Pierluigi, D. Piccolo, A. Russo, G. Saviano, A study of HFO-1234ze (1,3,3,3-Tetrafluoropropene) as an eco-friendly replacement in RPC detectors (May 2015). doi:10.48550/ARXIV.1505.01648.

[251] Y. Liang, F. Wang, Q. Sun, Y. Zhai, Molecular structural and electrical properties of trans-1,3,3,3-tetrafluoropropene and 2,3,3,3-tetrafluoropropene under external electric

fields, Computational and Theoretical Chemistry 1120 (2017) 79–83. doi:10.1016/j.comptc.2017.09.017.

[252] A. W. Ray, P. Weidner, A. Bodi, B. Sztáray, The Vagabond Fluorine Atom: Dissociative Photoionization of trans-1,3,3,3-Tetrafluoropropene, The Journal of Physical Chemistry A 124 (19) (2020) 3738–3746. doi:10.1021/acs.jpca.0c01804.

[253] H. Gan, F. Wang, L. Zhong, J. Liu, B. Hai, N. Tang, L. Li, Theoretical study of the discharge decomposition mechanism of environment-friendly insulation gas HFO-1234ze(E) in the presence of trace water, Journal of Physics: Conference Series 2221 (1) (2022) 012024. doi:10.1088/1742-6596/2221/1/012024.

[254] ETHZ database (Feb. 2024).

[255] E. A. Egüz, J. Pachin, H. Vemulapalli, C. M. Franck, Synergism in SF_6 mixtures with C=C-C backbone compounds, J. Phys. D Appl. Phys. (May 2023).

[256] N. Garland, D. Muccignat, G. Boyle, R. White, Robust approximation rules for critical electric field of dielectric gas mixtures (Dec. 2023). arXiv:2312.04755, doi:10.48550/arXiv.2312.04755.

[257] P. Nag, M. L. Ranković, H. C. Schewe, J. Rakovský, L. Sala, J. Kočišek, J. Fedor, Experimental setup for probing electron-induced chemistry in liquid micro-jets, Journal of Physics B: Atomic, Molecular and Optical Physics (Oct. 2023). doi:10.1088/1361-6455/ad0205.

[258] K. F. Ness, R. E. Robson, Velocity distribution function and transport coefficients of electron swarms in gases. II. Moment equations and applications, Physical Review A 34 (3) (1986) 2185. doi:10.1103/PhysRevA.34.2185.

[259] G. Boyle, The modelling of non-equilibrium light lepton transport in gases and liquids, Ph.D. thesis, James Cook University (2015).

[260] N. J. McCormick, I. Kuščer, On the inverse problem in radiative transfer, Journal of Mathematical Physics 15 (7) (1974) 926–927. doi:10.1063/1.1666771.

Appendix A

Appendix

A.1 Benchmarking of the liquid micro-jet simulation

Throughout the development of the present MC simulation, systematic benchmarking was conducted through comparisons of transport coefficients for swarm experiments under highly non-equilibrium conditions (Appendix A.1.1). Further, we have developed a relatively simple analytic model for the EELS and have systematically benchmarked the simulation against this (Appendix A.1.2).

A.1.1 Swarm benchmarks

In this section, we first present Lucas and Saelee's electron impact ionisation model to evaluate the accuracy of elastic, inelastic and ionisation collisions [258]. We then present a modified Percus-Yevic benchmark [259], to benchmark the liquid scattering dynamics discussed in Section 2.3.1. Lucas and Saelee's electron impact ionisation model is defined as the following:

$$
\begin{aligned}
\sigma_{elastic} &= 4U^{-\frac{1}{2}}\ \text{Å}^2, \\
\sigma_{inelastic} &= \begin{cases} 0.1(1-F)(U-15.6)\ \text{Å}^2, & U \geq 15.6\ \text{eV} \\ 0, & U < 15.6\ \text{eV} \end{cases} \\
\sigma_{ionisation} &= \begin{cases} 0.1F(U-15.6)\ \text{Å}^2, & U \geq 15.6\ \text{eV} \\ 0, & U < 15.6\ \text{eV} \end{cases} \\
E/n_0 &= 10\ \text{Td}, \\
m/m_0 &= 10^{-3}, \\
T_0 &= 0\ \text{K},
\end{aligned}
\tag{A.1}
$$

Table A.1: Swarm benchmark results for Lucas and Saelee's electron impact ionisation using the current MC code, presented alongside an independent solution to the Boltzmann equation [259]. Provided, for comparison, are the mean energy (ε), drift velocity (W) and the transverse (D_T) and longitudinal (D_L) diffusion coefficients for each value of F. Note that error estimates are given by the standard deviation of each transport coefficient with respect to time. For this benchmark 10^6 particles were simulated for $n_0 t = 2 \times 10^{16}$ sm^{-3}, where averages were conducted over the latter half of the simulation time.

F		ε [eV]	W [10^4 ms^{-1}]	$n_0 D_T$ [10^{24} m^{-1}s^{-1}]	$n_0 D_L$ [10^{24} m^{-1}s^{-1}]
0	[259]	5.565	7.319	27.26	26.54
	Current	5.563	7.327	27.28	26.64
	Uncertainty	0.0001	0.003	0.03	0.04
0.5	[259]	5.224	8.593	27.26	28.65
	Current	5.223	8.594	27.23	28.62
	Uncertainty	0.001	0.005	0.04	0.07
1	[259]	4.969	9.474	27.23	29.33
	Current	4.968	9.487	27.25	29.42
	Uncertainty	0.002	0.008	0.05	0.01

where U is energy in eV, E is the electric field, m is the electron mass, n_0 and m_0 are the background density and mass, respectively, while F is a parameter introduced to control the ratio of ionisation to inelastic collisions and reduced electric field, E/n_0, is given in Townsend units of Td $= 10^{-21}$ Vm^2. This model's strength comes from the fact that the total cross-section is independent of F. Therefore, variation of the ratio between ionisation and inelastic collisions allows for the isolation of the effects produced by each collision type. The results of this application are shown in Table A.1 for F values of 0, 0.5 and 1, with excellent agreement being found between the Boltzmann equation and present MC results for each transport coefficient.

We also present results from an adaptation of the Percus-Yevick model liquid benchmark, where the elastic cross-section is held constant and an additional, low energy inelastic cross-section is included:

$$\begin{aligned} \sigma_{elastic} &= 6 \text{ Å}^2, \\ \sigma_{inelastic} &= \begin{cases} 0, & U < 2 \text{ eV} \\ 0.1 \text{ Å}^2, & U \geq 2 \text{ eV} \end{cases} \\ \phi &= 0, 0.2, 0.3, 0.4 \\ m_0 &= 4 \text{ amu}, \\ E/n_0 &= 3 \text{ Td}, \\ T &= 0 \text{ K}, \end{aligned} \tag{A.2}$$

where ϕ is the so-called packing factor. For this model, a representative structure factor, detailed in [259], was implemented to verify coherent scattering. The time-averaged values are presented

Table A.2: Swarm benchmark results for our modified Percus-Yevik benchmark (equation (A.2)), from the current MC code, presented alongside an independent solution to the Boltzmann equation [259]. Provided, for comparison, are the mean energies (ε), drift velocities (W), and the transverse (D_T) and longitudinal (D_L) diffusion coefficients for each value of ϕ. Note that error estimates are given by the standard deviation of each transport coefficient with respect to time. For this benchmark 10^5 particles were simulated for varying times, where averages were conducted over the latter half of the simulation time.

ϕ		ε [eV]	W [10^4 ms^{-1}]	$n_0 D_T$ [10^{24} m^{-1}s^{-1}]	$n_0 D_L$ [10^{24} m^{-1}s^{-1}]
0.	[259]	0.833	1.385		2.38
	Current	0.834	1.384	2.825	2.38
	Uncertainty	0.0001	0.001	0.017	0.02
0.2	[259]	0.976	3.397		6.32
	Current	0.977	3.388	9.09	6.35
	Uncertainty	0.0001	0.003	0.04	0.05
0.3	[259]	1.080	5.929		11.2
	Current	1.080	5.915	17.92	11.1
	Uncertainty	0.0001	0.001	0.009	0.01
0.4	[259]	1.233	10.52		19.51
	Current	1.234	10.50	34.97	19.51
	Uncertainty	0.0001	0.004	0.013	0.013

in Table A.2, for various values of the packing factor ϕ, which is proportional to the density of the liquid used. Again, excellent agreement between the Boltzmann equation and present MC results, for each transport coefficient, is observed.

A.1.2 Beam benchmark

In this section, we derive a simplified analytic expression for results from reflected EELS measurements from an infinite half-plane given the underlying scattering cross-sections. We first note that, due to threshold excitation collisions, distinct peaks are expected to be observed in the EELS. The relationship between each scattering process (i.e. elastic, excitation and ionisation collisions) and their associated cross-sections, and the area of the corresponding EELS peak can be represented through an infinite series. Given the probability, p_n, of an electron escaping the jet after n collisions, the integral of an observed elastic scattering peak over the EELS, $I(\varepsilon)$, is given by the infinite series:

$$p_1 \frac{\sigma_{el}(\varepsilon_c)}{\sigma_t(\varepsilon_c)} + p_2 \left(\frac{\sigma_{el}(\varepsilon_c)}{\sigma_t(\varepsilon_c)}\right)^2 + p_3 \left(\frac{\sigma_{el}(\varepsilon_c)}{\sigma_t(\varepsilon_c)}\right)^3 + \ldots = \frac{1}{N}\int_{el} I(\varepsilon)\, d\varepsilon, \tag{A.3}$$

where the integration bound *el* is the peak width associated with pure elastic collision paths, ε is electron energy, σ_{el} and σ_t are the elastic and total cross-sections, respectively, and N is the initial number of electrons. For notation purposes, the left-hand side of equation (A.3) has been simplified as each subsequent collision will result in small energy losses that are encompassed by ε_c. Assuming a single collision, equation (A.3) reduces to:

$$p_1 \frac{\sigma_{el}(\varepsilon_0)}{\sigma_t(\varepsilon_0)} = \frac{1}{I_0} \int_{el} I(\varepsilon)\, d\varepsilon, \tag{A.4}$$

where ε_0 is the initial energy. If we denote the unknown background medium with the subscript *un*, and introduce a reference medium ref, we can then use the ratio of their peaks to arrive at the following relationship:

$$\frac{\sigma^{un}_{elastic}(\varepsilon_0)}{\sigma^{un}_{total}(\varepsilon_0)} = \frac{p_1^{ref}}{p_1^{un}} \frac{I_0^{ref} \int_{el} I^{un}(\varepsilon)\, d\varepsilon}{I_0^{un} \int_{el} I^{ref}(\varepsilon)\, d\varepsilon} \frac{\sigma^{ref}_{total}(\varepsilon_0)}{\sigma^{ref}_{elastic}(\varepsilon_0)}. \tag{A.5}$$

Given the above relationship and assuming that $p_1^{un} = p_1^{ref} = 1$, due to a restriction to single scattering events, such as with beam experiments in the gas-phase, we can then derive unknown cross-section sets given the reference cross-section sets and the experimental limitations being considered. Attempts to extend this to include multiple collisions results in an ill posed set of equations [260]. However, under certain assumptions, limited analytical expressions can be derived, which are subsequently used for benchmarking the developed MC simulation package.

Equation (A.3) can be used to derive an expression for each peak within the EELS, assuming we know the cross-section set and each probability p_n. Using a known cross-section, we thus seek an analytical or numerical solution for p_n. First, we consider the case for p_1. To escape, each electron must travel a distance s_1 without colliding, and then undergo a collision before travelling a distance s' towards the surface without undergoing another collision. If we assume a constant cross-section, the probability that a collision will occur at some distance s is given by the following:

$$p(s)\, ds = \frac{1}{l} \exp\left(-\frac{s}{l}\right) ds, \tag{A.6}$$

where l is the mean free path. Assuming now isotropic scattering, the probability of scattering with azimuthal angle χ and polar angle ψ, with respect to the initial velocity, is given by:

$$p(\chi) \sin\chi d\chi = \frac{1}{2} \sin\chi d\chi, \tag{A.7}$$

where the ψ dependence has been integrated over and normalised. Each detected electron then escapes the jet by travelling a distance s', defined through:

$$s' = -\frac{s}{\cos\chi}. \tag{A.8}$$

The probability to not collide in some distance s', is given by the cumulative distribution function (CDF):

$$P(s > s') = 1 - \int_0^{s'} \frac{1}{l} \exp\left(-\frac{s''}{l}\right) ds'', \tag{A.9}$$

$$P(s > s') = \exp\left(\frac{s}{l\cos\chi}\right). \tag{A.10}$$

To couple the spatial and angular probability densities, we multiply equations (A.6), (A.7) and (A.10) together to obtain the probability that an electron will escape after a collision at distance s and angle χ:

$$P(\chi, s)\sin\chi d\chi ds = \frac{1}{2l}\exp\left(-\frac{s}{l}\right)\exp\left(\frac{s}{l\cos\chi}\right)\sin\chi d\chi ds. \tag{A.11}$$

After performing a variable change to energy loss u_f, and utilising the following:

$$\frac{du_f}{d\chi} = \frac{2mm_0}{(m+m_0)^2}\sin\chi, \tag{A.12}$$

where m and m_0 are the electron mass and target mass, respectively, then integrating equation (A.11) with respect to (u_f, s) we arrive at the expression for p_1:

$$p_1 = \int \frac{1}{2}\left[\frac{(m+m_0)^2}{2mm_0} - \frac{1}{u_f}\right] du_f. \tag{A.13}$$

We then extend the method to calculate p_2, which requires the use of numerical integration techniques. Each electron now initially travels a distance s_1 and s_2, before each collision. The detected electron must then travel a distance s', towards the surface to escape. Note that the scattering angles χ and ψ, are now relative to the direction of motion prior to each respective collision. The probability that an electron will undergo each collision at s_1 and s_2, with scattering angles of (χ_1, ψ_1) and (χ_2, ψ_2), before escaping after some distance s', is given by:

$$P(s_1, s_2, s', \chi_1, \chi_2, \psi_1, \psi_2) = \frac{1}{16\pi^2 l^2}\exp\left(-\frac{s_1}{l}\right)\exp\left(-\frac{s_2}{l}\right)\exp\left(-\frac{s'}{l}\right), \tag{A.14}$$

where s' is represented through a similar CDF as equation (A.10). Assuming an initial position of $\vec{r} = [0,0,0]$, velocity $\vec{v} = [0,0,v_z]$, and a jet surface along $r_z = 0$, each detected electron must return to the surface defined by $r_z = 0$. To achieve an expression for this, we rotate the reference frame of the second collision by χ_1, about an appropriate unit vector, to the initial frame of reference according to Rodrigues' rotation formula. The z co-ordinate after two collisions is then given by:

$$r_z = s_1 + s_2\cos\chi_1 + s'\left(\cos\chi_1\cos\chi_2 - \sin\chi_1\sin\chi_2\cos(\psi_1 - \psi_2)\right).$$

Setting $r_z = 0$, we arrive at an expression for s':

$$s' = -\frac{s_1 + s_2\cos\chi_1}{\cos\chi_1\cos\chi_2 - \sin\chi_1\sin\chi_2\cos(\psi_1 - \psi_2)}.$$

Substituting this into equation (A.14) we find:

$$P(s_1,s_2,\chi_1,\chi_2,\psi_1,\psi_2) = \frac{1}{16\pi^2 l^2}\exp\left(-\frac{s_1}{l}\right)\exp\left(-\frac{s_2}{l}\right) \times \exp\left(\frac{1}{l}\frac{s_1+s_2\cos\chi_1}{\cos\chi_1\cos\chi_2-\sin\chi_1\sin\chi_2\cos(\psi_1-\psi_2)}\right). \tag{A.15}$$

The integration of equation (A.15) over the appropriate limits, along with a transformation of variables to energy loss, gives p_2. Any non-physical limits were removed using step functions, and they are detailed in what follows. First, bounds for which $s' < 0$ were removed as if $s' < 0$ the electron has already escaped after a single collision and is accounted for in p_1. Additionally, any divisions by 0 were also removed. Extending this methodology to higher terms is theoretically possible. However, in this investigation we include only p_1 and p_2 due to limitations in the available computation power.

For illustrative purposes and a comparison, a MC simulation of a 15 µm LµJ was then considered with the following model:

$$\begin{aligned} \sigma_{elastic} &= 1\,\text{Å}^2, \\ \sigma_{inelastic,1} &= \begin{cases} 0, & \varepsilon < 0.3\,\text{eV} \\ 1\,\text{Å}^2, & \varepsilon > 0.3\,\text{eV} \end{cases}, \\ \sigma_{inelastic,2} &= \begin{cases} 0, & \varepsilon < 0.5\,\text{eV} \\ 1\,\text{Å}^2, & \varepsilon > 0.5\,\text{eV} \end{cases}, \\ n_0 &= 2.13\times 10^{28}\,\text{m}^{-3}. \end{aligned} \tag{A.16}$$

Additionally, a numerical integration (using a Monte Carlo technique) was conducted for up to two collisions, and compared with the simulated results in Figure A.1. MC simulations that measure both all and up to 2 collisions are included as separate series. Also included as shaded regions are error estimations based upon standard deviations between successive simulations. Excellent agreement was found for up to two collisions. While being somewhat limited in scope, this benchmarking further lends confidence to the accuracy of the simulation.

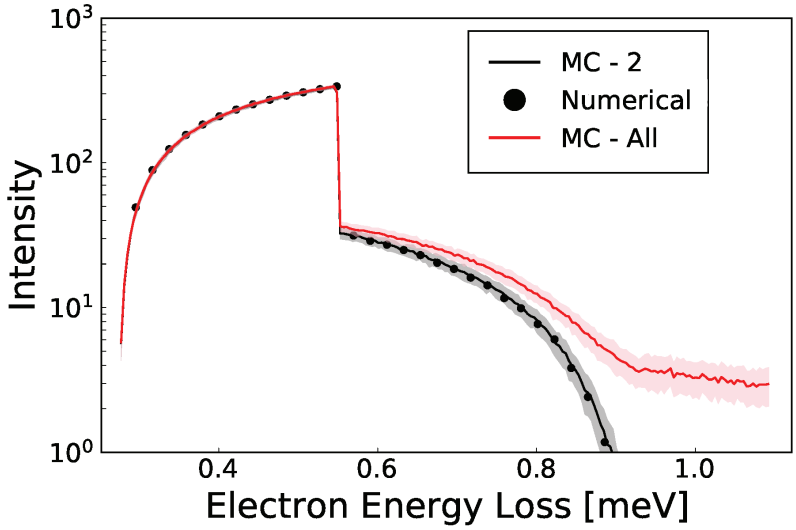

Figure A.1: Comparison of the elastic peak in the EELS using a MC simulation including all collisions (red line), a MC simulation with 2 collisions (black line) and a Monte Carlo integration of 2 collisions (black dots). Shaded areas indicate the standard deviation of successive simulations. Resulting from single collisions, a large clear initial hump is present and consistent between all three models. A sharp drop-off followed by a decaying tail, then represents electrons that underwent multiple collisions. Excellent agreement was found between both the numerical and Monte Carlo method.

A.2 Deep learning technique

A.2.1 LXCat data augmentation

To provide the network with sufficient training samples, we implement the data augmentation method first presented by Stokes *et. al.* [1]. First, we collate an appropriate set of physically plausible example swarm transport data using cross-sections from the LXCat project [52, 72, 73]. Following the method outlined in the work of Jetly *et al.* [105,], from a total of 397 elastic and effective cross-sections available, 3 groups of similar features were created by visual inspection. The total number of cross-sections contained in each group were 60, 130, and 197. In addition, 6763, 451 and 332 cross-sections in total were present for excitation, ionisation and attachment processes respectively.

In each iteration, we then generate a database of example cross-sections through a randomised mixing of cross-section pairs using a weighted sum in log space, [1]:

$$\sigma_s(\varepsilon) = \sigma_1^{1-r'}\left(\varepsilon - \varepsilon_1 + \varepsilon_1^{1-r'}\varepsilon_2^{r'}\right)\sigma_2^{r'}\left(\varepsilon - \varepsilon_2 + \varepsilon_1^{1-r'}\varepsilon_2^{r'}\right), \tag{A.17}$$

where σ_1 and σ_2 are a random pair of LXCat electron scattering cross-sections, sampled from the available targets, for a given process type (e.g., excitation, ionisation, etc.), while ε_1 and ε_2 are their respective threshold energies. The parameter r' is a pseudo-random mixing ratio. To help ensure a physical representation of cross-sections within the training set, a scaled Laplace

distribution truncated to the domain $r \in [0, 1.5]$ was chosen to bias r' towards small perturbations around each example cross-section. Any decaying distribution may be sufficient for this purpose however. Ratios greater than 1 are used here to accentuate cross-section features found within the sample set to reduce the extend of outliers within the set. Note that for the elastic cross-section, we sample two cross-sections from the three groups so that each group is equally represented in the training set.

In addition, due to the limited nature of the available data, the solution may exist at the extremes of the available training data which can introduce unwanted bias in the data augmentation process. To alleviate this, Equation A.17 is modified such that the energy domain and magnitude of each cross-section are multiplied by the scaling factors 10^a and 10^b respectively. Each factor is a pseudo-random number uniformly distributed within a defined range. Here, we set $a \in [-0.5, 0.5], b \in [-0.5, 0.5]$ for elastic cross-sections, $a = 0, b \in [0, 2]$ for excitation cross-sections, $a = 0, b \in [0, 1]$ for ionisation cross-sections and $a \in [-1, 1], b \in [-1, 1]$ for attachment cross-sections. Each was chosen to reasonably extend the extent of the available training data. Finally, we log transform then scale each cross-section between -1 and 1. If a cross-section magnitude is below $\delta = 10^{-6}$, it is replaced by 10^{-7} before applying the transform.

For each generated cross-section set, the resulting transport coefficients are calculated through a multi-term Boltzmann equation solver according to the target experimental transport coefficients. If a particular set results in non-physical transport coefficients, the set is removed from the training set and a new set is found until the condition is satisfied. For this investigation, physical transport coefficients are defined as $\mathbf{W} > 0$ and $n_0 \mathbf{D}_\mathrm{L} > 0$, where the electric field is directed along the negative z-axis. In addition, we apply a logarithmic transformation to ensure that all inputs and outputs of the network are dimensionless and lie within $[-1, 1]$, with special consideration given to $\mathbf{k}_\mathrm{eff}$ due to the presence of negative values. The vectors $\mathbf{k}^+_\mathrm{eff}$ and $\mathbf{k}^-_\mathrm{eff}$ are created to represent the positive and negative portions of the original input respectively. For $\mathbf{k}^+_\mathrm{eff}$, each negative value is set to a sufficiently small positive value while for $\mathbf{k}^-_\mathrm{eff}$, each positive value is set to a sufficiently small negative value before taking the absolute value of each.

A.2.2 Training procedure

Training of the network is conducted using a mini-batch of 32 cross-section sets evaluated at 128 energies for a particular iteration. Each *weight* and *bias* is then updated using the 'NAdam' optimiser [185] with a learning rate of 0.001 and 0.9 and 0.999 as the exponential decay for the first and the second momentum estimate respectively. For each batch, random noise is applied to each transport coefficient. Noise is sampled from a lognormal distribution with a standard deviation chosen to replicate experimental uncertainties typically observed for each transport coefficient.

The prediction of multiple cross-sections of the same collision type has previously been

shown to be a highly degenerate problem, particularly in the case of excitation collisions [1]. To emphasise the importance of the total cross-section, we use a loss function that includes a penalty for the total cross-section for each process type, in addition to each individual cross-section. The loss function is defined as follows,

$$L = \frac{1}{I}\sum_{i}^{I}\frac{1}{M_i+1}\left[\sum_{\sigma\in\boldsymbol{\sigma}_i}|\sigma-\hat{\sigma}| + \left|\sum_{\sigma\in\boldsymbol{\sigma}_i}\sigma - \sum_{\sigma\in\boldsymbol{\sigma}_i}\hat{\sigma}\right|\right], \tag{A.18}$$

where $\boldsymbol{\sigma}_i$ is the set of M_i cross-sections for the collision type i, I is the number of collision types present and $\hat{\sigma}$ is the predicted cross-section. Note that the calculation of the total cross-sections is conducted in linear space before scaling is re-applied.

To validate the network, we set aside 5 % of the available cross-sections for each collision type to form the basis of our validation set. In the case of the elastic cross-sections, 5 % of each of the feature groups is selected. The chosen validation cross-sections then undergo the same data augmentation as the training data to produce 100 samples. Every 100 iterations we test the network on the validation set and calculate the MARPD over the energy domain,

$$\text{MARPD} = \frac{1}{I}\sum_{i}^{I}\left|100\times\frac{\sigma_{t,i}-\hat{\sigma}_{t,i}}{|\sigma_{t,i}|+|\hat{\sigma}_{t,i}|}\right|, \tag{A.19}$$

where $\sigma_{t,i}$ is the total cross-section for the collision type i. During training, the validation loss is used to both compare network parameters and aid in preventing overfitting.

In addition, every 10 training iterations we store the neural network's prediction of the target transport data and compare the resulting transport coefficients. Due to the presence of multiple distinct fit parameters, we repeatedly select one random parameter and then remove the worst predicted cross-section set until only one remains. This process is then replicated 1000 times before the cross-section set which appears most frequently is chosen as the best overall fit. As desired, the best overall fit can be removed, and the processes repeated to find the next best fit.

To select each hyperparameter, a simple tuning process was conducted that compared the validation loss between reasonable values for batch size (32, 64, 128), number of hidden layers (2, 3, 4, 5), hidden layer size (32, 64, 128, 256) and the optimiser used (NAdam, Adam). For simplicity, this processes was conduced with a conventional ANN in which each layer contained an equal number of neurons and the output consisted of an elastic and ionisation cross-section along with three electronic excitation cross-sections. The tuning processes indicated that 4-5 hidden layers with 128-256 neurons resulted in the smallest validation error. Due to computational limitations, a more extensive tuning that includes branching hidden layers and a greater variation of parameters was not conducted.

And so, does the destination matter? Or is it the path we take? I declare that no accomplishment has substance nearly as great as the road used to achieve it. We are not creatures of destinations. It is the journey that shapes us. Our callused feet, our backs strong from carrying the weight of our travels, our eyes open with the fresh delight of experiences lived.

Brandon Sanderson,
The Way of Kings